UPPSALA
UNIVERSITET

Theoretical Investigations of Two-Dimensional Materials

Studies on Electronic, Magnetic, Mechanical, and Thermal Properties

XIN CHEN

Dissertation presented at Uppsala University to be publicly examined in Häggsalen/10132, Ångströmlaboratoriet, Lägerhyddsvägen 1, Uppsala, Friday, 27 November 2020 at 09:15 for the degree of Doctor of Philosophy. The examination will be conducted in English. Faculty examiner: Professor Kristian Sommer Thygsen (Technical University of Denmark).

Abstract

Chen, X. 2020. Theoretical Investigations of Two-Dimensional Materials. Studies on Electronic, Magnetic, Mechanical, and Thermal Properties. *Digital Comprehensive Summaries of Uppsala Dissertations from the Faculty of Science and Technology* 1975. 100 pp. Uppsala: Acta Universitatis Upsaliensis. ISBN 978-91-513-1027-5.

Two-dimensional (2D) materials have been paid enormous attention since the first realization of graphene in 2004, in connection to high-speed flexible electronics, 2D magnetism, optoelectronics, and so on. Apart from graphene, many new 2D materials with special properties have been predicted and synthesized. For the understanding of several interesting phenomena and prediction of new 2D materials, materials-specific density functional theory (DFT) plays a very important role.

In this thesis, based on first-principles calculations, structural, magnetic, electronic, mechanical, and thermal transport properties of two kinds of 2D systems are investigated.

The first kind of 2D materials is based on the synthesized material or the predicted structure with ultralow energy. These materials were functionalized by adsorbing transition metal atoms or oxygen atoms, which makes a significant difference in the properties. A part of the thesis covers the study of the self-assembly process of 3d transition metal hexamers on graphene with different defects. Interestingly, it is found that the easy axis of magnetization can be tuned between in-plane and out-of-plane directions in the presence of an external electric field. The second subsection is the oxygen functionalized form of 2D honeycomb and zigzag dumbbell silicene. Interestingly, both the structures are Dirac semimetal.

The other kind of 2D materials discussed in this thesis are new materials which were never reported before. Starting from a global structure search, we predicted several structures with ultrahigh stability and novel properties. One work is about a new allotrope of graphene, namely PAI-graphene. It is a new structural motif, which is energetically very close to graphene with interesting properties. PAI-graphene is a semimetal with distorted Dirac cones. By applying tensile strain, three different topological phases can be achieved. The second subsection is the work about new 2D structural forms of A_2B (A=Cu, Ag, Au, and B=S, Se). Our obtained square-A_2B (s-A_2B) structures are energetically more favored than all the reported 2D structures for A_2B. s-A_2B structures are direct bandgap semiconductors with high carrier mobilities. All the s-A_2B structures have unusually low lattice thermal conductivities. Moreover, s-A_2B monolayers have ultra-low Young's moduli and in-plane negative Poisson's ratios. The third work is about the phase transition in s-A_2B monolayers. We proposed two new s-A_2B structure, s(I)- and s(II)-Au_2Te. S(I)-Au_2Te is an auxetic direct-gap semiconductor, while s(II)-Au_2Te is a topological insulator. By applying strain or using thermal means, we can achieve a structural phase transition between the two phases.

Keywords: 2D materials, DFT, Structure search, Functional materials

Xin Chen, Department of Physics and Astronomy, Materials Theory, Box 516, Uppsala University, SE-751 20 Uppsala, Sweden.

Dedicated to my family

Dedicated to my teachers

List of papers

This thesis is based on the following papers, which are referred to in the text by their Roman numbers.

I **Manipulation of electronic and magnetic properties of 3d transition metal (Cr, Mn, Fe) hexamers on hraphene with vacancy defects: Insights from first principles theory**
X. Chen, Y. Liu, and B. Sanyal
J. Phys. Chem. C **124***, 7, 4270(2020)*

II **Dirac cones found in oxygen functionalized two-dimensional honeycomb and zigzag dumbbell silicene**
X. Chen, L. Li, X. Kong, F. M. Peeters, and B. Sanyal
Manuscript

III **Two-dimensional square-A2B (A = Cu, Ag, Au, and B = S, Se): Auxetic semiconductors with high carrier mobilities and unusually low lattice thermal conductivities**
X. Chen, D. Wang, X. Liu, L. Li, B. Sanyal
J. Phys. Chem. Lett. **11***, 8, 2925(2020)*

IV **PAI-graphene: a new topological semimetallic two-dimensional carbon allotrope with highly tunable anisotropic Dirac cones**
X. Chen, A. Bouhon, L. Li, F. M. Peeters, B. Sanyal
Carbon, **170***, 477(2020)*

V **Structural phase transition in monolayer gold(I) telluride: From a room-temperature topological insulator to an auxetic semiconductor**
X. Chen, L. Li, B. Sanyal
Submitted

VI **Damping-like Torque in Monolayer 1T-TaS2**
S. Husain, X. Chen, R. Gupta, N. Behera, P. Kumar, T. Edvinsson, F. G. Sanchez, R. Brucas, S. Chaudhary, B. Sanyal, P. Svedlindh, and A. Kumar
Nano Lett., **20***, 9, 6372(2020)*

Reprints were made with permission from the publishers.

Statement on my contribution

All the works in the papers are done in close collaboration with my collaborators. My own contribution is briefly listed as follows.

I take the main responsibility for planning and performing the DFT calculations, analysing the data, plotting the figures and writing the original draft. YL contributed equally in the work of paper I. In paper II and IV, the TB models are contributed by LL. In paper IV, the topological discussions are contributed by AB. In the work of papers VI, I participated in planing the theoretical part of the research and performed the DFT calculations.

Papers not included in the thesis

VII **Fingerprinting structural phase transition in SrTiO$_3$ with graphene**
S. Chen, <u>X. Chen</u>, E. Duijnstee, B. Sanyal, and T. Banerjee
Submitted

VIII **Interlayer charge transfer in tin disulphide: Orbital anisotropy and temporal aspects**
F. Johansson, <u>X. Chen</u>, O. Eriksson, B. Sanyal, and A. Lindblad
Phys. Rev. B **102***, 035165(2020)*

IX **Monolayer 1T-LaN2: Dirac spin-gapless semiconductor of p-state and Chern insulator with a high Chern number**
L. Li, X. Kong, <u>X. Chen</u>, J. Li, B. Sanyal, and F. M. Peeters
Appl. Phys. Lett. **117***, 143101(2020)*

X **Q-Carbon: A New Carbon Allotrope with a Low Degree of s–p Orbital Hybridization and Its Nucleation Lithiation Process in Lithium-Ion Batteries**
R. Lian, J. Feng, <u>X. Chen</u>, D. Wang, D. Kan, G. Chen, Y. Wei
ACS Appl. Mater. Interfaces **12***, 619(2020)*

XI **External electric field on electronic properties of water adsorbed MoS$_2$/Graphene van der Waals hetero-structures**
S. Lamichhane, <u>X. Chen</u>, H. Paudyal, N. P. Adhikari and B. Sanyal
Manuscript

XII **Carbon-rich carbon nitride monolayers with Dirac cones: Dumbbell C$_4$N**
L. Li, X. Kong, O. Leenaerts, <u>X. Chen</u>, B. Sanyal, and F. M. Peeters
Carbon **118***, 285(2017)*

Statement on my contribution

In the work of papers VII and VIII, I participated in the planing of the theoretical part of the research and performed DFT calculations. I participated in the analysis of the data, and wrote the DFT part of the original draft. In the work of papers IX, I designed and performed DFT calculations of the dynamical stability, mechanical and thermal properties, and wrote part of the original draft. In the work of paper X, I performed the VC-NEB calculations and have provided the mechanism of phase transition. For paper XI, I wrote the part of the change of charge density distribution. For paper XII, I performed part of the DFT calculations.

Contents

Part I:
Introduction & The Theoretical Background

1. Introduction

In recent years, with the remarkable development of magnetic storage and semiconductor technology, the integration of electronic components and magnetic devices has improved rapidly, which not only makes the computers smaller and faster but also makes the size effect and thermal problem more and more significant, which is hindering us from continuing to reduce the size. Because of this challenge, extensive attention from fundamental science and technology has been paid to investigate substitute materials to achieve high integration with lower energy loss. Two-dimensional (2D) materials are believed to be a promising solution of these issues.

Whether 2D materials should exist is a question that has plagued the scientific community for many years. It has been discussed in many theoretical works [1, 2]. In the last century, the theoreticians overestimated the influence of the thermal fluctuations on the lattice sheet of 2D materials and predicted that it could not be stable at a finite temperature [3, 2]. This prediction is also intimated by the fact that in many solid materials, the melting point rapidly decreases with the reduction of the thickness of samples [4, 5]. Thus it was the common opinion at that time. This question was finally solved in 2004 when K. S. Novoselov et al. realized graphene by mechanical exfoliation of graphite [6].

The synthesis of graphene is a significant achievement. That work proved that freestanding 2D materials can be thermally stable and showed that 2D materials as a new form of materials having many unusual properties. Further theoretical and experimental studies noted that graphene has high stability and novel electronic properties, such as the linear dispersion and ultrahigh carrier mobility [7, 8, 9, 10, 11]. These properties are entirely different from its three-dimensional counterpart graphite, and some features such as mobility and thermal properties are promising for a revolutionary improvement of the semiconductor technology.

For application in different fields, some properties of graphene are of practical importance, but some others are obstructive. For instance, pristine graphene is a gap-less semimetal and also without magnetic features, while for a higher I_{on}/I_{off} ratio of graphene-based field-effect transistors and application in spintronic devices, bandgap and magnetism are needed respectively. An enormous amount of studies have been conducted to manipulate the properties of graphene, and many functionalization methods have been come up with, such as cutting graphene into nanoribbons, placing graphene on different surfaces, physisorbing/chemisorbing atoms and molecules, and inserting defects [12, 13, 14, 15, 16, 17].

The enormous achievement in graphene science has inspired people to pay more attention to 2D materials in general. Beyond graphene, the monolayers of other group IV elements, i.e., post-graphene materials, are another most attractive subtopic in 2D materials studies. Post-graphene materials containing silicene, germanene, stanene, and plumbene, were first synthesized in 2012, 2014, 2015, and 2018, respectively [10, 18, 19, 11, 20]. Different from graphene, they are constructed with not only sp^2 hybridization but also sp^3. This hybridization feature makes their structures not as flat as graphene, containing two atomic layers. When stacking the layers, we can not get a Van der Waals crystal (like graphite), since the interlayer interactions arise from covalent bonds, which also implies that mechanical exfoliation is not possible for getting them. Synthesis by molecular-beam epitaxy on some substrate is the most widely used method. Among the post-graphene materials, with good connection to silicon-based microelectronics technology, the studies of silicene is the most appealing[21, 22, 23, 24, 25, 26, 27, 28, 29].

Silicon is the second lightest element in the carbon group, and many features resemble carbon. For example, they usually have sp^2 or sp^3 hybridization, and the bulk structure of silicon is also a diamond-like structure. As for the monolayer case, silicene also has a hexagonal honeycomb-like configuration, but the silicon atoms are not in the same plane (low buckled) since sp^2 bonds fail to stabilize the structure [30]. Due to the sp^2-sp^3 hybridization, there are dangling bonds in top sites of low-buckled (LB) silicene, which can be easily functionalized by chemical adsorption [31, 32, 33, 34, 35, 36, 37, 38, 39, 40]. For example, hydrogenation is a widely used method to functionalize silicene. It can introduce different properties such as bandgap and magnetism [33, 34, 35]. Notably, the adsorption of silicon atoms on LB silicene can form dumbbell-like units and stabilize the structure. The theory about the dumbbell reconstruction in silicene has nicely explained the formation mechanisms of silicene on Ag [41, 42]. Moreover, many stable silicene structures with dumbbell-like units have been predicted in those works, which may be synthesized on different substrates.

Due to the highly diverse hybridization forms, i.e., sp, sp^2 and sp^3, carbon atoms can be glued together to form different carbon allotropes in zero-dimensional (0D), one-dimensional (1D), 2D, and three-dimensional (3D) forms, such as C_{60}, carbon nanotube, graphene, and diamond [43, 44, 45, 46] respectively. The diversity is significant in 2D carbon allotropes. For example, a series of 2D carbon allotropes beyond graphene based on sp-sp^2 hybridized carbon atoms, i.e., graphyne, has also been synthesized recently [47, 48, 44]. For 2D carbon-based materials, sp hybridization is not energetically favored. Many sp^2 and sp^3 hybridization dominated graphene allotropes constructed with non-hexagonal rings are lower in energy than graphyne. Recently, there have been predictions of this kind of structures [49, 50, 51, 52, 53, 54, 55]. They have excellent stability and interesting electronic proper-

ties and are promising candidate materials for the applications in 2D materials based devices [56, 57, 58, 59, 60].

The investigation in the 2D chemical elements and compounds beyond carbon group materials have also achieved great success, such as the 2D forms of group-IV [10, 11, 19], group-V [61, 62, 63], and group-III-V [64, 65, 66], and transition metal dichalcogenides and halides (TMD and TMH) [67, 68, 69, 70, 71, 72, 73]. The 2D forms of transition metal compounds are particularly interesting since transition metal atoms also have highly diverse hybridization forms, which implies diverse structures and properties. For example, there are many different phases in 2D MoS_2, such as 1H, 1T, 1T′, and 1T″ phases. 1H-MoS_2 is a semiconductor with high carrier mobility and a direct bandgap, while 1T-MoS_2 is metallic. The 1T phase is not stable, and it usually transfers to T-prime phase, which is the distorted structure of the 1T phase, and can be seen as charge density wave states [74].

Theoretical studies are of significant importance in the investigation of 2D materials. By using first-principles calculations, we can compute the properties of 2D materials, such as energetics, electronic, magnetic, and optical properties, only if we know the crystal structure. However, the crystal structural information obtained by modern experimental techniques, e.g., transmission electron microscopy (TEM) and scanning tunneling microscopy (STM) [75, 76], is not sufficient to deduce the atomic coordinates in a unit cell, which are the most crucial input in computational materials discovery. A significant amount of research has been conducted to predict the possible structures, such as the DB silicene works mentioned in the above paragraph. The critical parameter to measure whether a structure has a high possibility to exist is its total potential energy. The lowest energy structures usually have the highest possibility to exist. However, in most cases, we can not prove a structure to be the lowest energy structure, and we can only compare it to as many as other structures. Here comes a problem: If we place atoms in random positions in a unit cell, there are infinite possibilities. By pixelating the unit cell, we can reduce the possibilities to be finite, but the number of possibilities is still huge. Actually, we do not need to map all the possibilities. We only need to get the low energy structures, which is a typical machine learning problem. Many methods were established, in which simulated annealing, metadynamics, genetic algorithms and data mining were used extensively [77, 78, 79, 80, 81, 82, 83, 84, 85, 86]. The evolutionary algorithm is one of the most efficient methods in this field. By using this method, the theoretical works of 2D materials have reduced the dependence of structural information from the experiment, and the theoretical results have become more reliable [87, 88, 89, 90, 91, 92, 93].

Two-dimensional topological insulator (2DTI), also known as quantum spin Hall (QSH) insulator, is a new state of matter with time-reversal symmetry protected edge states [94, 95, 96, 97]. In a 2DTI, the low-energy scattering of the edge state is accompanied by the time-reversal symmetry, resulting in

a non-dissipative edge transmission channel, which is expected to be applied in spintronics and quantum computing. The Quantum spin Hall (QSH) effect was first theoretically predicted in graphene by Charles Kane and Gene Mele [96]. However, since the spin-orbit coupling (SOC) effect is quite weak for the p_z orbital of carbon atoms, the small nontrivial bandgap ($\approx 10^{-3}$ meV) is not observable in the experiment. Many materials have been predicted as TIs, but only HgTe/CdTe [98] and InAs/GaSb [99] quantum wells, and very recently reported monolayer WTe_2 [100] are proved to be 2DTI experimentally at ultra-low temperature. The structure search for 2DTIs with large nontrivial bandgaps provides a possibility of increasing the working temperature.

Based on the same chemical formula, there could be many different stable crystalline structures. If these structures have distinct properties and manually controllable transition, it can be classified as phase transition materials (PTMs). They are attracting increasing research interest due to their promising applications in phase transition devices and sensors [101, 102, 103, 104, 105]. There are many examples in 3D PTMs, such as VO_2 and TaS_2: as two metal-insulator PTMs, they have been used as the channel in phase transition devices [106, 107]. Another important class of PTMs involves the transitions between different topological states. However, as a new group of matter, TI based PTMs are rarely reported. Zhou et al. have theoretically reported SnSe, with Pnma and Fm$\overline{3}$m phases is a normal-to-topological insulator PTM [108]. Transition metal dichalcogenide (TMD) monolayers are another group of promising normal-to-topological insulator PTMs. In 2H-1T′ $MoTe_2$, phase transition (insulator-metal phase transition) has been achieved in experiment by thermal means [109, 110], electrostatic doping[101], electrostatic gating [111, 105, 112]. However, the TI based PTMs have not been achieved in the experiment yet.

After the synthesis of graphene, theoretical researchers became curious about whether pentagon units can form stable 2D materials. A 2D carbon allotrope fabricated purely by pentagons, namely penta-graphene, was predicted by Zhang et al. [50]. The most special property is its mechanical property: it is an auxetic material. Auxetic materials are a class of matter with negative Poisson's ratio (NPR): with a tensile/compressive strain in one direction, the materials will expand/shrink in the vertical direction. Thus, they are also known as NPR materials. NPR materials are attracting much attention due to their novel properties such as superior toughness, robust shear resistance, and enhanced sound adsorption [113, 114, 115]. 3D auxetic materials have been studied extensively, but 2D auxetic materials are still rare. Most of the predicted in-plane NPR materials only have very small NPR, limiting their applications in NPR devices [116, 117, 118, 119].

Beyond those, there are still many other novel properties to be realized in 2D materials, such as low lattice thermal conductivity for thermoelectric applications, spin-obit torque materials, and spin-transfer torque materials for applications in spintronic devices, photocatalysis, and low-dimensional solar

16

cell. I believe that the functionalization of existing materials and searching for more stable new materials are two reliable ways to achieve those fantastic properties in two-dimensional materials.

Outline of the thesis

In this thesis, based on first-principles density functional theory, we studied various 2D materials and explored their novel properties, including structural, mechanical, electronic, magnetic, topological and thermal transport properties. The thesis contains three parts: Part I, II, and III. In Part I, the computational methods based on density functional theory (DFT) are discussed. Part II contains the results and discussion, containing two chapters, i.e., Chapter 3 and Chapter 4. In Chapter 3, I discussed the functionalization of 2D materials and have shown the modification of their properties. In Chapter 4, I have presented the prediction of three groups of new 2D materials based on global structural search and investigated their nontrivial properties and possible applications. In Chapter 5, I introduced the works in Paper VI and VII and discussed the interaction effect of 2D materials with a magnetic substrate to explain the spin-orbit torque related phenomena observed in experiments. Part III contains the final remarks of this thesis, containing the conclusions and outlooks in English and Swedish. Finally, readers can see the details of my works in the original research papers attached to this thesis.

2. The theory background and computational methods

In this chapter, the density functional theory (DFT) background and the main computational methods used in the works of the thesis are introduced. In the first section, the many-body problem and its three important approximations are introduced. Then density functional theory is introduced to solve the many-body problem.

2.1 Many-body problem

For an arbitrary system with atomic nuclei and electrons, the dynamics can be described by the Schrödinger equation:

$$H\psi = i\hbar \frac{\partial \psi}{\partial t}. \tag{2.1}$$

where the Hamiltonian can be expressed as:

$$H = -\frac{\hbar^2}{2m_i} \sum_i \nabla_i^2 - \sum_I \frac{\hbar^2}{2m_I} \nabla_I^2 - \sum_{i,I} \frac{Z_I e^2}{|\mathbf{r}_i - \mathbf{R}_I|}$$
$$+\frac{1}{2} \sum_{i \neq j} \frac{e^2}{|\mathbf{r}_i - \mathbf{r}_j|} + \frac{1}{2} \sum_{I \neq J} \frac{Z_I Z_J e^2}{|\mathbf{R}_I - \mathbf{R}_J|}. \tag{2.2}$$

where m_i, $\mathbf{r}_i$ and m_I, $\mathbf{R}_I$ denote the mass and position of the ith electron and the Ith nucleus. Since no time-dependent term is involved in the Hamiltonian, we can present the wavefunction as $\psi(\{r_i\}, t) = \phi_E(\{\mathbf{r}_i\}, t)e^{-iEt}$. And the Schrödinger equation becomes:

$$H\psi = E\psi, \tag{2.3}$$

where E denotes the total energy of system. Furthermore, since the nucleus is much massive than electron, the kinetic energy of the nuclei term can be ignored. If we use this approximation (Born-Oppenheimer's approximation [120]), the Hamiltonian can be simplified to describe the nucleus-frozen system, as:

$$H = -\frac{\hbar^2}{2m_i} \sum_i \nabla_i^2 - \sum_{i,I} \frac{Z_I e^2}{|\mathbf{r}_i - \mathbf{R}_I|}$$
$$+\frac{1}{2} \sum_{i \neq j} \frac{e^2}{|\mathbf{r}_i - \mathbf{r}_j|} + \frac{1}{2} \sum_{I \neq J} \frac{Z_I Z_J e^2}{|\mathbf{R}_I - \mathbf{R}_J|}, \tag{2.4}$$

in which the last term is fixed as a constant for a given structure with the position and charge of nucleus known. Thus we can get an electron-only Hamiltonian, writen as

$$\hat{H} = \underbrace{-\frac{\hbar^2}{2m_i}\sum_i \nabla_i^2}_{\hat{T}_e} - \underbrace{\sum_{i,I}\frac{Z_I e^2}{|\mathbf{r}_i - \mathbf{R}_I|}}_{\hat{V}_{ext}} + \underbrace{\frac{1}{2}\sum_{i \neq j}\frac{e^2}{|\mathbf{r}_i - \mathbf{r}_j|}}_{\hat{V}_{ee}} \qquad (2.5)$$

In this Hamiltonian, there are three terms. The first term $\hat{T}_e$ represents the kinetic energy. An important challenge is that when electrons move in high and different velocities, the masses are actually not a constant m_e due to the relativistic effect. But to simplify the problem, this effect is just not taken into account. The second term $\hat{V}_{ext}$ is the external potential energy functional of the electrons due to the frozen nucleus. The third term $\hat{V}_{ee}$ is the Coulomb repulsion induced potential energy functional. Since electrons are not frozen, to obtain this term, a proper treatment needs a many-body wavefunction containing 3N variables, which is not possible to be exactly calculated in systems with more than two electrons.

The first method to solve this problem is proposed by Hartree, where the interaction between electrons can be averaged, and every electron can be treated as in the effective potential of other N-1 electrons. Thus every electron is only characterized by the electron density distribution of the N-1 electrons and not relevant to the specific position of the N-1 electrons. All electrons are moving independently, and thus the many-body electron wavefunction can be simplified as a product of single-electron wavefunctions. Then we can get the single electron Hamiltonian equations by using the variational principle. The problem in this approximation is that since the electrons are Fermions, the Pauli exclusion principle should be considered.

To consider this principle, Hartree-Fock formalism has been proposed. In this theorem, the many-body wavefunction is constructed in a Slater determinantal form. This is a big improvement that, in the derived Hamiltonian equation, an extra potential (exchange potential) is introduced. Moreover, in many small systems, this method can nicely describe the system. However, in the Hartree-Fock formalism, the electron correlation effect is not considered, making the method still not accurate.

Both Hartree and Hartree-Fock are based on the wave functions, and therefore for large systems, this method needs a large number of computational resources. For an N-electron system, 4N variables are needed to construct the wave function. Thus the complexity increases sharply with the increase in the number of electrons. In view of that, a density functional-based approach has been well developed and widely used in computational studies of condensed matter physics and chemistry. In contrast to the wave function-based methods, in an N-electron system, the degree of freedom of electron density is only

four (three spatial and a spin variable), which is much more achievable in large systems.

2.2 Density functional theory

2.2.1 Hohenberg-Kohn theorems

The density functional theory (DFT) is based on the fact that any property of a system can uniquely be determined by the ground state density $n_0(r)$, [121, 122] which established a vital milestone in 1964 by Hohenberg and Kohn [123], and unraveled an exact theory of interacting many-body systems, based on the two statements:

Firstly, for a system only containing equivalent Fermi particles without considering spins, the ground state energy is the unique function of the particle density distribution function $\rho(r)$. So we can fully determine a system without knowing the wavefunctions (without considering the spin densities).

The second one is that the energy function E[ρ] attains its minimum when ρ corresponds to the ground state, and $E[\rho]_{min}$ becomes the ground state energy. This theorem is a variational principle of density functional theory, which provides a method for applying variational methods to solve specific problems.

Hohenberg-Kohn formalism reveals that the particle density function ρ is the essential variable of the properties of a many-body system's ground state. The variation of the energy functional E[ρ] is a route to determine the ground state of a system.

In summary, according to Hohenberg and Kohn theorem, the ground state energy and particle density function can be determined by the minimum of:

$$E[\rho] \equiv \int d\mathbf{r} v_{ext}(\mathbf{r})\rho(\mathbf{r}) + <\psi|T+U|\psi>, \qquad (2.6)$$

in which $v_{ext}(\mathbf{r})$ is the external potential energy of point $\mathbf{r}$, T is the kinetic energy of electrons, U is the interaction energy among electrons.

The $<\psi|T+U|\psi>$ term in Equation 2.6 can be written as:

$$<\psi|T+U|\psi> = T[\rho] + \underbrace{\frac{1}{2}\int d\mathbf{r}d\mathbf{r}' \frac{\rho(\mathbf{r})\rho(\mathbf{r}')}{|\mathbf{r}-\mathbf{r}'|}}_{J_{Hartree}} + E_{ncl}[\rho], \qquad (2.7)$$

in which the first and second terms are the kinetic energy functional and Coulomb interactions among electrons (Hartree term), respectively. The third term $E_{ncl}[\rho]$ is the non-classical term, including the self-interaction, exchange, and correlation effects. By minimizing the energy functional $E[\rho(\mathbf{r})]$, one can obtain the ground state density distribution and the corresponding total energy. However, only the external potential term in Equation 2.6 and the Hartree term in Equation 2.7 are known, while the explicit form of other terms are still needed to be determined.

2.2.2 Kohn-Sham formalism

To get a proper solution to the unknown terms in the Hohenberg-Kohn equation, a practical approach was presented by W. Kohn and L. J. Sham [124]. The Kohn-Sham formalism is to replace the kinetic energy (T) and non-classical term (E_{ncl}) of the many-body system by a summation of the exact kinetic energy of a non-interacting system (T_s) with the same charge density distribution and a $exchange-correlation$ term (E_{XC}). Then we get

$$
\begin{aligned}
T[\rho(\mathbf{r})] + J_{Hartree}[\rho(\mathbf{r})] & + E_{ncl}[\rho(\mathbf{r})] \\
& = T_s[\rho(\mathbf{r})] + J_{Hartree}[\rho(\mathbf{r})] + E_{xc}[\rho(\mathbf{r})],
\end{aligned} \tag{2.8}
$$

in which the Hartree term is already defined in Equation 2.7, and the $T_s[\rho\mathbf{r}]$ term is described by a functional of the single-electron Kohn-Sham orbitals ($\phi_i(\mathbf{r})$), as

$$
T_s[\rho(\mathbf{r})] = -\frac{\hbar^2}{2m_e} \sum_{i=1}^{occ} \langle \psi_i | \nabla_i^2 | \psi_i \rangle . \tag{2.9}
$$

Thus the energy functional of the system can be written as

$$
E_{KS}[\rho(\mathbf{r})] = T_s[\rho(\mathbf{r})] + J_{Hartree}[\rho(\mathbf{r})] + V_{ext}[\rho(\mathbf{r})] + E_{xc}[\rho(\mathbf{r})]. \tag{2.10}
$$

In this formalism, the T_s and $J_{Hartree}$ term just about the distribution of electrons and are universal for any system. Different structures have different external potentials (V_{ext}), which make them show different electronic properties. The exchange-correlation term is not exactly described yet (it will be discussed in the next section), but we can obtain the ground state energy form by employing the Hohenberg-Kohn theorem.

The ground state can be obtained by minimizing the energy functional. The minimum of the energy functional with respect to the electron distribution $\rho(\mathbf{r})$ can be described by the Schrödinger-like Kohn-Sham equation, as

$$
H_{KS}(\mathbf{r})\psi_i(\mathbf{r}) = \left[-\frac{1}{2}\nabla^2 + V_{KS}(\mathbf{r}) \right] \psi_i(\mathbf{r}) = \varepsilon_i \psi_i(\mathbf{r}), \tag{2.11}
$$

In which

$$
V_{KS}(\mathbf{r}) = V_{ext}(\mathbf{r}) + V_{Hartree}(\mathbf{r}) + V_{xc}(\mathbf{r}), \tag{2.12}
$$

in which $V_{Hartree}$ is the Hartree potential, written as

$$
V_{Hartree} = \int \frac{\rho(\mathbf{r}_2)}{|\mathbf{r} - \mathbf{r}_2|} d\mathbf{r}_2. \tag{2.13}
$$

The term V_{xc} is the exchange-correlation potential, which is the partial derivative of the exchange-correlation energy E_{XC}, written as

$$
V_{xc} = \frac{\delta E_{xc}[\rho(\mathbf{r})]}{\delta\rho(\mathbf{r})}. \tag{2.14}
$$

Then the electron density distribution of the ground state can be computed by:

$$\rho(\mathbf{r}) = \sum_{i=1}^{occ} |\psi_i(\mathbf{r})|^2. \tag{2.15}$$

Then, we can calculate the total energy by the sum of the occupied eigenstate energy values.

Now, the only thing left in the equation is the exchange-correlation term $E_{XC}[\rho(\mathbf{r})]$, for which several efficient approximations have been proposed.

2.3 Exchange-correlation functionals

2.3.1 Local density approximation

Based on the Hohenberg-Kohn-Sham equation, the many-body system can be calculated by a single particle model. However, finding a good E_{xc} is very important in the calculation.

Many approximations have been suggested to find a good E_{xc}, among which the local density approximation (LDA) proposed by W. Kohn and L. J. Sham is widely used.[124] This method is basically approximating the exchange-correlation functional of electrons using that of the uniform electron gas, $\varepsilon_{xc}[\rho(\mathbf{r})]$.

$$E_{xc}(\rho) = \int d\mathbf{r}\rho(r)\varepsilon_{xc}[\rho(\mathbf{r})] \tag{2.16}$$

The exchange-correlation potential is approximated as:

$$V_{xc}[\rho(\mathbf{r})] = \frac{\delta E_{xc}[\rho]}{\delta\rho} = \frac{d}{d\rho(r)}(\rho(r)\varepsilon_{xc}[\rho(\mathbf{r})]) \tag{2.17}$$

It is feasible to get ε_{xc} in uniform electron gas with different ρ, and then get $\rho(\mathbf{r})$ using interpolation. The exchange-correlation term ε_{xc} can be divided into exchange term ε_x and correlation term ε_c. The exchange term ε_x is present by Dirac as:

$$\varepsilon_x(\rho) = -\frac{3}{4}[\frac{3\rho}{\pi}]^{1/3}. \tag{2.18}$$

While for the correlation part, an analytical solution is not available. In general, it can be parameterized from the results obtained from Quantum Monte Carlo simulations.

Comparing the LDA results with experimental results, it is found that LDA usually has some systematic problems, such as overestimation of the binding energy and underestimation of the bond length and bandgap. Moreover, for the systems in which electron density is extremely uneven, for example, transition metal oxide systems, LDA does not perform well. Since the electron

distribution is not uniform, the exchange-correlation energy in each position is quite dependent on the electron density of other positions. Thus the LDA is not good enough to give a reliable result.

2.3.2 Generalized-gradient approximation

A commonly used improvement over LDA is to let the exchange-correlation energy density in a small space not only be related to the local electron density in the space but also to the near neighbor space.[123] Thus, the first-order correction of exchange-correlation energy density is made taking electron density gradient into account,

$$E_{xc}[\rho] = \int d\mathbf{r} \varepsilon_{xc}[\rho(\mathbf{r}), |\nabla \rho(\mathbf{r})|]. \tag{2.19}$$

Many Generalized-gradient approximation (GGA) based methods have been proposed, such as Perdew-Wang (PW91)[125], Perdew-Burke-Ernzerhof (PBE)[126, 127], etc.

2.3.3 Hybrid functional

Since the exchange-correlation term is not exactly described in LDA and GGA, some properties such as the bond lengths, energy band gaps are quite different from experimental results. To improve the results, hybrid functional methods are proposed by A. Beck.[128] This method uses the hybrid exchange-correlation energy functional, which is usually a linear combination of Hartree-Fock exchange E_x^{HF} and LDA or GGA exchange-correlation energy functional.

Many hybrid functional methods are proposed, such as B3LYP, PBE0, etc.[129, 130] In this thesis, a Heyd-Scuseria-Ernzerhof (HSE) exchange-correlation functional[131] is used to correct the band structures.

2.4 Solving the KS equation in periodic crystals

2.4.1 Periodic boundary conditions and the basis sets

The equations above can only be solved for systems with finite electrons such as molecules and atoms, but crystal systems always have infinite electrons. In a solid crystal system, the periodicity can provide the equations a periodic boundary condition, which can be used to simplify and solve the KS equations.

In a periodic crystal with lattice translational vector $\mathbf{R}$, the effective potential V_{KS} satisfies:

$$V_{KS}(\mathbf{r} + \mathbf{R}) = V_{KS}(\mathbf{r}). \tag{2.20}$$

The KS wave function satisfies the boundary condition:

$$\psi_{l,\mathbf{k}}(\mathbf{r} + \mathbf{R}) = e^{i\mathbf{k}\cdot\mathbf{R}}\psi_{l,\mathbf{k}}(\mathbf{r}), \tag{2.21}$$

$$\psi(l,\mathbf{r}) = e^{i\mathbf{k}\cdot\mathbf{r}}w_{l,\mathbf{k}}(\mathbf{r}), \tag{2.22}$$

and

$$w_{l,\mathbf{k}}(\mathbf{r}) = w_{l,\mathbf{k}}(\mathbf{r} + \mathbf{R}) \tag{2.23}$$

in which $\mathbf{k}$ is the Bloch wave vector, l is the band index, $\psi_{l,\mathbf{k}}(\mathbf{r})$ is the Bloch wave function, and $w_{l,\mathbf{k}}(\mathbf{r})$ is the periodic function.

The accurate description of the wave function needs a good complete basis set. The basis set should include all the regions in the crystal. There are several basis sets with different approximations, such as the linearized augmented plane waves (LAPW), the linear combination of atomic orbitals (LCAO), and plane waves (PW). In this section, we just introduce the PW approximation.

We can write the periodic wave function as a Fourier series, i.e.,

$$w_{l,\mathbf{k}} = \sum_{\mathbf{G}} c_{l,\mathbf{G}}e^{i\mathbf{G}\cdot\mathbf{r}}, \tag{2.24}$$

in which $\mathbf{G}$ is the reciprocal lattice vector satisfying $\mathbf{G}\cdot\mathbf{r} = 2\pi m$, where m is an interger. $c_{l,\mathbf{G}}$ is the PW expansion coefficient. The we can write the KS orbitals as a linear combination of the complete PW basis set $e^{i(\mathbf{k}+\mathbf{G})\cdot\mathbf{r}}$, i.e.,

$$\psi_{l,\mathbf{k}}(\mathbf{r}) = \sum_{\mathbf{G}} c_{l,\mathbf{k}}(\mathbf{G}) \times \frac{1}{\sqrt{\Omega}}e^{i(\mathbf{k}+\mathbf{G})\cdot\mathbf{r}}, \tag{2.25}$$

in which $c_{l,\mathbf{k}}$ is the expansion coefficient of the basis set, and $\frac{1}{\Omega}$ is the normalization factor (Ω is the volume). The KS equation is written as

$$\left(-\frac{\hbar^2}{2m_e}\nabla^2 + V_{KS}(\mathbf{r})\right)\psi_{l,\mathbf{k}} = \varepsilon_{l,\mathbf{k}}\psi_{l,\mathbf{k}}(\mathbf{r}), \tag{2.26}$$

By multiplying from the left by $e^{-i(\mathbf{k}+\mathbf{G}')\cdot\mathbf{r}}$ and integrating over $\mathbf{r}$, we get

$$\sum_{\mathbf{G}'}\left(\frac{\hbar^2}{2m_e}|\mathbf{k}+\mathbf{G}|^2\delta_{\mathbf{G}'\mathbf{G}} + V_{KS}(\mathbf{G}-\mathbf{G}')\right)c_{l,\mathbf{k}}(\mathbf{G}) = \varepsilon_{l,\mathbf{k}}c_{l,\mathbf{k}}(\mathbf{G}). \tag{2.27}$$

In the equation, the effective potential energy V_{KS} is in terms of Fourier transforms and the kinetic energy is diagonal. Thus we can diagonalize the Hamiltonian matrix $H_{\mathbf{k}+\mathbf{G},\mathbf{k}+\mathbf{G}'}$ and solve the equation.

The calculation size is determined by the choice of cutoff energy

$$E_{cutoff} = \frac{\hbar^2}{2m_e}|\mathbf{k}+\mathbf{G_{max}}|^2. \tag{2.28}$$

To get a meaningful solution, the valence and core electrons should be considered, but it is very expensive. The problem is simplified by pseudopotential approximations in the following chapter.

2.4.2 Pseudopotentials

In a crystal, the core electrons are tightly bound to the nuclei. The interaction between the wave function of the core electrons and the crystalline environment is very weak, and thus we can combine the core electron potential and the nuclear Coulomb potential to reduce the number of electrons to be computed. The combined potential is the pseudopotential, and the method is named as Frozen-Core-Approximation.

As shown in Fig. 2.1, in the core region (the green part) the pseudopotential V^{ps} replaces the steep ionic potential $V^{ae} = -\frac{Z}{r}$ with a much weaker effective potential. The corresponding wavefunctions Ψ^{ae} are replaced with pseudowavefunctions Ψ^{ps}. Beyond the core region, the pseudopotential V^{ps} and the all-electron potential are identical, and thus corresponding pseudowavefunctions and all-electron wavefunctions are also identical. Unlike the all-electron wavefunctions, the pseudowavefunctions do not have nodal structures, making it possible to describe the pseudowavefunctions with a small number of PWs.
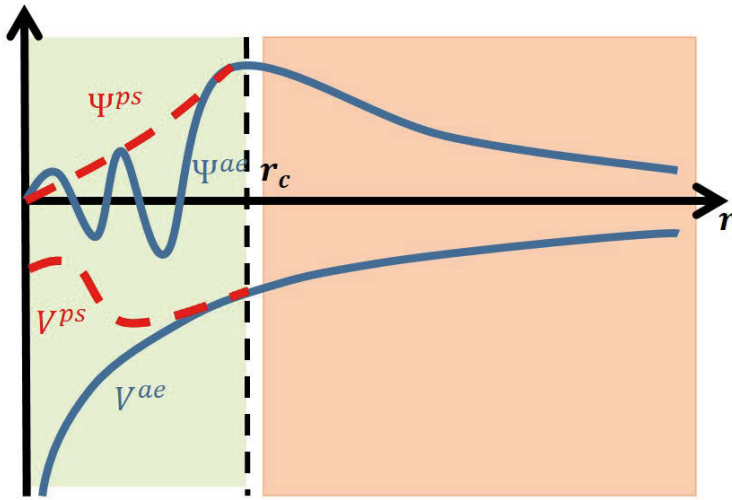

Figure 2.1. The mechanism of constructing pseudopotential. The solid blue lines show the all-electron wavefunction Ψ^{ae} and the ionic potential V^{ae}. The dashed lines show the pseudowavefunction Ψ^{ps} and pseudopotential V^{ps}. **r** is the distance from nuclear. When $\mathbf{r} > \mathbf{r_c}$, the pseudowavefunction and pseudopotential coincide with the all-electron wavefunction and ionic potential.

The construction of the pseudopotential is based on orthogonalised-plane-wave approach. For an atom with core and valence stats $|\psi_c\rangle$ and $|\psi\rangle$, with Hamiltonian $\hat{H}$, the Schrödinger equation becomes

$$\hat{H}|\psi_c\rangle = E_c|\psi_c\rangle, \quad and \quad \hat{H}|\psi_v\rangle = E_v|\psi_v\rangle, \tag{2.29}$$

25

in which E_c and E_v are the energy eigenvalues of core electrons and valence electrons, respectively. We can write the wavefunction of the valence electrons as a linear combination of the core states and the pseudowavefunctions, as

$$|\psi_v\rangle = \sum_c |\psi_c\rangle a_{cv} + |\psi^{ps}\rangle, \tag{2.30}$$

In which the coefficient a_{cv} is for the oscialting region. Limited by the orthogonality condition,

$$\langle \psi_c | \psi_v \rangle = 0. \tag{2.31}$$

Thus, multiplying Equation 2.30 by $\langle \psi_c |$ from the left, we can get

$$0 = \langle \psi_c | \psi^{ps} \rangle + a_{cv}. \tag{2.32}$$

And thus

$$|\psi_v\rangle = |\psi^{ps}\rangle - \sum_c |\psi_c\rangle \langle \psi_c | \psi^{ps} \rangle. \tag{2.33}$$

Thus the left side of the Schrödinger equation Equation 2.29 become

$$\hat{H}|\psi_v\rangle = \hat{H}|\psi^{ps}\rangle - \hat{H}\sum_c |\psi_c\rangle \langle \psi_c | \psi^{ps} \rangle = \hat{H}|\psi^{ps}\rangle - \sum_c E_c |\psi_c\rangle \langle \psi_c | \psi^{ps} \rangle. \tag{2.34}$$

The right side is

$$E_v|\psi_v\rangle = E_v \left(1 - \sum_c |\psi_c\rangle \langle \psi_c | \right) |\psi^{ps}\rangle \tag{2.35}$$

The Schrödinger equation become

$$\hat{H}|\psi^{ps}\rangle + \sum_c (E_v - E_c)|\psi_c\rangle \langle \psi_c | \psi^{ps} \rangle = E_v |\psi^{ps}\rangle. \tag{2.36}$$

Thus for the pseudowavefunction,

$$\left(\hat{H} + \hat{V}_{nl}\right) |\psi^{ps}\rangle = E_v |\psi^{ps}\rangle, \tag{2.37}$$

in which

$$\hat{V}_{nl} = \sum_c (E_v - E_c)|\psi_c\rangle \langle \psi_c |. \tag{2.38}$$

We can combine $\hat{V}_{nl}$ with the effective potential term $\hat{V}_{eff}$ in the Hamiltonian, and then we get the pseudopotential as

$$\hat{V}^{ps} = \hat{V}_{eff} + \hat{V}_{nl}. \tag{2.39}$$

From these formulae, we see that $\hat{V}_{ps}$ is weaker than the real potential since $\hat{V}_{nl}$ localized in the core region is repulsive in nature and it cancels parts of the Coulomb potential in $\hat{V}eff$.

2.4.3 Projector Augmented Wave method

In this thesis, most of the DFT calculations are performed on the base of the projector augmented wave (PAW) [132, 133] based density functional code, Vienna Ab initio Simulation Package (VASP)[134, 135].

The projector augmented wave (PAW) method is adapted from the pseudopotential method and is first introduced by Blöch. PAW method is an all-electron method. It divides the space into two regions: the augmented (core) region and the rest region. The core region is the sphere around each nucleus, which is less system-dependent and less interested. The result region is the most important region for studying the properties of solids. The PAW method's strategy is to divide the wavefunction into two parts: the wavefunction in the augmented area and the wavefunction in the other area. The two wavefunctions are connected continuously at the interface of the two regions. For the real all-electron wave function $\psi(\mathbf{r})$, the number of the partial waves $\phi(\mathbf{r})$ needed in the core region is huge, thus we need an smooth auxiliary wavefunction ($\tilde{\psi}(\mathbf{r})$) to describe it with less numbers of partial wavefunctions $\tilde{\phi}(\mathbf{r})$. Since the core region is usually not much influenced by the chemical environment, we can just take the eigenfunctions of isolated atoms to describe the electrons in the core region. Outside the core region, the auxiliary pseudo wavefunctions and the all-electron wavefunctions should be identical. The relationship between the real all-electron wavefunction and the auxiliary pseudo wavefunction can be described by a linear transformation $\mathcal{T}$, as

$$\phi_i(\mathbf{r}) = \mathcal{T}\tilde{\phi}_i(\mathbf{r}) \quad \text{(outside the core region)}, \tag{2.40}$$

in which

$$\mathcal{T} = 1 + \sum_R \mathcal{T}_R, \tag{2.41}$$

$\mathcal{T}_R$ is always zero outside the core region Ω_R, and i is the index of angular momentum lm.

For the core states, the partial wavefunctions are orthogonal. Thus the all-electron wavefunction can be written as a linear combination of the partial wave.

$$|\psi(\mathbf{r})\rangle = \sum_i p_i |\phi_i(\mathbf{r})\rangle \quad \text{(in the core region)}, \tag{2.42}$$

in which p_i is the expansion coefficient of the plane wave ϕ_i.

Outside the core region, the all-electron wavefunction and the pseudo wavefunctions should be identical. Thus we get

$$\phi_i(\mathbf{r}) = \tilde{\phi}_i(\mathbf{r}) \quad \text{(outside the core region)} \tag{2.43}$$

The operator $\mathcal{T}_R$ can be obtained by the relationship

$$\mathcal{T}_R|\tilde{\phi}_i\rangle = |\phi_i\rangle - |\tilde{\phi}_i\rangle. \tag{2.44}$$

Since $\mathcal{T}$ is a linear operator, we can write the coefficients p_i in the form

$$p_i = \left\langle q_i \mid \tilde{\psi} \right\rangle, \tag{2.45}$$

in which $|q_i\rangle$ are a set of project functions. The functions satisfy the relation of completeness and orthogonality, as

$$\sum_i \left| \tilde{\phi}_i \right\rangle \langle \tilde{q}_i | = 1, \tag{2.46}$$

and

$$\left\langle \tilde{\phi}_i \mid \tilde{q}_j \right\rangle = \delta_{i,j}. \tag{2.47}$$

Thus we can write the pseudo wavefunction as

$$|\tilde{\psi}\rangle = \sum_i \left| \tilde{\phi}_i \right\rangle \left\langle \tilde{q}_i \mid \tilde{\psi} \right\rangle. \tag{2.48}$$

Utilizing the linear operator $\mathcal{T}_R$ in Equation 2.48, the all-electron wavefunction can be described by

$$
\begin{aligned}
|\psi\rangle &= |\tilde{\psi}\rangle + \sum_i \left(|\phi_i\rangle - |\tilde{\phi}_i\rangle \right) \left\langle \tilde{q}_i \mid \tilde{\psi} \right\rangle \\
&= |\tilde{\psi}\rangle - \underbrace{\sum_i \left| \tilde{\phi}_i \right\rangle \left\langle \tilde{q}_i \mid \tilde{\psi} \right\rangle}_{\text{Pseudo onsite}} + \underbrace{\sum_i \left(|\phi_i\rangle \left\langle \tilde{q}_i \mid \tilde{\psi} \right\rangle \right)}_{\text{All electron onsite}},
\end{aligned} \tag{2.49}
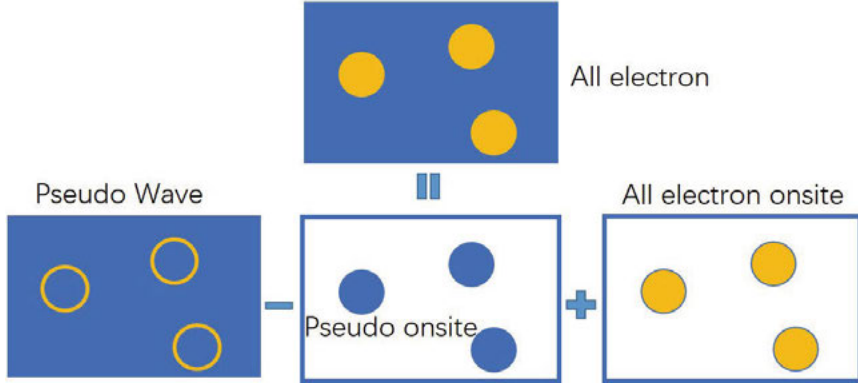$$

as indicated in Fig. 2.2.

Figure 2.2. The mechanism of constructing PAW all electron wave function.

Then we can get the exact form of the operator between the pseudo wavefunction and the real all-electron wavefunction, as

$$\mathcal{T} = 1 + \sum_i \left(|\phi_i\rangle - |\tilde{\phi}_i\rangle \right) \langle \tilde{q}_i |. \tag{2.50}$$

Using the transform operator, the Kohn-Sham equation can be written as

$$(\tilde{H} - \varepsilon\tilde{O})|\tilde{\psi}\rangle = 0, \text{in which}$$
$$\tilde{H} = \mathcal{T}^\top H \mathcal{T} \text{ and } \tilde{O} = \mathcal{T}^\top \mathcal{T}. \tag{2.51}$$

2.5 Hellmann-Feynman force

In a DFT calculation, to optimize the structure to the local minimum in the energy surface, we can compute the first derivative of the energy surface (force). At the local minimum, the first derivative of the energy surface should be exactly zero.

The force on an atom can be computed by the first derivative of energy E, as

$$F_i = -\frac{\partial E}{\partial R_i}, \tag{2.52}$$

in which R_i is the position of the atom i, and

$$E = \frac{\langle\psi|H|\psi\rangle}{\langle\psi\mid\psi\rangle} = \langle\psi|H|\psi\rangle. \tag{2.53}$$

By substituting E in Equation 2.52, we get

$$F_i = -\left\langle\psi\left|\frac{\partial H}{\partial R_i}\right|\psi\right\rangle - \left\langle\frac{\partial\psi}{\partial R_i}|H|\psi\right\rangle - \left\langle\psi|H|\frac{\partial\psi}{\partial R_i}\right\rangle. \tag{2.54}$$

By substituting $H|\psi\rangle$ with $E|\psi\rangle$, we get

$$F_i = -\left\langle\psi\left|\frac{\partial H}{\partial R_i}\right|\psi\right\rangle - E\left(\frac{\partial\langle\psi\mid\psi\rangle}{\partial R_i}\right) = -\left\langle\psi\left|\frac{\partial H}{\partial R_i}\right|\psi\right\rangle. \tag{2.55}$$

Equation 2.55 is the representation of the Hellmann-Feynman force. In a geometry optimization calculation, the Hellmann-Feynman force on each atom should be smaller than the convergence criteria.

2.6 Born-Oppenheimer molecular dynamics

In most works of this thesis, Born-Oppenheimer molecular dynamics (BOMD) simulations have been performed using VASP to simulate the diffusion process or evaluate the thermal stability of structures. BOMD is a type of ab initio molecular dynamics (AIMD), which is widely used in many fields such as simulating the chemical reaction process, simulating the phase transition process, and checking dynamical stability.

BOMD is based on statistical mechanics, Newtonian dynamics, density functional theory, and Born-Oppenheimer approximation. The main idea is to treat

electrons and nucleus separately since electrons' velocity is much faster than the nucleus. The electronic ground states are computed by the Kohn-Sham equation. Then we can get the energy of the system. As mentioned before, the force can be computed by using the Hellman-Feynman force theorem

$$\mathbf{F}_i = -\left\langle \psi \left| \frac{\partial \mathbf{H}}{\partial \mathbf{R}_i} \right| \psi \right\rangle , \tag{2.56}$$

in which ψ is the ground-state wavefunction, $\mathbf{R}_i$ is the position of the atom i. The temperature is added as a term of the Hamiltonian H. Then we treat the nucleus as classic particles, whose motion is following Newton's second law, as

$$m_i \ddot{\mathbf{R}}_i = -\frac{\partial E}{\partial \mathbf{R}_i} = \mathbf{F}_i. \tag{2.57}$$

The process of the BOMD can be described as the following steps. First, the structure is initialized with knowing the position of each atom and the corresponding initial momenta. Then the forces on each atom are computed by using the Hellman-Feynman theorem, and the motion equations are obtained. Then compute the atomic position and momenta in the next timestep and repeat the above two steps for a sufficient number of simulation time.

2.7 Relativistic effect and spin-orbit coupling

In our calculations of magnetic anisotropy energies and some of the electronic band structure calculations, spin-orbit coupling (SOC) is considered.

Spin-orbit coupling generates from the relativistic character of electrons. For electrons moving in the presence of an electromagnetic field, the 4-vector Dirac equation can be written as:[136].

$$i\hbar \frac{\partial}{\partial t} \Psi = (c\alpha \cdot \pi + \beta m_0 c^2 + V)\Psi \tag{2.58}$$

in which $\alpha = \begin{pmatrix} 0 & \sigma \\ \sigma & 0 \end{pmatrix}$ (σ is the Pauli matrix of spin of electrons), $\beta = \begin{pmatrix} I_{2\times2} & 0 \\ 0 & -I_{2\times2} \end{pmatrix}$, $\pi = p + e\mathbf{A}$, $V(x) = -e\varphi$, I is the identity matrix. e is positive, denoting a positive charge, $\mathbf{A}$, φ denotes the vector potential and scalar potential. Dirac wavefunction Ψ describes the positive/negative energy states. The term β shows that the positive and negative energy states have a Dirac energy gap of about $2m_0 c^2$. the term $c\alpha \cdot \pi$ can relate the two states and the strength of the relation is proportional to the electron momentum π. Commonly, the correlation of positive and negative energy states can be treated as a perturbation, and the Dirac equation is changed into:

$$i\hbar \frac{\partial}{\partial t} \Psi = [\frac{(\sigma \cdot \pi)^2}{2m_0} + V + \frac{\hbar}{4m_0^2 c^2}(\nabla V \times \pi) \cdot \sigma +$$
$$\frac{\hbar^2}{8m_0^2 c^2}\nabla^2 V - \frac{(\sigma \cdot pi)^4}{8m_0^3 c^2}]\Psi \tag{2.59}$$

Spin-orbit coupling term reads as $H_{SO} \equiv \frac{\hbar}{4m_0^2 c^2}(\nabla V \times \pi) \cdot \sigma$. The strength is proportional to the momentum of electrons and the electric field strength $E \equiv (1/e)\nabla V$.

With SOC term, the Kohn-Sham Hamiltonian becomes:

$$H = H_{KS} + H_{SOC}, \tag{2.60}$$

$$H_{SOC} = \xi \mathbf{S} \cdot \mathbf{L}, \tag{2.61}$$

$$\xi = -\frac{e}{2c^2 m_0^2 r} \frac{dV_{eff}(\mathbf{r})}{dr}. \tag{2.62}$$

In the Hamiltonian, $\mathbf{L} = \mathbf{r} \times \mathbf{p}$ denotes the orbital angular momentum, $\mathbf{S} = 1/2\sigma$ is the spin of an electron. SOC parameter ξ is relevant to the element type and is more important in systems containing heavy atoms such as Au, Pb, Bi, etc. By changing the parameter ξ, we can investigate the influence of the SOC effect on systems and study relevant properties.

2.8 Evolutionary structure search

The crystal structure is the most crucial input in first-principles calculations. However, limited by experimental techniques, in some cases, especially in 2D systems, the crystal structures cannot be directly obtained. Deducing the crystal structure from the indirect experimental observations is sometimes quite hard. Many research interests have been conducted to predict the possible structures, and one of the most famous examples is the prediction of the DNA and RNA structure. The critical parameter to measure whether a structure has a high possibility to be stable is its total energy. In most cases, we can not prove a structure to be the lowest energy structure, but we can compare it to as many structures available.

Many methods have been established for the structure prediction [84, 85, 86], among which the evolutionary algorithm is one of the most efficient methods. By using this method, the theoretical works of 2D materials have been reduced the dependence of structural information from the experiment, and the theoretical results have become more reliable [91, 92, 93].

The procedures of a evolutionary structure search using USPEX code [89, 82, 137] are shown in Fig. 2.3:

(I) The essential inputs are the chemical composition, the size of the unit cell, the thickness of the slab (for 2D materials only).

(II) For the first generation, the initial structures are generated under constraints such as inter-atomic distance, slab thickness, and the extent of the vacuum in the unit cell. In the process, space groups are randomly chosen to construct the structures. Moreover, to speed the structure search, we can also take some know structures with low energies as seed structures.

(III) Then the initial structures will be optimized with DFT codes. After full geometry optimization, we will get the local minimum energy structures and the corresponding energies.

(IV) The low energy structures in step III will become the seed structures for the next generation through heredity, permutation, and mutation. For getting the global lowest energy structure, the structures with lower energies will have a higher possibility of being used as parent structure. Moreover, there are also some structures generated randomly as the new generation structures.

(V) Then repeat the loop from step III until the convergence criterion is satisfied. The convergence criterion is that in several latest generations, the lowest energy structures do not get modified anymore. The structure with the absolute minimum energy is regarded as the global minimum structure in the structure search.

The operators in step IV is of vital importance. The heredity operator is to cut the unit cell into several parts and then gather the parts to form a new structure. The permutation operator swaps the chemical composition between different structure blocks. There are two types of mutation operators. One of them is the coordinate mutation: it moves the center of structure blocks in a random direction to build a new structure. The other is the rotational mutation: it rotates randomly selected structure blocks with random angles. Usually, the two mutation operators are used together, i.e., they move the structure blocks and rotate with random angles. In this thesis, the evolutionary algorithm is employed in predicting PAI-graphene, s-A_2B (A=Cu, Ag, Au; B=S, Se), and s-Au_2Te in Chapter 4 for searching low energy 2D structures.

2.9 Nudged elastic band

The nudged elastic band (NEB) method[138] is efficient for finding the lowest energy transition paths between two structures. In an NEB calculation, the transition paths are a series of images that are initially guessed by interpolation of initial and final structures. Then they will be optimized to find the lowest energy paths. In this period, the spacing between neighbor images is kept equally by using spring forces on the direction of neighboring images. When the force satisfies the convergence criteria, the transition path is the lowest energy path.

One of the most significant drawbacks of this method is that enormous images are needed to reach the saddle point, which is essential for getting the energy barrier. An improved method, i.e., climbing image NEB (cNEB), was proposed to solve the problem [139]. In a cNEB calculation, the spring force for the highest energy image (climbing image) is removed. The images are optimized to maximize the energy curve maximum of the phase transition path and minimize it in other directions. With this method, we can get the exact saddle points with fewer images and computational time.
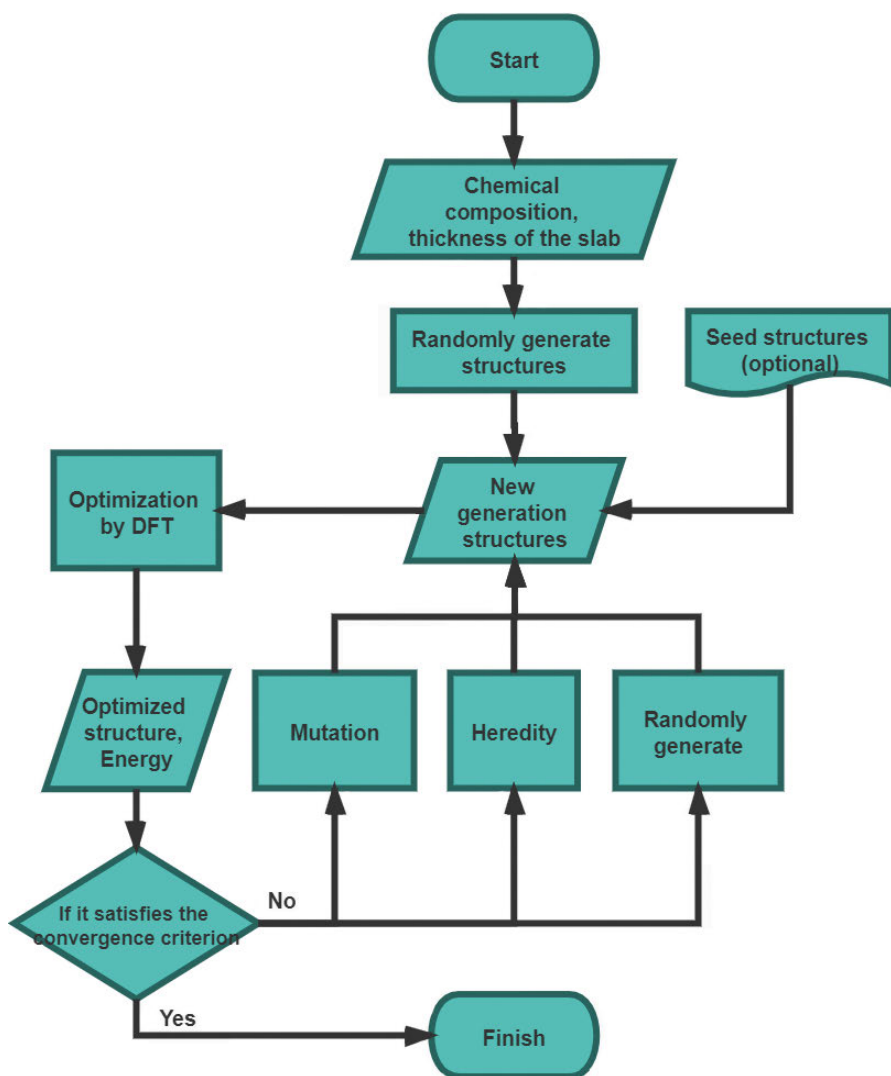
Figure 2.3. The procedures of performing a DFT based evolutionary structure prediction.

2.10 Calculations for the properties of two-dimensional materials

2.10.1 Theoretical calculations for lattice thermal conductivity

In a solid material, heat is conducted by both electrons and phonons (lattice vibrations). In a semiconductor, the dominant heat transfer is via phonon thermal conduction. The thermal current J driven by temperature gradient ∇T can be computed by

$$J = \sum_{\nu} \int f_\lambda \hbar \omega_\lambda v_\lambda \frac{dq}{(2\pi)^3}, \tag{2.63}$$

in which λ is the phonon mode index, $\lambda \equiv (\nu, \mathbf{q})$, where the ν and $\mathbf{q}$ are the phonon branch index and the wavevector, respectively. ω_λ is the angular frequency of mode λ, and v_λ is the group velocity. f_λ is the distribution function of mode λ. Under thermal equilibrium condition, the distribution can be described by the Bose-Einstein distribution function

$$f_\lambda = f_0(\omega_\lambda) = \left[e^{\frac{\hbar \omega_\lambda}{k_B T}} - 1 \right]^{-1}. \tag{2.64}$$

With a temperature gradient ∇T, the change of f_λ in time t in steady-state condition can be computed from the Boltzmann transport equation [140]

$$\frac{df_\lambda}{dt} = \frac{\partial f_\lambda}{\partial t}\bigg|_{\text{diffusion}} + \frac{\partial f_\lambda}{\partial t}\bigg|_{\text{scattering}} = 0, \tag{2.65}$$

in which

$$\frac{\partial f_\lambda}{\partial t}\bigg|_{\text{diffusion}} = -\nabla T \cdot v_\lambda \frac{\partial f_\lambda}{\partial T}, \tag{2.66}$$

and

$$\frac{\partial f_\lambda}{\partial t}\bigg|_{\text{scattering}} = \nabla T \cdot \mathbf{v}_\lambda \frac{\partial f_\lambda}{\partial T}. \tag{2.67}$$

Normally, the temperature gradient ∇T is quite small. Thus the phonon distribution function f_λ can be expanded till the first order of ∇T, as

$$f_\lambda = f_0(\omega_\lambda) + g_\lambda, \tag{2.68}$$

in which

$$g_\lambda = -\tau_\lambda \mathbf{v}_\lambda \cdot \nabla T \frac{\partial f_0}{\partial T}, \tag{2.69}$$

and

$$\tau_\lambda = \tau_\lambda^0 (1 + \Delta_\lambda), \tag{2.70}$$

where τ_λ^0 is the single-mode phonon relaxation time (phonon lifetime), which can be obtained by employing the first-order perturbation theory with three-phonon scattering process taken into account. It can be written as

$$\frac{1}{\tau_\lambda^0} = \sum_{\lambda'\lambda''}^{+} \Gamma_{\lambda\lambda'\lambda''}^{+} + \frac{1}{2} \sum_{\lambda'\lambda''} \Gamma_{\lambda\lambda'\lambda''}^{-} + \sum_{\lambda'} \Gamma_{\lambda\lambda'}^{\text{ext}}, \tag{2.71}$$

in which λ, λ', and λ'' represent the phonon modes in the three-phonon scattering process, i.e., the absorption processes, labeled by $+$, and the emission process, labeled by $-$.

In the absorption process, two phonons with energies ω_λ and $\omega_{\lambda'}$ are combined to form a resultant phonon with energy $\omega_{\lambda''} = \omega_\lambda + \omega_{\lambda'}$. In the emission process, one single phonon with energy ω_λ splits into two phonons with energies of $\omega_{\lambda'}$ and $\omega_{\lambda''}$, satisfying $\omega_\lambda = \omega_{\lambda'} + \omega_{\lambda''}$.

$\Gamma^{\pm}_{\lambda\lambda'\lambda''}$ are the intrinsic scattering rates from the interaction between phonons. $\Gamma^{ext}_{\lambda\lambda'}$ are the extrinsic scattering rates due to the defects and boundaries.

The intrinsic scattering rates can be computed by

$$
\Gamma^{\pm}_{\lambda\lambda'\lambda''} = \frac{\hbar\pi}{4N} \left\{ \frac{f^0_{\lambda'} - f^0_{\lambda''}}{f^0_{\lambda'} + f^0_{\lambda''} + 1} \right\} \times \left| V^{\pm}_{\lambda\lambda'\lambda''} \right|^2
$$
$$
\times \frac{\delta\left(\omega_\lambda \pm \omega_{\lambda'} - \omega_{\lambda''}\right)}{\omega_\lambda \omega_{\lambda'} \omega_{\lambda''}},
\tag{2.72}
$$

where the elements of the scattering matrix,

$$
V^{\pm}_{\lambda\lambda'\lambda''} = \sum_{i \in u.c.} \sum_{j,j'} \sum_{xyz} \Phi^{xyz}_{ijk} \frac{e^x_\lambda(i) e^y_{p',\pm q'}(j) e^z_{p'',-q''}(k)}{\sqrt{M_i M_j M_{j'}}}
\tag{2.73}
$$

in which N is the total number of **q** points sampled in the Brillouin zone, and Φ^{xyz}_{ijk} are the third-order interatomic force constants (IFCs) computed by

$$
\Phi^{xyz}_{ijk} = \frac{\partial^3 E}{\partial r^\alpha_i \partial r^\beta_j \partial r^\gamma_k}.
\tag{2.74}
$$

i, j, and j' are the atomic indices. x, y, and z are the Cartesian directions. M_n is the mass of the nth atom. r^m_n is the displacement of the nth atom in the m direction from the equilibrium position. $e^x_\lambda(i)$ represents the eigenfunction x component of the ith atom of the phonon λ.

Δ_λ is the change of the phonon lifetime due to the absence of equilibrium condition, which can be computed by solving the BTE iteratively. It can be written as

$$
\Delta_\lambda = \sum_{\lambda'\lambda''} \Gamma^+_{\lambda\lambda'\lambda''} \left(\xi_{\lambda\lambda''} \tau_{\lambda''} - \xi_{\lambda\lambda'} \tau_{\lambda'} \right)
$$
$$
+ \sum_{\lambda'\lambda''} \frac{1}{2} \Gamma^-_{\lambda\lambda'\lambda''} \left(\xi_{\lambda\lambda''} \tau_{\lambda''} + \xi_{\lambda\lambda'} \tau_{\lambda'} \right)
\tag{2.75}
$$
$$
+ \sum_{\lambda'} \Gamma^{ext}_{\lambda\lambda'} \xi_{\lambda\lambda'} \tau_{\lambda'},
$$

in which $\xi_{\lambda\lambda'} \equiv \omega_{\lambda'} \nu^z_{\lambda'} / \omega_\lambda \nu^z_\lambda$.

The lattice thermal conductivity is computed by integrating over the first Brillouin zone, as

$$\kappa_l^{xy}\left(F_{\max}\right) = \frac{1}{k_B T^2 \Omega N} \sum_{\lambda}^{F_\lambda < F_{\max}} f_0 \left(f_0 + 1\right) \left(\hbar \omega_\lambda\right)^2 v_\lambda^x v_\lambda^y \tau_\lambda, \quad (2.76)$$

in which Ω is the volume of the unit-cell, the mean free path of the phonon mode λ $F_\lambda = |v_\lambda| \cdot \tau_\lambda$, and F_{max} is the given maximum mean free path. In the thesis, the lattice thermal conductivity is obtained by solving the phonon BTEs using ShengBTE code [141, 142]. In the calculations, the volume of unit-cell, Ω, is reduced to SH, where S is the surface area, and H is the sum of the thickness of the 2D material and the van der Waals radii of surface atoms.

2.10.2 Mechanical properties

The mechanical properties of 2D materials can be characterized by their elastic modulus tensor C, which can be computed by fitting the energy-strain curved surface [143, 144], i.e.,

$$U = \frac{1}{2} C_{11} \tau_x^2 + \frac{1}{2} C_{22} \tau_y^2 + C_{12} \tau_x \tau_y + 2 C_{66} \tau_{xy}^2, \quad (2.77)$$

in which the τ_x, τ_y, τ_{xy} are the strain along the x-, y-, and xy-directions (shear strain). C_{11}, C_{22}, C_{12}, and C_{66} are the components of the elastic modulus tensor.

With the elastic modulus tensor, we can compute the in-plane Young's moduli E_{2D} and Poisson's ratios ϑ in the different directions θ. By using the formulae [145, 146]

$$E_{2D}(\theta) = \frac{C_{11} C_{22} - C_{12}^2}{C_{11} \sin^4 \theta + C_{22} \cos^4 \theta + \left(\frac{C_{11} C_{22} - C_{12}^2}{C_{66}} - 2 C_{12}\right) \cos^2 \theta \sin^2 \theta}, \quad (2.78)$$

and

$$\vartheta(\theta) = -\frac{\left(C_{11} + C_{22} - \frac{C_{11} C_{22} - C_{12}^2}{C_{66}}\right) \cos^2 \theta \sin^2 \theta - C_{12} \left(\cos^4 \theta + \sin^4 \theta\right)}{C_{11} \sin^4 \theta + C_{22} \cos^4 \theta + \left(\frac{C_{11} C_{22} - C_{12}^2}{C_{66}} - 2 C_{12}\right) \cos^2 \theta \sin^2 \theta}. \quad (2.79)$$

It is notable that Young's modulus obtained from the above method cannot be directly compared with 3D structures since they do not have the same unit. For comparison, the 3D Young's modulus can be computed by $E = E_{2D}/H$, in which H the sum of the thickness of the 2D material and the van der Waals radii of surface atoms.

2.10.3 Carrier mobility

For 2D semiconductors, the carrier mobilities can be computed with the deformation potential method [147]. The carrier mobility is approximately

$$\mu = \frac{e\hbar^3 C_{2D}}{k_B \, T \, m^* m_d^* \left(E_d^i\right)^2},\tag{2.80}$$

where k_B is the Boltzmann constant, e is the charge of an electron, $\hbar$ is the reduced Plank constant, and T represents the temperature. C_{2D} is the 2D elastic which can be computed using Equation 2.77, or by the equation $(E - E_0)/S_0 = C_{2D} \left(\Delta l/l_0\right)^2 /2$, in which $E - E_0$ is the energy change of the 2D structure under strain. S_0 is the surface area of the pristine 2D structure. l/l_0 is the lattice constant deformation ratio in the transport direction. m_d^* is computed by $m_d^* = \sqrt{m^* m_\perp^*}$, illustrating the mean effective mass, in which m^* is the effective mass of the hole or electron in the transport direction, and $m_\perp^*$ is the effective mass in the perpendicular direction. E_d^i represents the deformation potential constant of band i, which is computed by $E_d^i = \Delta V^i / (\Delta l/l_0)$. In the formula, ΔV^i is the change of the edge of band i under the strain of Δl.

Part II:
Summary of the Results

3. Functionalization of two-dimensional materials

In order to be applied in a specific field, two-dimensional materials need to have many different properties at the same time, while it is not easy to find materials satisfying all the requirements. A general way is to find a material satisfying most of the requirements and functionalize it by using some method such as by using chemical adsorption, oxidization, substrate, defect, and strain.

3.1 Adsorption of 3d transition metal clusters on defected graphene

Graphene, as the first realized 2D material, has dramatically attracted the research interests from both theory and experiments. There are quite many unique properties such as high mobility, quantum Hall effect, Dirac cones, high Young's modulus, and excellent stability [6, 8]. However, the absence of many vital properties has hindered its applications in many basic nanodevices. As one of the most significant exemplar, without magnetism, pristine graphene have many obstacles in working in spintronic fields. To remove the limitations, many functionalization methods have been studied, such as depositing it on substrates, cutting it along different edges, inserting defects, and adsorbing molecules or atoms [13, 12, 14, 15, 16, 17].

Chemically doping is a widely used method to manipulate the properties of 2D materials. For introducing magnetism, adsorbing transition metal atoms or clusters is a standard way. However, on pristine graphene, without dangling bonds, the transition metal atoms usually have high mobilities [148, 149, 150]. A recent work by Krasheninnikov et al. [151] and Gan et al. [152] have reported that the transition metal atoms can be arrested by the defects on graphene. Moreover, by continuing adsorbing more atoms, small clusters appear. The studies of the magnetic proprieties of these transition metal clusters functionalized graphene may help for graphene applications in spintronic devices.

3.1.1 Self-assembly process

The self-assembly processes are studied by BOMD simulations at a constant temperature of $T = 300K$. The initial substrate structures are built by taking one or two carbon atoms away from a large supercell of graphene. Then
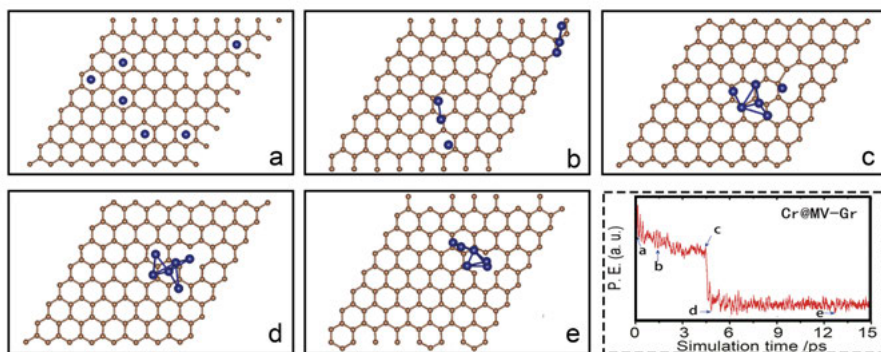
Figure 3.1. Self-assembly process of Cr hexamer formation on graphene with a MV defect. The corresponding times and potential energies (P.E.) in Figure a-e are also shown in the figure at the lower right corner. Reproduced with permission from Paper I. Copyright ©2019 American Chemical Society.

six sites on graphene are randomly picked to put the isolated transition metal atoms, as shown in Fig. 3.1(a).

In the simulations for all the X@MV/DV-Gr systems up to 15 ps, several exciting observations are found. Firstly, the relaxation of the defect area of graphene is very fast (takes less than 1.5 ps). For graphene substrates with a MV defect, the defect area reconstructs into a 5-9 defect, while for graphene with a DV defect, the defect area forms a 5-8-5 defect. In the process, the adatoms are not bonded firmly with pristine graphene. Moreover, they can, therefore, move very fast on the smooth surface. Once the atoms or clusters get caught by the defects, they cannot run away. The BOMD images, along with potential energies (P.E.) of Cr@MV-Gr, are given as an example. Other X@MV/DV-Gr systems have a similar phenomenon, as shown in the supplementary information of Paper I.

Among Cr, Mn, and Fe atoms, the Fe atoms move the slowest on the pristine part of the graphene substrate, which implies that the interaction between Fe atoms and pristine graphene is much stronger than Cr and Mn atoms. This is confirmed by DFT calculations, in which we compared the adsorption energies of the three types of atoms on pristine graphene. The adsorption energies of Cr atom and Mn atom are -0.27 eV/Cr atom and -0.20 eV/Mn atom, respectively, which are much smaller than that of Fe, -1.24 eV/Fe atom. The later calculation also implies that isolated Fe atoms may be fixed on graphene.

In summary, the BOMD simulations show that the three transition metal atoms on defected graphene prefer to accumulate at defect sites, resulting in firmly bonded cluster-graphene systems.
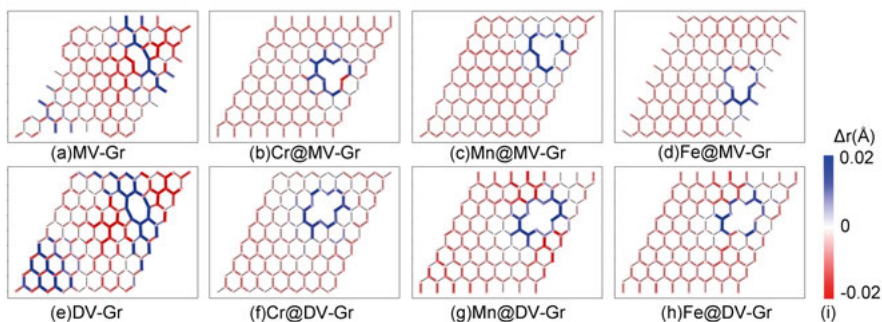
Figure 3.2. The C-C bond length in graphene with mono/divacancies and clusters. The bond length r is compared with that in pristine graphene r_0, by the value of $\Delta r = r - r_0$. Reproduced with permission from Paper I. Copyright ©2019 American Chemical Society.

3.1.2 Ground and metastable states of X@MV/DV-Gr

To study the properties of the final structures in BOMD simulations, their ground states are needed. These structures are optimized with setting different initial magnetic configurations, and the energies are compared to determine the ground states. The structures and magnetic configurations of the ground states are discussed in two parts: the substrate and the adsorbate.

The graphene parts of the ground states are present in Fig. 3.2(b)-(d) and (f)-(h). Since most substrate parts are not changing significantly, the bonds with different C-C bond lengths are emphasized using different colors. In the figures, the colors are determined by $\Delta r_{i,j} = r_{i,j} - r_0$, in which $r_{i,j}$ demonstrates the bond length between two adjacent carbon atoms i and j in defected graphene, and r_0 demonstrates that in pristine graphene. $\Delta r_{i,j}$ also indicates the measure of tensile and compressive strains in the substrates.

As shown in Fig. 3.2(a) and (e) in pristine defected graphene, five-atom rings induces strong tensile strain in the longest-bond direction. While in X@DV/MV systems, with Cr, Mn, and Fe atoms trapped at vacancy sites, no five-atom ring is formed. Therefore the strain is much more localized in X@MV/DV-Gr systems.

The atomic magnetic moments of carbon atoms in all X@MV/DV-Gr systems are never larger than $1\mu_B$, and the distribution is shown in Fig. 3.3. In all X@MV/DV-Gr systems, without unpaired electrons, all the carbon atoms show very small magnetic moments. What is more, the tiny moments decline rapidly as the distance increases from defect centers and converge to almost zero at 8 Å.

Geometries and magnetic configurations of the adsorbate part are shown in Fig. 3.4(a)-(f). Only the defect areas are plotted, with the transition metal atoms labeled with numbers. Each transition metal atom is denoted as XN
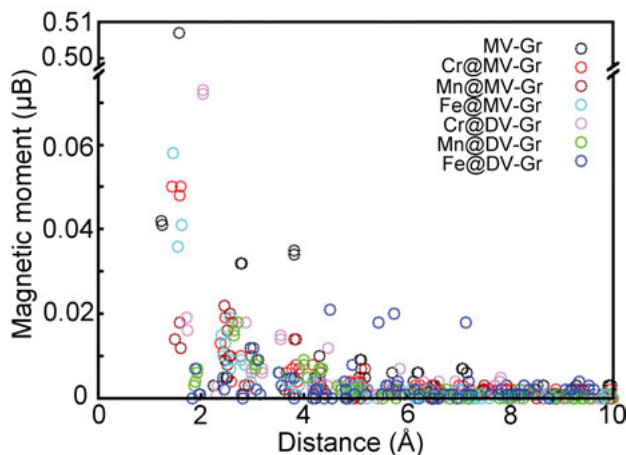
Figure 3.3. The magnetic moments of the carbon atoms in different distances from the defect sites. Reproduced with permission from Paper I. Copyright ©2019 American Chemical Society.

(X=Cr, Mn, Fe, and N=1-6). In the figures, the yellow and blue isosurfaces show up- and down-spin densities.

As shown in Fig. 3.4, all the hexamers are bonded with a graphene substrate with one trapped atom and show a pendulum-like structure. Interestingly, the ground state of Cr hexamers all have two short bonds (about 1.7 Å), which substantially decreased the total energy of Cr hexamers. The short bonds are also found in many Chromium compounds, like [PhCrCrPh], as the result of the $3d^5 4s^1$ half-filled electronic configurations.[153, 154, 155, 156, 157]

The magnetic structures are shown in Fig. 3.4 as spin densities and in Table 3.1 as the atomic magnetic moments. All Fe hexamers are ferromagnetic [158] while Cr and Mn hexamers show ferrimagnetic structures, which agree with the recent experimental result in Ref. [159]. In detail, the Mn or Fe atoms trapped at the defect sites own the tiniest magnetic moments, while the Cr atoms as the endpoints of the short bond own the tiniest magnetic moments. In general, the least bonded transition metal atoms have the largest magnetic moments.

By setting various initial magnetic moments, many metastable structures are found, among which the one who has the lowest energy is named as the first metastable structure. The energy difference of the ground state and the first metastable state can be used for measuring the stability of ground states. As shown in Table 3.2, the formation energy is defined as:

$$E_{form} = E_{X@Gr} - (E_{X_6} + E_{Gr}). \tag{3.1}$$

It is observed that most ground states have significant energy differences with their corresponding first metastable structures. However, the energy difference between the ground and the first metastable state of Cr@MV-Gr is quite small

44
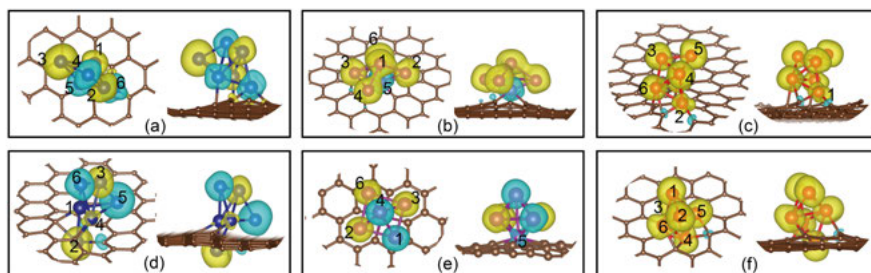
Figure 3.4. The spin density distribution of the transition metal clusters on graphene with monovacancy (a, b, c) and divacancy (d, e, f). Isosurface level is set as 0.008. Cr, Mn, and Fe atoms are in blue, brown, and red, respectively. Reproduced with permission from Paper I. Copyright ©2019 American Chemical Society.

Table 3.1. *The magnetic moment of each transition metal atom in the ground states (in μ_B). Reproduced with permission from Paper I. Copyright ©2019 American Chemical Society.*

Graphene	Monovacancy			Divacancy		
Mag$_s$ \\ Cluster atom	Cr$_6$	Mn$_6$	Fe$_6$	Cr$_6$	Mn$_6$	Fe$_6$
1	1.35	3.58	2.57	0.03	-3.59	2.89
2	1.48	3.83	0.82	2.84	3.49	2.91
3	4.06	3.48	2.94	1.81	3.47	2.62
4	-1.41	3.61	2.85	0.15	-3.88	2.14
5	-1.27	-1.87	2.98	-3.85	-0.51	2.80
6	-1.40	3.58	2.79	-2.03	3.25	2.51

(less than 1 meV). The geometries and magnetic structures are shown in Fig. 3.5(a), the position of Cr4 has changed a lot, and the magnetic configuration has changed from (+++—) to (++—-).

Table 3.2. *The computed cohesive energies of the ground states and the first metastable structures. Reproduced with permission from Paper I. Copyright ©2019 American Chemical Society.*

Graphene	Monovacancy			Divacancy		
Cluster	Cr_6	Mn_6	Fe_6	Cr_6	Mn_6	Fe_6
E_{gro}	-6.61	-6.17	-2.55	-6.57	-7.18	-1.90
E_{meta}	-6.61	-5.45	-2.17	-6.30	-6.55	-1.43
Δ	0.00	0.72	0.37	0.28	0.63	0.47
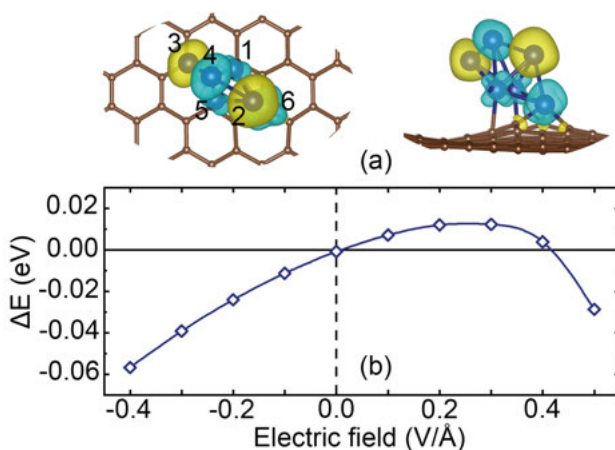
Figure 3.5. (a) The first metastable state of Cr@MV-Gr. (b) The energy difference between the ground state and the first metastable state in different external electric fields. $\Delta E = E_{ground} - E_{metastable}$. Copyright ©2019 American Chemical Society.

With external electric field, the ground states and the first metastable state can be tuned greatly. As shown in Fig. 3.5(b), they have equal energy at about E= 0 V/Å or E = 0.4 V/Å. Interestingly, from E = 0 V/Å to E = 0.4 V/Å, the structure in Fig. 3.5(a) shows lower energy instead.

3.1.3 Electric field manipulation of magnetic anisotropy

The magnetic anisotropy energies (MAEs) of these structures (ground states) are measured, as shown in Table 3.3. Cr@DV-Gr and Fe@DV-Gr own tiny energy difference between the out-of-plane and the in-plane axes, which is implying a possibility of switching the magnetic axes by the electric field.

46

Table 3.3. *Orbital (μ_{orb}), spin (μ_{sp}), total ($\mu_{tot}=\mu_{orb}+\mu_{sp}$), and average ($\mu_{tot}/6$) magnetic moments of the transition metal hexamers on defected graphene (in μ_B). Reproduced with permission from Paper I. Copyright ©2019 American Chemical Society.*

Graphene	Monovacancy			Divacancy		
Cluster	Cr_6	Mn_6	Fe_6	Cr_6	Mn_6	Fe_6
μ_{orb}	0.01	0.06	0.35	0.02	0.03	0.38
μ_{sp}	3.60	18.27	15.68	1.79	2.26	16.65
μ_{orb}/μ_{sp}	0.003	0.003	0.022	0.011	0.013	0.023
μ_{tot}	3.61	18.33	16.03	1.81	2.29	17.03
μ_{ave}	0.60	3.05	2.67	0.30	0.38	2.84

By applying the electric field, the magnetic anisotropy energies of Cr@DV-Gr and Fe@DV-Gr are tuned continuously, as shown in Fig. 3.6. The easy magnetic axis of Fe@DV-Gr is switched from in-plane to out-of-plane in an electric field of 0.1 V/Å, and the easy magnetic axis of Cr@DV-Gr is switched from the z-direction to the x-direction with an electric field stronger than 1.0 V/Å.
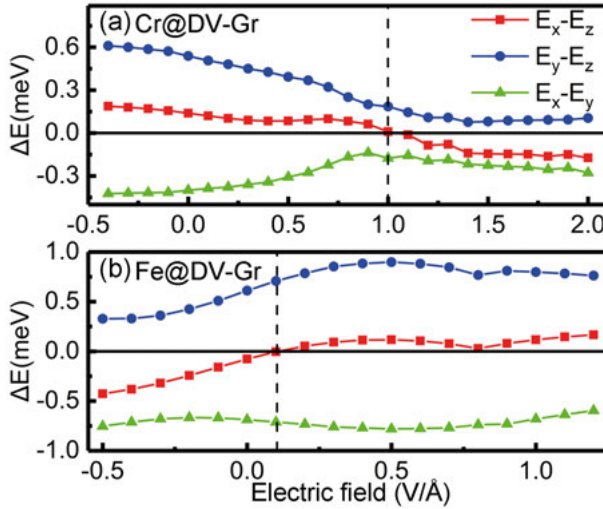
Figure 3.6. (a) Energy difference between magnetic directions of Fe@DV-Gr as a function of the electric field. (b) Energy difference between magnetic directions of Cr@DV-Gr as a function of the electric field. Reproduced with permission from Paper I. Copyright ©2019 American Chemical Society.

To investigate the mechanism of the electric field shifted MAE, the effect of an electric field on the projected density of states (PDOS) is important since the PDOS change is related to MAE through the second-order perturbation

method:[160]

$$E_x - E_z = \xi^2 \sum_{u,\alpha,o,\beta} (2\delta_{\alpha\beta} - 1)[\frac{|\langle u,\alpha| L_z |o,\beta\rangle|^2}{\epsilon_{u,\alpha} - \epsilon_{o,\beta}} - \frac{|\langle u,\alpha| L_x |o,\beta\rangle|^2}{\epsilon_{u,\alpha} - \epsilon_{o,\beta}}]$$

(3.2)

According to Equation 3.2, d_{z^2} and (b) d_{yz} projected DOS of the trapped atoms affects MAE the most, and their changes in the electric field are shown in Fig. 3.7. The change is coming from the charge transfer between graphene substrate and hexamers in the electric field. Detailed discussions are presented in Paper I.
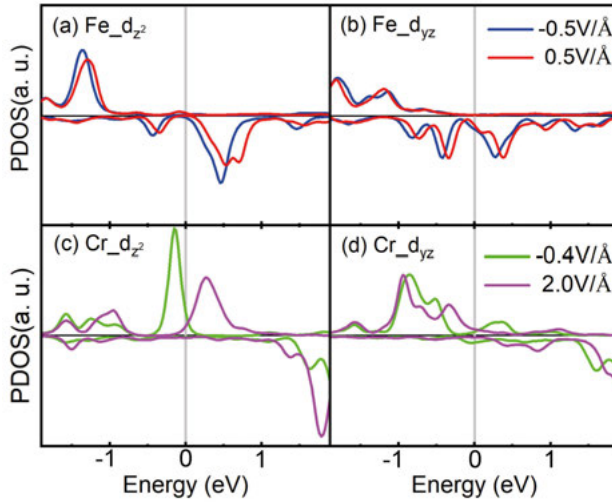
Figure 3.7. (a) d_{z^2} and (b) d_{yz} projected DOS of the Fe atom and the Cr atom trapped in graphene, in presence of an external electric field. Reproduced with permission from Paper I. Copyright ©2019 American Chemical Society.

3.2 2D dumbbell-like silicene structures and their functionalization

Different from graphene, free-standing silicene is low-buckled (LB) single layer due to pseudo Jahn-Teller effect.[30] and can easily chemisorb atoms or clusters.[31, 32, 33, 34, 35, 36, 37, 38, 39, 40] The adsorption of Si atoms on silicene is studied [41, 42] and dumbbell-like (DB) units are found to be energetically preferred. Recently based on DB units, a series of DB structures are predicted and investigated. It is found that the several most stable DB structures own much lower energy than L.B. silicene due to fewer dangling bonds.[161] The DB silicenes still have dangling bonds which can easily chemisorb atoms or clusters. In this chapter, I briefly discussed the structure

and stability of the oxide forms of two stable DB silicene and then investigated their electronic properties. It is found that both of the oxidized DB silicene structures are semi-metal, and the Dirac cones own high Fermi velocities. More details can be read in Paper II.

3.2.1 DB-h silicene and DB-z silicene

The single-layer silicene with DB units is predicted to be more stable than pristine L.B. silicene in freestanding condition. Recently, a theoretical study has predicted and compared the energies of all the DB silicene structures and have come up with several stable structures[161].
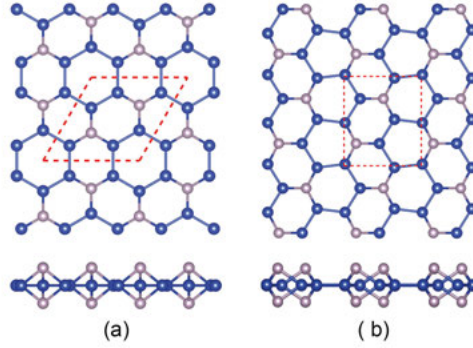
Figure 3.8. The top and side views of optimized structures of PDB-h and PDB-z are shown in (a), (b), respectively. The blue, grey balls demonstrate Si(α), Si(β) atoms, the dashed area is the primitive cell of PDB-h and PDB-z. Reproduced from Paper II.

The pristine dumbbell silicene structures (labeled as PDB) with dumbbell units arranged in honeycomb pattern (labeled as PDB-h)[162] and in zigzag pattern (labeled as PDB-z)[161] are shown in Fig. 3.8. For both DB-h and DB-z silicene, there are two DB units containing 10 silicon atoms in one unit cell. The thickness of the layer and the atomic density are both almost the same.

The electronic band structures of PDB-h and PDB-z are shown in Fig. 3.9. PDB-h and PDB-z are both indirect-gap semiconductors, with a band gap of 0.24 eV and 0.62 eV, respectively. The conduction band minimum (CBM) of both cases are at Γ point, while the valence band maximum (VBM) of PDB-h is at K point, and that of PDB-z is near S point. These results are in good agreement with the recent study.[162, 42, 161]
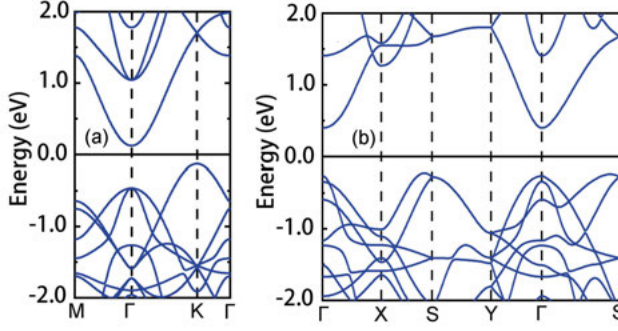
Figure 3.9. PBE band structures of (a) PDB-h, and (b) PDB-z. The energy is set to zero at the Fermi level. Reproduced from Paper II.

3.2.2 Oxidized dumbbell silicene

The oxidization problem is essential in the application of silicon-based materials[39]. In contrast to the hydrogenation forms of DB silicene, the study of oxidization is still absent.

In this section, the oxidized forms of DB silicenes (labeled as ODB-h and ODB-z) are investigated, and its stability is further proved from the energetic aspect and dynamics aspect. Moreover, the electronic properties of these structures are calculated and analyzed. It is found that both ODB-h and ODB-z are semi-metal with high Fermi velocity. The robustness of the Dirac cones against tensile strain is also discussed.

Geometry structure and stability

As shown in Fig. 3.10, in both ODB-h and ODB-z, all the three-fold silicon atoms are fully coordinated with O atoms. The thickness of the DB units is increased to about 2.8 Å, due to stronger sp^3 hybridization. In both cases, the Si-O bond length is roughly the same, similar to that in β-cristobalite[163].

The binding natures of ODB-h, ODB-z, PDB-h, and PDB-z are analyzed using electron localization functions (ELF). As shown in Fig. 3.11, the ELF plots of ODB-h and ODB-z are almost the same, implying a similar bonding mechanism. Comparing PDB and ODB, the electrons in ODB silicene Si atom layers are not as localized as that in PDB silicene. Furthermore, the binding energies of O atoms on PDB-h and PDB-z are about -5.2 eV/O atom, implying strong chemisorption.

The formation energy is calculated in the reaction $Si + O_2 \rightarrow Si_{10}O_4$, in which Si denotes bulk silicon, while O_2 denotes oxygen gas, and $Si_{10}O_4$ denotes ODB-h and ODB-z. The formation energy of ODB-h is about $-0.363eV$ per O atom, slightly smaller than that of ODB-z, $-0.366eV$ per O atom. Both reactions are exothermic.
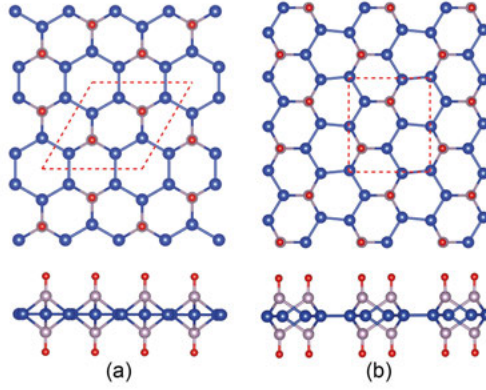
Figure 3.10. The optimized structures of ODB-h and ODB-z are shown in (a), (b), respectively. The blue, grey, and red balls demonstrate Si(α), Si(β), and oxygen atoms. Reproduced from Paper II.

The phonon dispersion spectrum along high symmetric points is calculated and shown in Fig. 3.11(c) and (d). Since no mode with imaginary frequencies is found, the dynamical stability of ODB-h and ODB-z is confirmed.
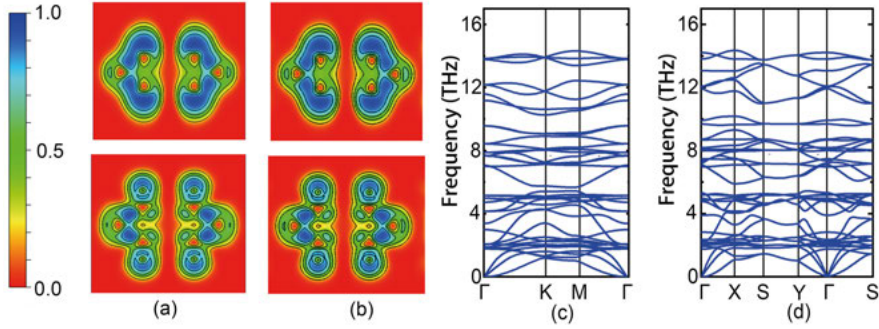
Figure 3.11. The top panel is the slice view of the ELF of PDB-h and ODB-h (a), PDB-z and ODB-z (b). The bottom panel is the phonon dispersion spectrum of ODB-h (c) and ODB-z (d), respectively. Reproduced from Paper II.

Electronic structure

From the local density of states distribution (LDOS) of ODB-z and ODB-h in Fig. 3.12, it is found that the $p_{x,y}$ orbitals of O atoms, $p_{x,y}$ and p_z atomic orbitals of Si(α) in ODB-h and ODB-z have the most contribution to the states near the Fermi level.

The band structures are shown in Fig. 3.13 along with the contribution of $p_{x,y}$ orbitals of O atoms, $p_{x,y}$ and p_z atomic orbitals of Si(α) in ODB-h and
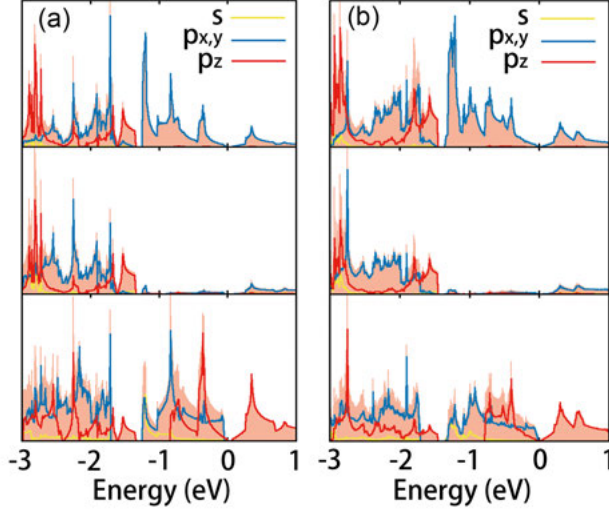
Figure 3.12. From bottom to top panel is the LDOS projected on Si(α), Si(β) and O layers of (a) ODB-h and (b) ODB-z. PDOS of s, $p_{x,y}$ and p_z orbitals and total DOS of corresponding layers are distinguished with yellow, blue, and green lines and orange area, respectively. Reproduced from Paper II.

ODB-z. It is observed that both ODB-h and ODB-z have Dirac cones at the Fermi level. By linearly fitting the band structure, following:

$$\nu = \frac{1}{\hbar}\nabla_k E(\mathbf{k}), \tag{3.3}$$

$$m^* = \hbar\frac{d^2 E(\mathbf{k})}{d\mathbf{k}^2}, \tag{3.4}$$

in which $E(\mathbf{k})$ is the band gap at wave vector $\mathbf{k}$. velocity ν of ODB-h and ODB-z is calculated, as 3.1×10^5 m/s and 3.4×10^5 m/s respectively, comparable to that of graphene, silicene, and stanene ($4.7 - 8.5 \times 10^5$ m/s), with effective mass m^* equal to zero at the Fermi level.

The Dirac cones as shown in Fig. 3.13, are mainly contributed by $p_{x,y}$ atomic orbitals of O atoms and p_z orbitals of Si(α) atoms, and the $p_{x,y}$ atomic orbitals of O atoms contribute much more than p_z orbitals of Si(α) atoms, as shown in Fig. 3.13 (c) and (d).

To study the origin of the Dirac cones in ODB-h and ODB-z explicitly, tight-binding models involving only the p_x and p_y atomic orbitals are proposed. The Hamiltonian is taken as[164]:

$$H_{TB} = \sum_{i,\alpha}\varepsilon_i^\alpha c_i^{\alpha+}c_i^\alpha + \sum_{\langle i,j\rangle,\alpha,\beta} t_{ij}^{\alpha\beta}(c_i^{\alpha+}c_j^\beta + h.c.), \tag{3.5}$$
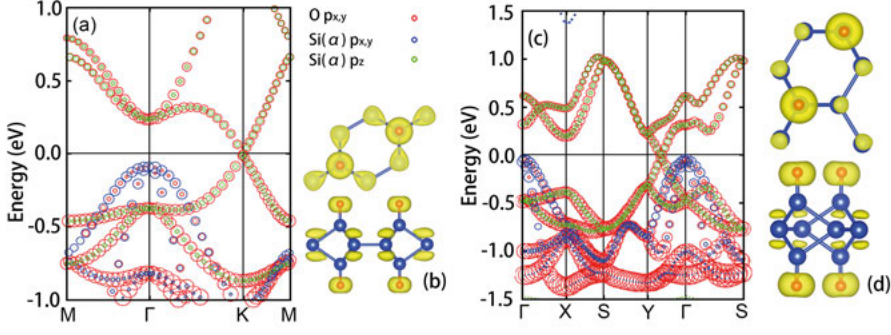
Figure 3.13. The orbital projected band structures of ODB-h and ODB-z along high symmetry path are shown in (a) and (b); the corresponding electron wave functions of VMB/CBM are shown in (c) and (d). Reproduced from Paper II.

in which ε_i^α, $c_i^{\alpha+}$, and c_i^α denotes the on-site energy, creation and annihilation operators of an electron at the α-orbital of the i-th atom, respectively. $t_{ij}^{\alpha\beta}$ is the nearest-neighbor hopping energy of i-th atom's α-orbital and j-th atom's β-orbital. This model nicely fitted the Dirac points at the Fermi level, and the details are presented in Paper II.

Strain manipulated electronic properties

Applying in-plane strain on 2D materials is a feasible route to manipulate the electronic properties. [66, 165, 162] In this contribution, strain is applied by changing the lattice parameter from a_0 to $(1 + \tau)a_0$. As shown in Fig. 3.14(a) and (b), the energy changes continuously, implying no structural transition.
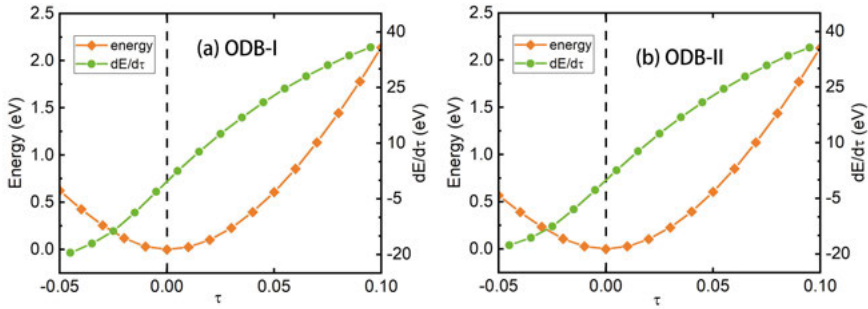

Figure 3.14. Energy and energy derivative with different in-plane tensile strain τ. The energy is set to zero at $\tau = 0$. Reproduced from Paper II.

The Dirac cones near the Fermi level in ODB silicenes are always intact under strain. Under tensile stress, the Dirac cones are at the Fermi level until $\tau = 9\%$, while under strong compressive strain, the Dirac cones are shifted

below Fermi level, implying that the electrons from Si(β) are taken by Si(α) and O atoms.

I have also performed band structure calculations with the SOC effect considered. The SOC effect is not strong since both Si and O are light elements. Therefore, with or without SOC, the band structures are not significantly changed. At the Dirac cones in both ODB-h and ODB-z, a band gap of roughly 10 meV is opened. The SOC band gap is much larger than that of L.B. silicene. It is because that the Dirac cones in ODB-h and ODB-z are mainly contributed by the p_x and p_y atomic orbitals of O atoms, while in L.B. silicene, the Dirac cone is mainly contributed by the p_z atomic orbital of Si atoms, and the SOC effect of p_x and p_y in 2D materials are more significant than p_z atomic orbitals.

Finally, a hybrid functional calculation using HSE06 is performed to correct the PBE band gap. Without SOC, there is no band gap opened at the Fermi level, and the Dirac cones are intact. With SOC, the band gap is enlarged to roughly 20 meV in both ODB-h and ODB-z.

4. New 2D materials with novel properties

Beyond investigating the functionalization of 2D materials, the investigation of new 2D materials is another important way to satisfy the requirement of different applications. Many efforts have been paid to this topic, both in the experiment and theory.

The crystal structural information is virtual importance in first-principles based studies. However, limited by the experimental techniques [75, 76], it is quite hard to get the atomic coordinates in a unit cell. For example, Watson, Crick, and Wilkins got the Nobel Prize in 1962 for their prediction of the structure of deoxyribonucleic acid (DNA). Many research interests have been conducted to predict the possible structures. Many methods have been established [77, 78, 79, 80, 81, 82, 83, 84, 85, 86]. The evolutionary algorithm is one of the most efficient method in this field. In this part, based on the evolutionary structure search, we predicted several new 2D materials with distinct properties and interesting potential applications.

4.1 Highly tunable anisotropic Dirac cones in PAI-graphene

Carbon is a special main group element. It has many different hybridization forms. Based on that, carbon atoms can fabricate enormous allotropes, such as diamond, graphite, graphene, graphyne, carbon nanotube, C60 [43, 44, 45, 46]. Among them, graphyne, as a class of newly synthesized 2D materials, has attracted much research interest. But indeed, there are many sp^2, and sp^3 hybridization dominated graphene allotropes constructed with non-hexagonal rings are lower in energy than graphyne, such as T-graphene[49], Haeckelite sheets[166, 167], and SW-graphene[55]. These 2D materials have quite different properties from graphene, such as NPR[50, 168], anisotropic Dirac cones [49, 53, 55], and high Li storage capacity[54]. Moreover, due to the low energies, they are likely to be realized in the future experiment.

4.1.1 Structure and stability

Based on density functional theory calculations and evolutionary structure search, we generated thousands of 2D carbon allotropes and compared their energies. The energies of these structures are shown in Fig. 4.1. Firstly, it is observed

that graphene is the most stable structure in our calculation. Beyond graphene, a structure, namely PAI-graphene with 24 atoms per primitive cell, has the lowest energy, of only 144 meV/atom higher than graphene[53].
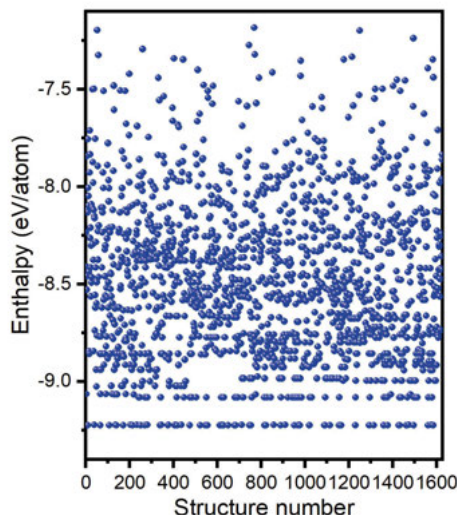
Figure 4.1. The energies of the structures discovered in our structure search. Reproduced with permission from Paper IV. Copyright ©2020 Elsevier.

As shown in Fig. 4.2, the optimized structure of the carbon allotrope is constructed of 5-6-7 carbon rings. It can be divided into many carbon skeletons of as-indacene, as indicated by the green blocks in Fig. 4.2. PAI-graphene has 24 atoms in one unit cell, showing Pbam (layer group No. 44) group symmetry. The C-C bonds are different from graphene, and they vary from 1.392 Åto 1.468 Å.

The dynamic stability of PAI-graphene is proved from two aspects. One is the phonon spectrum at 0 K: there are no imaginary modes, showing that it is dynamically stable. The other aspect is the energy changes of the structure at high temperature: we have performed ab initio molecular dynamics simulations at 1500 K, showing that PAI-graphene is still stable at this temperature, without any structural reconstruction.

For further application, an easy-achieved synthesis route is very important. In the work, we have proposed a route for synthesizing the carbon allotrope: by polymerizing as-indacenes, i.e., $2C_{12}H_8 \rightarrow C_{24}$(PAI-graphene)$+8H_2$. In this reaction, energy of 71 meV/carbon atom is released.
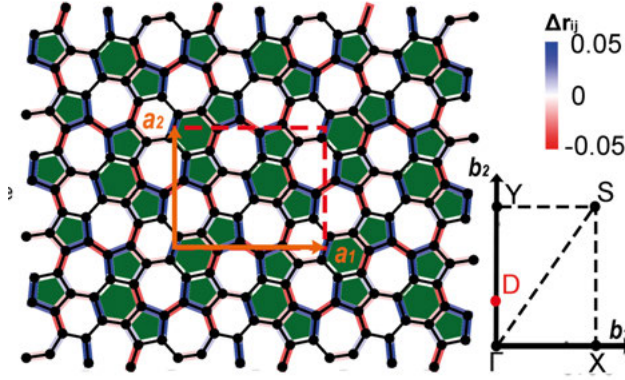
Figure 4.2. The optimized structure of PAI-graphene, with the unit cell illustrated by red dashed lines. The lattice vectors are marked by orange vectors. Green blocks are the units of the carbon skeleton. The lengths of the carbon bonds are illustrated with different colors, and the relative values are given in the color bar, where $\Delta r_{ij} = r_{ij} - r_{graphene}$, in which $r_{graphene}$ is the bond length in graphene. Part of the first BZ is also shown. Reproduced with permission from Paper IV. Copyright ©2020 Elsevier.

4.1.2 Electronic properties

We computed the electronic band structures and the density of states (DOS) distribution, as shown in Figs. 4.3. From the HSE06 results in Figs. 4.3 (a) and (b), it is observed that the VBM and CBM meet at one point at the Fermi level, forming a distorted Dirac cone. Two Dirac cones are observed in the first BZ, one is between Y and Γ, and the other one is between Y′ and Γ, as shown in Fig. 4.3 (c). By linear fitting the band structure, we got the Fermi velocities are up to 7.0×10^5 m/s, comparable to that of graphene, i.e., 1.01×10^6 m/s (HSE) [59].

The origin of the Dirac cones is investigated by computing the atomic orbital projected bands, as shown in Fig. 4.3 (d). It is observed that the two bands are contributed by the p_z atomic orbitals of two groups of carbon atoms. The inversion feature is similar to that in many other 2D materials with distorted Dirac cones [53, 55].

Moreover, a tight-binding (TB) model is proposed for describing the bands near the Fermi level. The effective Hamiltonian is written as:

$$H_{TB} = \sum_{\langle i,j \rangle} t_{ij} c_i^+ c_j + h.c., \tag{4.1}$$

in which c_i^+ is the creation operator of a p_z electron of the ith atom. t_{ij} is the hopping parameter between the electrons of the ith atom and j^{th} atom. Only the first nearest neighbor is considered, and t_{ij} is distance-dependent, written as $t_{ij} = t_0 exp(q \times (1 - d_{ij}/d_0))$, where $t_0 = -2.7$ eV, adjustment factor
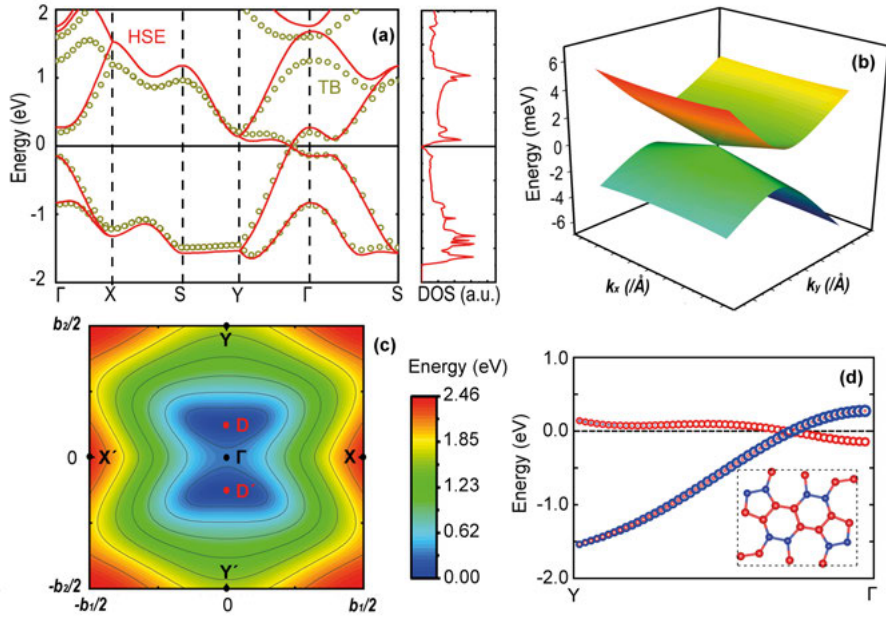
Figure 4.3. (a) The band structures and total DOS by HSE06 (in red), and the band structures by TB model (in brown-green). (b) The highest valence band and the lowest conduction band near the Dirac cone. (c) The contour plot the band gap in the first BZ. (d) The fat bands near the Dirac cone. The contributions of different atoms are plotted in correspondingly colored circles. Reproduced with permission from Paper IV. Copyright ©2020 Elsevier.

$q = 2.8$, and $d_0 = 1.5$ Å. Hoping energies less than 0.1 eV is ignored. As show in Fig. 4.3(a), the TB model fits the DFT result well.

4.1.3 Strain-induced electronic phase transition

Then we studied the strain-induced electronic band structure changes systematically. The strain in simulated by tuning the lattice parameters from ($\mathbf{a}_1$, $\mathbf{a}_2$) to (($1+\tau_x$)$\mathbf{a}_1$, ($1+\tau_y$)$\mathbf{a}_2$). As shown in Fig. 4.4, with strain in the range $-2\% \leq \tau_x, \tau_y \leq 10\%$, the potential energy (P.E.) changes continuously, implying no structural phase transition. By applying different tensile strains, PAI-graphene has three different electronic states, as shown in 4.4 (b): (1) semi-metallic state with two Dirac points on the high symmetry path $Y - \Gamma$ and $Y' - \Gamma$ (purple points); (2) semi-metallic state with two Dirac points on $X - \Gamma$ and $X' - \Gamma$; (3) semiconducting state. The mechanism of this property is discussed in detail in Paper IV.
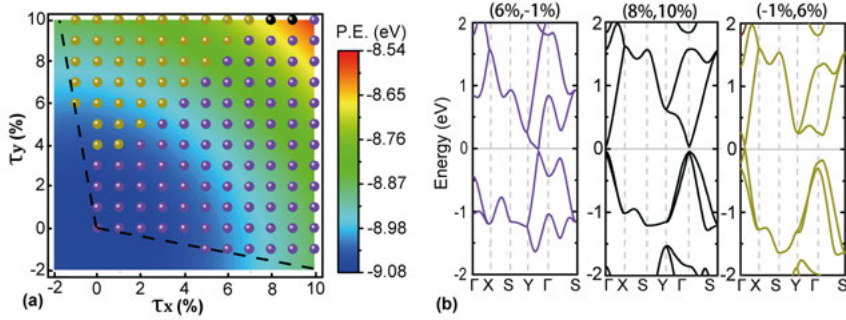
Figure 4.4. (a) The contour plot of the potential energy (P.E.) under different strain. The electronic feature of the strained structures are indicated by different colors. And corresponding examples are shown in (b), including with Dirac cones along Y-Γ, along X-Γ, and without Dirac cone. Reproduced with permission from Paper IV. Copyright ©2020 Elsevier.

The change in the Dirac points' position is then studied systematically by employing different uniaxial strains in the y-direction. The position change and total energy change are shown in Fig. 4.5 (a). The tracked Dirac cone moves from 0.35Y to Γ and then moves to 0.18X under strain from 0 to $\tau_y = 7\%$. The energy changes continuously, showing that the electronic property change is not induced by a structural phase transition. Importantly, near $\tau_y = 2.8\%$, the positions of the Dirac cones change steeply, as shown in Fig. 4.5 (b). This is an excellent property for applications as sensors.
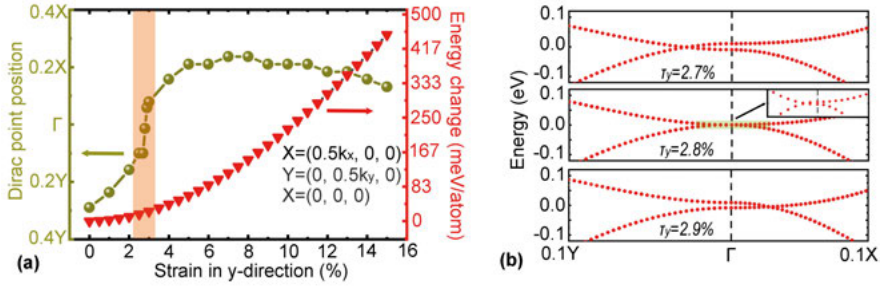
Figure 4.5. (a) The position of the Dirac cones (green) and the total energy of the system (red) as a function of uniaxial strain in the y-direction. (b) The electronic bands with Dirac cones near the Γ point. Reproduced with permission from Paper IV. Copyright ©2020 Elsevier.

## 4.2 Two-dimensional square-A_2B (A=Cu, Ag, Au; B=S, Se)

The 2D form of A_2B (A=Cu, Ag, Au; B=S, Se) has become attractive to the scientific community in recent times. For instance, 2D β-Cu_2S sheet with a hexagonal structure [169, 170] has been synthesized recently. Furthermore, theoretical work by Guo et al. [171] predicts that 2D β-Cu_2S is not the lowest energy structure of 2D Cu_2S, i.e., a new 2D structure δ-Cu_2S with superior oxidation resistance has lower energy than β-Cu_2S. Peng et al. have predicted monolayer α-Ag_2S, and further experiment work synthesized it [117, 172]. 2D colloidal Cu_2Se has been synthesized using the Langmuir-Blodgett method [173]. However, a systematic structural prediction for the 2D form of A_2B is absent.

Negative Poisson's ratio (NPR) is an unusual property in some materials: with tensile strain in one direction, it expands in the perpendicular direction. The materials with this property are named NPR materials or auxetic materials. NPR has been realized in many 3D materials and used in many areas such as medicine, clothing, and tough composites [113, 114, 115]. However, in 2D materials, NPR is still a rare property [144].

4.2.1 Structure search and stability

In our structure search, we predicted thousands of structures and compared their energies, as shown in Fig. 4.6 (a). The structures with their thicknesses less than 3 Å have similar square geometries, s(I) and s(II) structures, as shown in Fig. 4.6 (b) and (c), showing P4/nmm and P4212 group symmetry, respectively. S(I) structures have Ag_2S, Ag_2Se, Au_2S, and Au_2Se, and s(II) structures have Cu_2S and Cu_2Se monolayers. In a unit cell of s(I/II) A_2B, there are four transition metal atoms sandwiched by two non-metal atoms. S(II)

structures are like distorted s(I) structures, with larger thickness and smaller lattice parameters, as listed in Table 4.1. The chemical bonds between A and B atoms are analyzed by using the electron localization functions (ELFs) and Bader charge analysis [174]. It is found that the electrons are mainly concentrated near B atoms, showing the nature of the ionic bond.
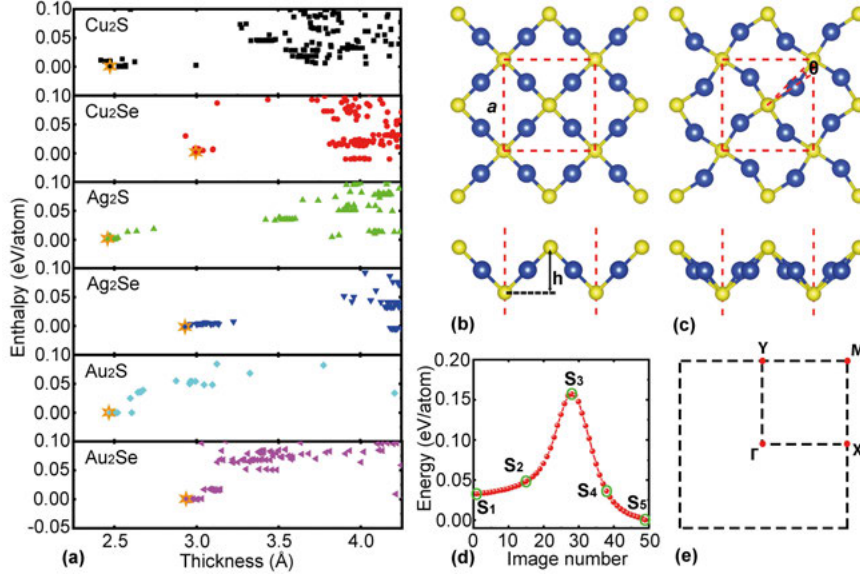
Figure 4.6. (a) The enthalpies of different low-energy allotropes with different thicknesses. The studied structure s-A_2B is indicated by an orange hexagon. The energy of s-A_2B structures is set to zero. (b) and (c) show the geometries of two types of s-A_2B. The unit cells are shown by the red dashed rectangle. (d) The energy change in the phase transition process from s(I)-Ag_2S to monolayer $\alpha - Ag_2S$. (e) shows the first BZ and high symmetry points used in the band structure computations. Reproduced with permission from Paper III. Copyright ©2020 American Chemical Society.

Among the six low energy structures, s(II)-Cu_2S and s(I)-Au_2S were previously predicted by Guo et al. [171] and Wu et al. [175]. It should be noted that s(I)-Ag_2S is different from the reported $\alpha-Ag_2S$ monolayer [117]. We have computed the energy barrier between these two phases of Ag_2S, and the energy change in the transition process is shown in Fig. 4.6 (d). The energy barrier is 124 meV/atom, suggesting that the transition between the two phases is possible at a high temperature.

The cohesive energies have been computed by the following expression:

$$\Delta E = \frac{n_A \times E_A + n_B \times E_B - E_{tot}}{n_A + n_B},\qquad(4.2)$$

where E_{tot}, E_A, and E_B are the energy of the whole system, the plasma state of A and B, respectively. The energetic stability is measured by comparing ΔE

Table 4.1. *The structural type, the lattice constant (a), lattice thickness (h), distortion angle (θ), formation energy (ΔE), and the charge transfer (A to B) computed by Bader charge analysis ($\Delta\rho_A$). Reproduced with permission from Paper III. Copyright ©2020 American Chemical Society.*

Chemical formula	Cu_2S	Cu_2Se	Ag_2S	Ag_2Se	Au_2S	Au_2Se
Type	II	II	I	I	I	I
a(Å)	5.02	4.97	5.88	5.90	5.81	5.82
h(Å)	2.55	3.02	2.49	2.93	2.49	2.95
$\theta(°)$	12.54	14.22	0	0	0	0
ΔE(eV/atom)	3.544	3.322	2.811	2.664	3.104	2.960
$\Delta\rho_A(e)$	0.31	0.21	0.30	0.23	0.19	0.03

with synthesized 2D materials. As given in Table 4.1, the values of ΔE of these 2D A_2B structures are similar to the value of the synthesized 2D materials silicene (3.98 eV/atom) and stanene (2.74 eV/atom), implying good energetic stabilities. To synthesize them, we suggest that the chemical vapor deposition method[169, 176] can be a good candidate.

The dynamical and thermal stability of A_2B monolayers are then considered. As shown in Fig. 4.7, all the phonon modes are above -0.1 Thz, and no obvious imaginary frequencies are observed. Moreover, in the ab initio molecular dynamics simulation, the energies are kept stable, and the structural features are preserved. Both of the two above observations suggest that all the six A_2B 2D structures are dynamically and thermally stable. Moreover, all the phonons are concentrated on the low energy parts, implying low lattice thermal conductivities [177, 178].

4.2.2 Thermal and electronic properties

The lattice thermal conductivities can be computed by using the formula [179]:

$$\kappa_{\alpha\beta} = \frac{1}{SH} \sum_{\lambda} C_{\lambda} v_{\lambda\alpha} v_{\lambda\beta} \tau_{\lambda}, \qquad (4.3)$$

where λ is the phonon mode index, S is the area of the surface, H is the height of the layer, considering the vdW radii [180]. C_{λ} demonstrates the thermal capacity of the phonon mode λ. $v_{lambda\alpha}$ demonstrates the component of the group velocity of phonon mode $lambda$ in the α-direction. τ_{lambda} demonstrates the relaxation time of mode λ. By solving the Boltzmann transport equation (BTE) with ShengBTE code [141, 142], we got k_L of 2D A_2B structures at different temperatures as shown in Fig. 4.7 (h).

The lattice thermal conductivities (κ_L) of the six structures are isotropic, and the values in different temperatures are computed and shown in Fig. 4.7 (h). We compared the room-temperature lattice thermal conductivities of the
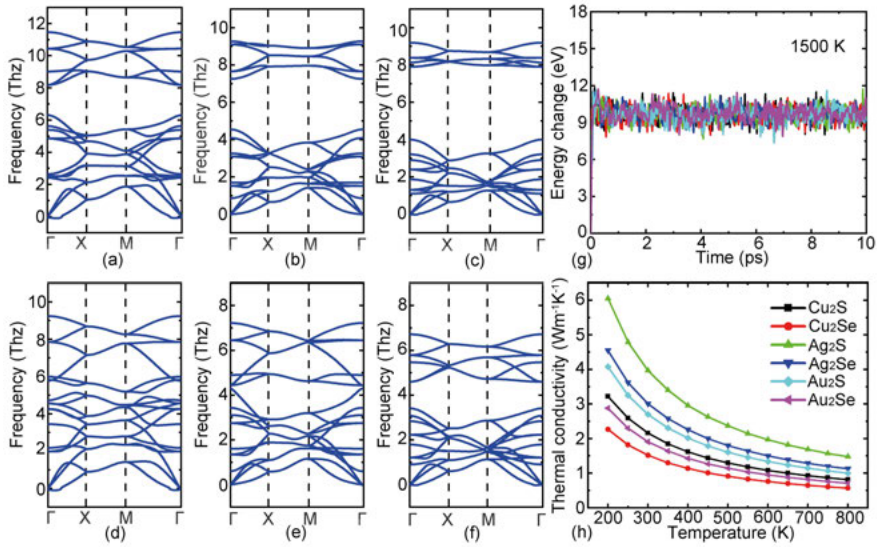
Figure 4.7. (a)-(f) Phonon dispersion spectra of s(II)-Cu_2S, s(I)-Ag_2S, s(I)-Au_2S, s(II)-Cu_2Se, s(I)-Ag_2Se, and s(I)-Au_2Se, respectively. (g) shows the potential energy change of the six structures up to 10 ps at 1500K. (h) shows the lattice thermal conductivities of the six structures. Reproduced with permission from Paper III. Copyright ©2020 American Chemical Society.

six A_2B monolayers with the reported 2D materials with low lattice thermal conductivities such as 2D tellurium, and it is found that A_2B monolayers have lower κ_L [179, 181]. The low lattice thermal conductivities can be explained by the large atomic masses and weak chemical bonding [182, 183].

The electronic properties of s-A_2B monolayers are studied from two aspects, i.e., electronic band structures and electronic transport properties. As shown in Fig. 4.8, all six structures are direct-gap semiconductors with Conduction Band Minimum (CBM) and Valence Band Maximum (VBM) situated at the Γ points. The bandgaps calculated by using PBE and HSE06 functionals are different, as seen in Table 4.2. We have studied the influence of the SOC effect on the electronic band structures. For Cu and Ag systems, the SOC effect is very weak and has a negligible influence on the electronic bandgaps. While for Au systems, the SOC effect is strong and change the bandgap significantly. Thus in the electronic properties calculations for the Au_2B system, the SOC effect should be taken into account. The VBM is mainly contributed by $p_{x,y}$ orbitals of B atoms and d_{xy} orbitals of A atoms, and this is discussed in the Supplemental material of Paper III.

Due to the degeneracy of the VBM of Cu_2B and Ag_2B, there are two types of holes. They have different effective masses in the x- and y-directions, namely heavy holes (hh) and light holes (lh). We computed the carrier mobilities in

the six structures with the deformation potential method [147, 184], which was introduced in Part II.
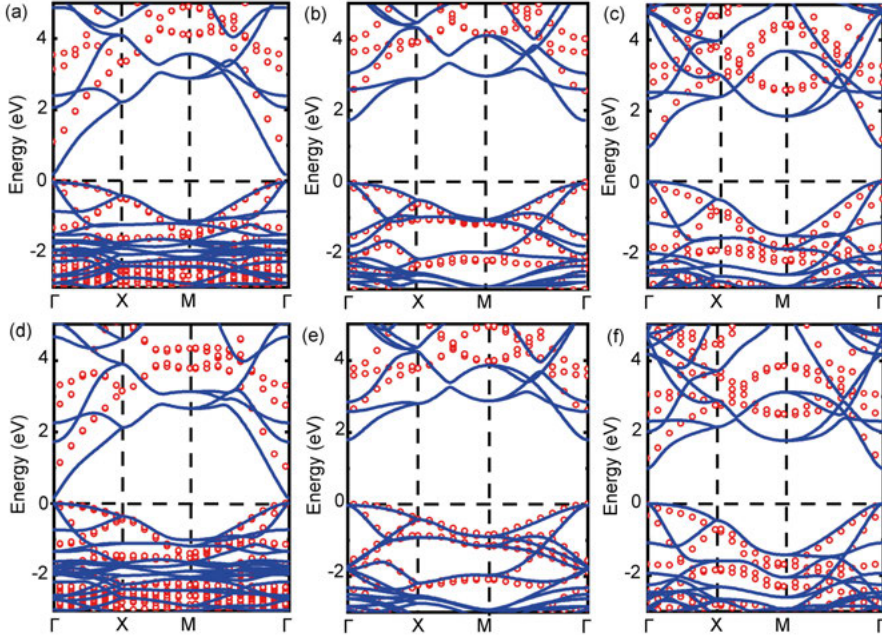

Figure 4.8. (a)-(f) show the band structures of s(II)-Cu$_2$S, s(I)-Ag$_2$S, s(I)-Au$_2$S, s(II)-Cu$_2$Se, s(I)-Ag$_2$Se, and s(I)-Au$_2$Se, respectively. The bands in red circles are obtained by using HSE06 functional and taking the SOC effect into account. The bands in blue are obtained by using PBE functional without the SOC effect. Reproduced with permission from Paper III. Copyright ©2020 American Chemical Society.

The x-direction is set as the transport direction in the calculations. We computed the related parameters as listed in Table 4.3. It is exciting to find that all these structures have high carrier mobilities. The electron mobilities are from $2.93 \times 10^3\ cm^2V^{-1}s^{-1}$ to $4.78 \times 10^4\ cm^2V^{-1}s^{-1}$, which are much larger than existing 2D materials such as black phosphorene ($1.14 \times 10^3\ cm^2V^{-1}s^{-1}$) [185]. The hole mobilities of hh and lh are significantly different. The mechanism of the difference is discussed in the SI of Paper III.

4.2.3 Mechanical properties and strain induced NPR

We computed the mechanical properties by using the energy-strain method[143, 144]. By applying different strain, we can get the elastic tensor by solving

$$U = \frac{1}{2}C_{11}\tau_x^2 + \frac{1}{2}C_{22}\tau_y^2 + C_{12}\tau_x\tau_y + 2C_{66}\tau_{xy}^2, \qquad (4.4)$$

Table 4.2. *The bandgaps (eV) of the six structures computed with different exchange-correlation functionals with and without the SOC effect. Reproduced with permission from Paper III. Copyright ©2020 American Chemical Society.*

Structure	Cu_2S	Cu_2Se	Ag_2S	Ag_2Se	Au_2S	Au_2Se
PBE w.o. SOC	0.226	0.155	1.789	1.810	0.968	0.981
PBE w. SOC	0.173	0.151	1.708	1.771	0.617	0.689
HSE06 w.o. SOC	1.139	1.059	2.638	2.620	1.608	1.609
HSE06 w. SOC	1.091	1.036	2.554	2.601	1.201	1.284

Table 4.3. *The parameters needed for computing the carrier mobilities, including the deformation potential energy E_1 (eV), the 2D elastic modulus C_{2D} (N/m) and the effective mass m^* (m_e). The calculated carrier mobilities (in 10^2 $cm^2V^{-1}s^{-1}$) are also presented. Reproduced with permission from Paper III. Copyright ©2020 American Chemical Society.*

A_2B	Cu_2S			Ag_2S			Au_2S	
carrier	e	hh	lh	e	hh	lh	e	h
E_1	2.41	1.83	-2.70	2.35	2.50	-5.32	1.95	-4.33
C_{2D}	33.7			23.3			31.6	
m^*	0.10	3.73	0.11	0.18	2.67	0.18	0.08	0.12
μ	126	0.150	87.8	29.3	0.110	5.35	306	24.1
A_2B	Cu_2Se			Ag_2Se			Au_2Se	
carrier	e	hh	lh	e	hh	lh	e	h
E_1	1.31	0.82	-2.76	1.97	1.93	-5.63	1.68	-3.11
C_{2D}	36.9			21.0			22.0	
m^*	0.10	3.09	0.10	0.19	3.44	0.19	0.08	0.14
μ	478	1.21	95.1	33.3	0.100	4.08	234	25.8

in which U is the energy change, τ_{xy} is the shear strain, C_{nn} are the elastic modulus tensors. By fitting the curves of $U(\tau_x, \tau_y, \tau_{xy})$, we got all the tensor components listed in Table 4.4.

Table 4.4. *The stiffness tensor components (N/m) of the six structures. Reproduced with permission from Paper III. Copyright ©2020 American Chemical Society.*

Structure	Cu$_2$S	Cu$_2$Se	Ag$_2$S	Ag$_2$Se	Au$_2$S	Au$_2$Se
C11	33.7	36.9	23.3	21.0	31.6	22.0
C12	2.7	7.6	3.1	3.1	10.1	8.0
C22	33.7	36.9	23.3	21.0	31.6	22.0
C66	19.4	17.3	10.7	10.7	15.2	13.9
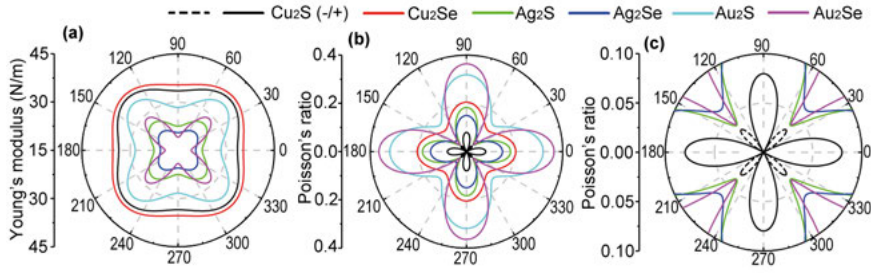
Figure 4.9. The direction-dependent in-plane Young's moduli (a) and Poisson's ratios (b) of s-A$_2$B structures. The central part of the Poisson's ratios diagram is enlarged and shown in (c). Reproduced with permission from Paper III. Copyright ©2020 American Chemical Society.

We computed the Young's moduli and Poisson's ratios by

$$E_{2D}(\theta) = \frac{C_{11}C_{22} - C_{12}^2}{C_{11}\sin^4\theta + C_{22}\cos^4\theta + \left(\frac{C_{11}C_{22}-C_{12}^2}{C_{66}} - 2C_{12}\right)\cos^2\theta\sin^2\theta},$$
(4.5)

and

$$\vartheta(\theta) = -\frac{\left(C_{11} + C_{22} - \frac{C_{11}C_{22}-C_{12}^2}{C_{66}}\right)\cos^2\theta\sin^2\theta - C_{12}\left(\cos^4\theta + \sin^4\theta\right)}{C_{11}\sin^4\theta + C_{22}\cos^4\theta + \left(\frac{C_{11}C_{22}-C_{12}^2}{C_{66}} - 2C_{12}\right)\cos^2\theta\sin^2\theta},$$
(4.6)

[145, 146], respectively. In these formulae, θ is the direction angle, and the x-direction is set as $\theta = 0$. The polar diagrams are shown in Fig. 4.9. The Young's moduli of all the six structures are smaller than 40 N/m. In comparison, the 2D Young's modulus of graphene is 335 N/m [186]. The low Young's moduli show that 2D A$_2$B structures are extraordinarily flexible. Five of the pristine A$_2$B structures show positive Poisson's ratio, while s(II)-Cu$_2$S show negative Poisson's ratio along $\theta = 45 \times n(n = 1, 2, 3, 4)$ directions.

With strain, the mechanical properties may change. In this work, we computed the change of the Poisson's ratios as a function of the external uniaxial strain. As shown in Fig. 4.10, we computed the mechanical response of A_2B monolayers under the uniaxial strain. It is found that by applying strain along the [110]-direction, the out-of-plane Poisson's ratios are approximately unchanged, while the in-plane Poisson's ratios change significantly. Notably, most of these materials can be tuned to have negative Poisson's ratios. In particular, the Poisson's ratio of Cu_2S can be tuned to -1.68 with proper strain, much larger than the reported 2D in-plane NPRs.
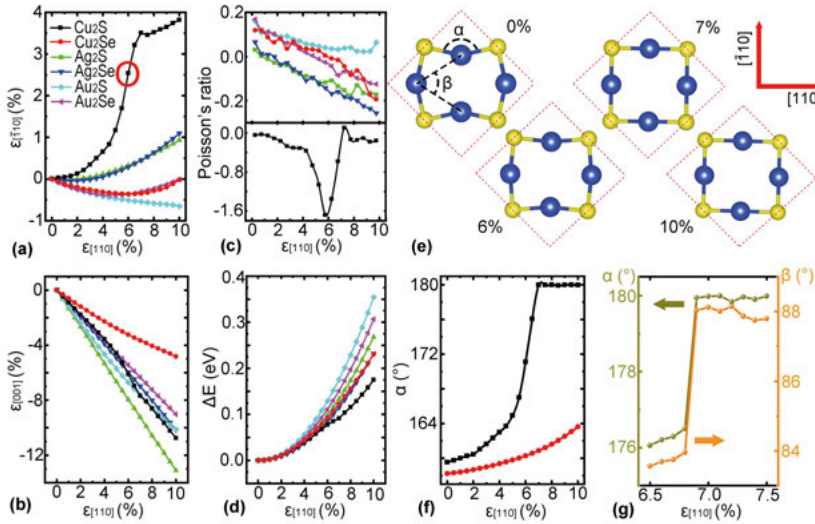
Figure 4.10. (a) and (b) show the in-plane and out-of-plane mechanical response under strain along the [110]-direction. (c) shows the Poisson's ratios under different strains. (d) contains potential energy curves under different strains. (e) shows the structures of s(II)-Cu_2S under different strain. (f) and (g) show the change of α and β under strain. (f) is the change of α in s(II)-Cu_2S and s(II)-Cu_2Se, and (g) is the change of both α and β in s(II)-Cu_2S. Reproduced with permission from Paper III. Copyright ©2020 American Chemical Society.

Moreover, by checking the energy, we proved that the unusual large negative Poisson's ratio does not arise from the structural phase transition. Indeed, there is no energy barrier between the s(II)-phase and s(I)-phase of Cu_2S, Cu_2Se, Ag_2S, Ag_2Se, and Au_2S. This observation is an important starting point of the following work.

4.3 Structural phase transition in single-layer gold(I) telluride

In recent years, a class of new 2D materials, transition metal dichalcogenides have been studied extensively[67, 68, 69, 70]. Different from graphene, 2D transition metal dichalcogenides have numerous polymorphs, including the insulating phase, the metallic phase, and the phase of topological insulator (TI)[187, 102]. Among these, 1H and 1T′ $MoTe_2$ are quite extraordinary: the geometries and energies of these two phases are quite close, which makes the phase transition possible. Recent researches have revealed that the structural phase transition between the two phases can be driven by thermal means [109, 110], electrostatic doping[101], electrostatic gating [111, 105, 112], and photoexcitation [188]. Because of this feature, 1H and 1T′ $MoTe_2$ are promising materials for potential applications in electronic switches, electronic oscillators, memristive devices, thermal sensors, and chemical sensors [102, 189, 104, 105, 188]. These aspects have attracted more research interest in other phase transition materials (PTMs) with different electronic states.

In the previous chapter, we discussed the 2D forms of A_2B (A=Cu, Ag, Au; B=S, Se) structures. There are two structural forms, i.e., s(I) and s(II). With uniaxial strain, for Cu_2S, Cu_2Se, Ag_2S, and Ag_2Se, the distortion of s(II) structure will decline, and the structure will become a s(I)-like structure. However, due to the absence of energy barriers in this process, the induced s(I)-like structure will automatically turn back to s(II) form, which makes them not suitable for application as PTMs. For Au_2Se, both s(I) and s(II) phases are stable. There is an energy barrier between the two phases. However, since the energy barrier is quite small and the energy of compressed s(I)-Au_2Se has lower energy than s(II)-Au_2Se, it is also not suitable for application as a PTM. But this inspired us to study other A_2B structures for searching PTMs.

4.3.1 Structure search and stability

We have performed an evolutionary structure search for the 2D forms of A_2Te. Interestingly, in our computation, the lowest energy structure of Au_2Te is found to be in the s(II) form. Naturally, we studied the possibility of 2D Au_2Te as a PTM by computing the stability of s(I)-Au_2Te and the energy barrier between the two phases.

The fully relaxed s(II) and s(I) structures are shown in Fig. 4.11 (a). In comparison, after being fully relaxed, s(I)-Cu_2S and s(I)-Cu_2S will go back to s(II) form. The structural and energetic data are listed in Table 4.5. Notably, s(I) phase Au_2Te has a larger lattice parameter than s(II) phase, which makes it possible to get s(I)-Au_2Te by applying tensile strain to s(II) Au_2Te.
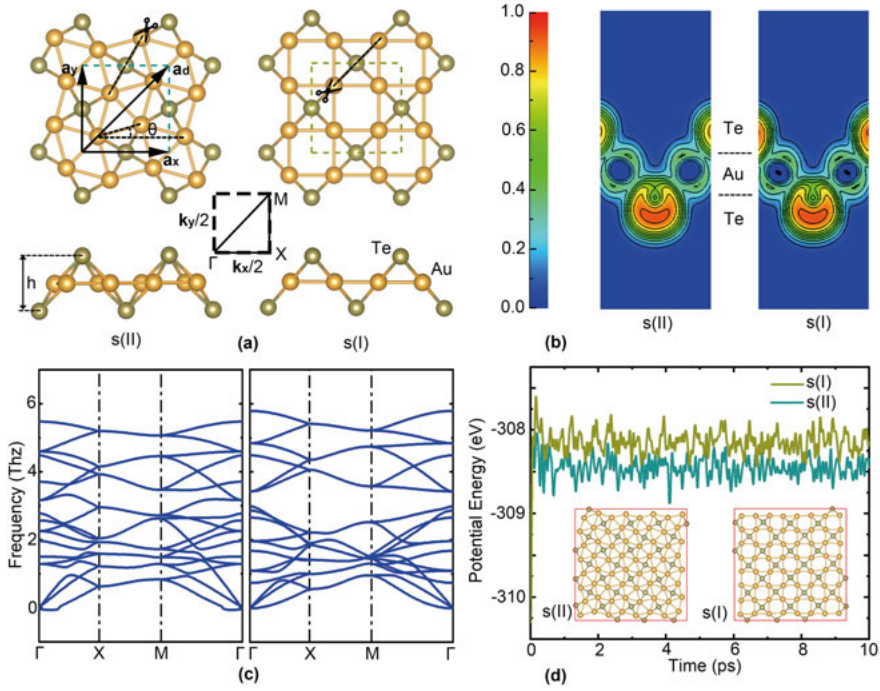
Figure 4.11. (a) The geometries of the two phases of s-Au$_2$Te. The unit cells are in the green and brown dashed rectangle. The high symmetric path used in calculating the band structures is shown as the black dashed rectangle. (b) shows the contour plots of the ELFs of the two structures, slices along the black dashed lines in (a). (c) are the two phonon spectra of the two s-Au$_2$Te structures. (d) is the energy change of the structure at room temperature up to 15 ps. Reproduced from Paper V.

Table 4.5. *The lattice constants a_x and $a_{[}d]$ (Å), the lattice thickness h (Å), the distortion angle θ (°), the formation energy ΔE (eV/atom), and the stiffness tensors C_{mn} (N/m) of s-Au$_2$Te. Reproduced from Paper V.*

Phase	a_x	a_d	h	θ	ΔE	C11	C12	C66
s(I)	5.85	8.27	3.44	0	-2.893	23.460	5.953	12.301
s(II)	5.61	7.93	3.55	15.28	-2.897	34.798	19.006	14.199

The energetic stability is measured by the formation energy as

$$\Delta E = \frac{E_{Au_2Te} - (n_{Au} \times E_{Au} + n_{Te} \times E_{Te})}{n_{Au} + n_{Te}}, \qquad (4.7)$$

where E_{Au_2Te} is the energy of monolayer Au_2Te. E_{Au} and E_{Te} are the energies of Au and Te atoms in plasma states. The values of s(I)- and s(II)-Au_2Te are comparable to that of germanene and stanene, i.e., -3.26 eV/atom and -2.74 eV/atom, respectively [190].

The dynamical and thermal stability of s(I/II)-Au_2Te is confirmed by their phonon spectra and the BOMD results. As shown in Fig. 4.11(c), there are no or only tiny imaginary frequencies in the phonon spectra. From the BOMD simulation results, as shown in Fig. 4.11(d), it is found that in 300 K, the energies of the two structures are both kept stable. Both of the two above observations show that s(I/II)-Au_2Te are dynamically and thermally stable. The mechanical stabilities are proved by the Born-Huang criteria: C_{11}, C_{22}, and $C_{66} > 0$, and $|C_{11} + C_{22}| > |2C_{12}|$, in which C_{nn} are the elastic tensor components of s(I/II)-Au_2Te as listed in Table 4.5.

4.3.2 Structural phase transition

The structural phase transition between the two phases is studied. By applying uniaxial strain along the [110]-direction on s(II)-Au_2Te, we can spread the distorted structure and transfer it to s(I) phase, as shown in Fig. 4.12. The transition occurs when a_d=8.4 Åwithout considering the temperature. Moreover, the energy barrier is about 19 meV/atom. If we consider temperature, the phase transition may happen by applying a smaller tensile strain.

On the other hand, in the phase transition from s(I) to s(II) phase, the lattice parameter is decreased. Compared with tensile strain, applying compressing strain on 2D materials is quite hard, and thus we need other methods to induce the phase transition. Since s(I) phase has higher energy than s(II) phase, by heating and annealing s(I)-Au_2Te, we may get the lowest energy structure, i.e., s(II) phase. We computed the energy barrier in the phase transition by employing variable cell nudged elastic (VC-NEB)[191]. The energy barrier is about 7.8 meV/atom, suggests that the phase transition can be induced by a small thermal perturbation.

In the work, we have also investigated the electric field effect on the phase transition. The energy difference between the two phases is varying in different electric fields, as shown in Fig. 4.12(b). With an electric field of above 0.78 eV/Å, the s(I) phase has lower energy than the s(II) phase. Thus, with the assistant of heat, an electric field induced phase transition may be achieved.
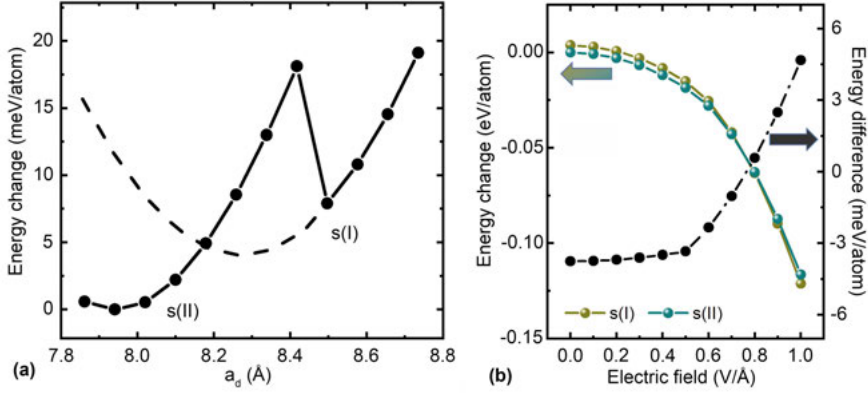
Figure 4.12. (a) The energy of s(I)- and s(II)-Au_2Te, with respect to the lattice parameter a_d. The two local minimums are the energies of the fully optimized s-Au_2Te structures. (b) The energy change of the two phases as a function of the external electric field. The energy difference between the two phases is plotted in black points and lines. Reproduced from Paper V.

4.3.3 Electronic and mechanical properties

As PTMs, distinguishable electronic and mechanical properties of the two phases are important. The electronic properties of 2D s(I)-Au_2Te is studied by computing its electronic band structures and carrier mobilities. As shown in Fig. 4.13 (a), s(I)-Au_2Te is a direct-gap semiconductor, similar to other s-A_2B structures in previous chapter. The band gaps with and without SOC are 1.470 eV and 1.252 eV, respectively.
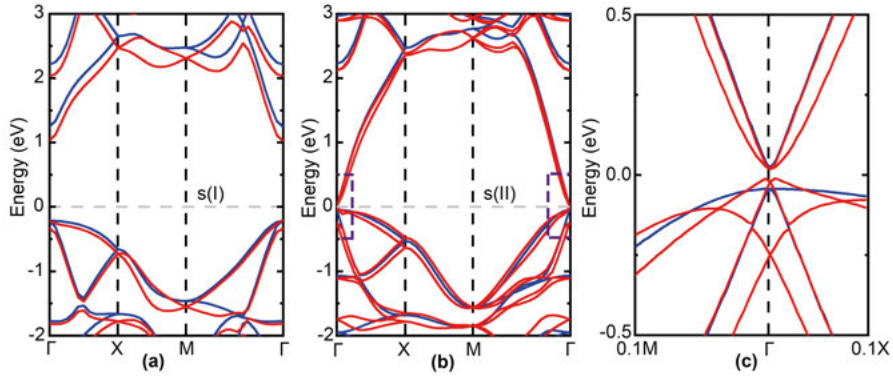

Figure 4.13. (a) and (b) are the band structures of s(I)- and s(II)-Au_2Te, respectively. (c) is the enlarged bands near the Γ point. The blue and red lines are the bands without and with the SOC effect, respectively. Reproduced from Paper V.

The carrier mobilities are computed by employing the deformation potential method discussed in Part II [147, 184]. At 300 K, the electron mobility is

$3.45 \times 10^4 cm^2/(Vs)$, and the hole mobility is $6.466 \times 10^3 cm^2/(Vs)$. Both of the values are much larger than that of 1-H MoS_2 and black phosphorus [185, 192, 193], promising applications in 2D devices.

The electronic properties of s(I)-Au2Te are studied start from computing the electronic band structures, as shown in Figs. 4.13 (b) and (c). Without SOC, there is a direct band-gap of 68 meV at Γ point. While with SOC, the band-gap is decreased t 28 meV. To investigate how the SOC effect narrows the band-gap, we performed a series of calculations with different SOC strengths. The band-gap as a function of SOC strength (λ_{SOC}) is shown in Fig. 4.14. It is found that from $\lambda_{SOC} = 0$ to $\lambda_{SOC} = 0.7$, the band-gap decreases to zero. For $\lambda_{SOC} > 0.7$, the band-gap is always increasing. This implies a band inversion happened in s(II)-Au_2Te, which induces a nontrivial topological property. Then we confirmed that it is a topological insulator by the Wannier charge center changes, which is discussed in detail in Paper V.
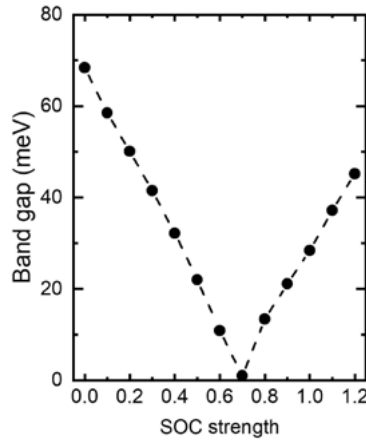

Figure 4.14. The band-gap of s(II)-Au_2Te as a function of SOC strength. Reproduced from Paper V.

The mechanical properties are investigated by computing the Poisson's ratio and Young's modulus, as shown in Fig. 4.15(a) and (b). Pristine s(I/II)-Au_2Te structures have positive Poisson's ratios and ultra-small in-plane Young's moduli, similar to other A_2B structures. In all the directions, the Poisson's ratios of s(I) phase are always smaller than those of the s(II) phase.

Strain-induced large in-plane negative Poisson's ratios are observed in most other A_2B monolayers in the previous chapter. Naturally, we investigated the mechanical response of s-Au_2Te by applying uniaxial strain along the [110]-direction. As shown in Fig. 4.15 (c) and (d), s(I)-Au_2Te show in-plane NPR and out-of-plane positive Poisson's ratio under strain larger than 2%, while s(II)-Au_2Te always shown positive Poisson's ratios in both in-plane and out-of-plane directions.
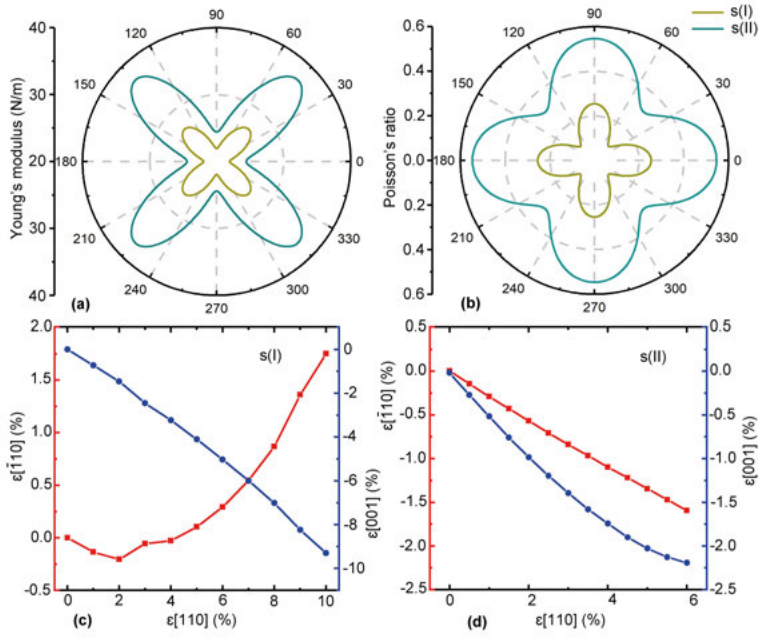
Figure 4.15. The direction-dependent in-plane (a) Young's moduli and (b) Poisson's ratios of s-Au_2Te. (c) and (d) are the in-plane and out-of-plane mechanical response of s(I)- and s(II)-Au2Te under strain along the [110]-direction. Reproduced from Paper V.

5. Interface between 2D materials and substrates

For most of the applications of 2D materials, proper substrates are needed. The 2D material may interact strongly with the substrate and show quite different properties from the free-standing case. On the other hand, the 2D materials may change the properties of substrates as well. Thus, investigating the interaction between 2D materials and the substrates is important for understanding the properties of the heterostructures.

Damping-like spin-orbit torques (SOTs) can realize the controlling of magnetization with spin-polarized currents at a low-energy cost and has enormous applications in spintronic devices [194, 195, 196]. Unlike spin-transfer torque (STT), the origin of the SOT is not the spin-polarized charge transfer but the angular momentum transfer. Compared to spin-polarized charge transfer, the momentum transfer costs much lower energy. In SOTs, the spin-polarized currents are usually generated by the spin Hall effect or Rashba-Edelstein effect, originally from the spin-orbit coupling. Since strong spin-orbit coupling is always found in heavy atoms, most SOTs are achieved in heavy metals. However, it is hard to control the thickness of heavy metals since they tend to become bulk structures. To overcome this problem, 2D-TMDs on ferromagnets were proposed to provide strong spin-orbital coupling [197, 198].

5.1 Monolayer 1T-tantalum-disulfide on NiFe (Py) ferromagnetic layer

Freestanding monolayer 1T-TaS_2 shows charge density wave (CDW) structure. However, the energy difference between the CDW state and the undistorted 1T phase (as shown in Fig. 5.1 (a)) is not so large, which indicates that it can be easily destroyed by interface interaction. In the work, we studied structural, electronic, and magnetic properties of monolayer TaS_2 on NiFe (Py) substrate to discuss the origin of the strong SOC effect in the 2D TaS_2 based large damping-like spin-orbital torque [199].

The optimized geometry structure of 2D 1T-TaS_2 is shown in Fig. 5.1 (a). There are three atomic layers: a Ta atomic layer is sandwiched by two S layers. The band structure of 2D 1T-TaS_2 with and without SOC is shown in Fig. 5.1 (b). It always shows metallic feature. With SOC effect, there are significant band splittings near the Γ point, i.e., the degeneracy of d_{xz} and d_{yz} bands are broken.

74

The heterostructure is constructed by a 1×3 TaS$_2$ supercell and a 1×5 Py supercell, in which the mismatch is less than 5.1%. We set the lattice parameter of Py to be 3.54 Å, according to the reported data of Py thin films. The Py substrate is simulated by a five-atomic-layer slab, in which the two bottom layers are fixed. To simulate the low symmetry of alloy, we generated the structure with evolutionary algorithm using USPEX code. The optimized TaS$_2$ structure as shown in Fig. 5.1 (c) is quite different from the free-standing case. It is found that the bottom S atoms are chemically bonded with the substrate, and the strong interaction deformed the lattice structure of TaS2. The resulting structure is similar to the 1T′ phase of MoS$_2$, the distances between two nearest Ta atoms become different.

In TaS$_2$/Py heterostructure, the degeneracy near Γ point is already lifted due to the breaking of symmetry from the structural distortion and magnetism. Moreover, we plotted the projected density of states (DOS) with and without Py substrate. In pristine 1T-TaS$_2$, the states near the Fermi level are mainly contributed by the d_{xy}, d_2, and d_{xz} orbitals of Ta, and these orbitals are influenced strongly by the spin orbit couplings. In the heterostructure, in the vicinity of the Fermi level, the d_{z^2} orbitals of Ta are prominent for both spin channels. A hybridization is found between the d_{z^2} atomic orbitals of Ta and Ni atoms.
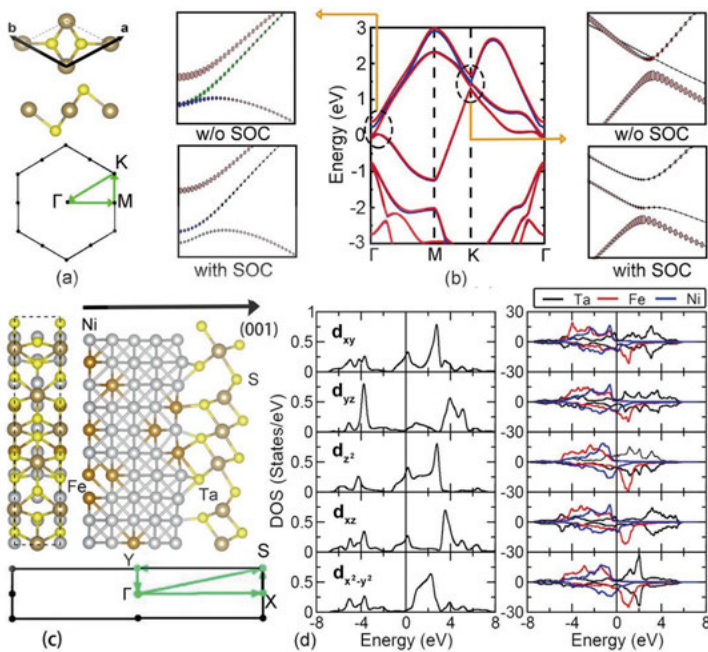
Figure 5.1. (a) The primary cell of the pristine 1T-TaS$_2$, and its first BZ shown in the black hexagon. (b) The electronic band structure and atomic orbital projected bands of 1T-TaS$_2$. (c) The structure of the heterostructure and its first BZ. (d) The d atomic orbital projected density of states of pristine 1T-TaS$_2$ and the TaS$_2$/Py heterostructure. Reproduced with permission from Paper VI. Copyright ©2020 American Chemical Society.

Part III:
Final Summaries & Remarks

6. Summary and outlook

In this thesis, a theoretical study employing the DFT framework is conducted on the two-dimensional materials on their electronic, magnetic, mechanical, and thermal properties. The thesis is mainly constructed in five chapters, and a overall diagram is presented as Fig. 6.1.

In the first chapter, the background of 2D materials is introduced, and the importance and motivations of related studies are presented. In the second chapter, the density functional theory and approximations are first described, including Hohenberg-Kohn theorems, Kohn-Sham formalism, local density approximation, generalized gradient approximation, and pseudopotential. Then we introduced the mechanism of evolutionary structure search and the detailed method to compute the thermal conductivities, mechanical properties, and carrier mobilities of 2D materials.
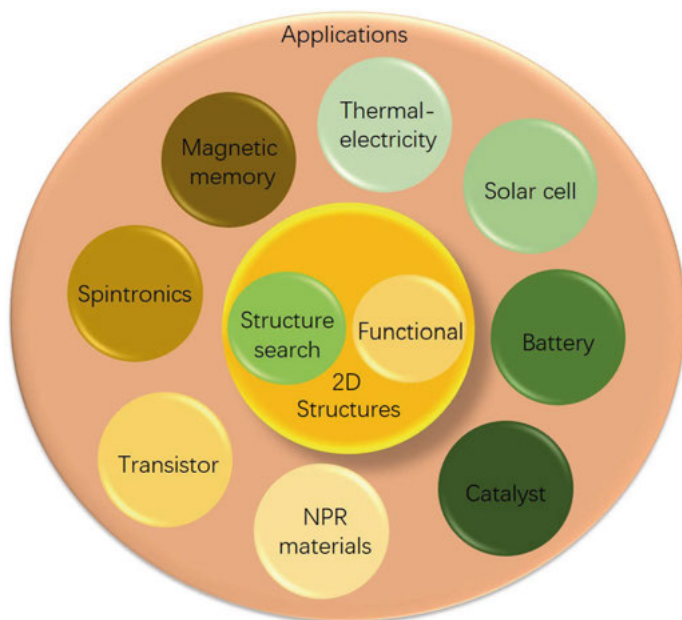
Figure 6.1. Overview of the topics and outlooks in this thesis.

In the third chapter, I discussed the effect of chemical adsorption on the properties of 2D materials, including two systems. The first system is transition metal clusters on graphene with defects. In this study, the self-assembly

processes of 3d transition metal (Cr, Mn, Fe) hexamers are simulated. In 300 K, the isolated transition metal atoms or clusters can move fast on pristine graphene and stuck at defect sites. Starting from the optimization of BOMD resulting structures, the ground state and metastable structures are studied, finding that Fe hexamers on defect graphene are ferromagnetic, while Cr and Mn hexamers show ferrimagnetic structures, in good agreement with the experiment. The magnetic anisotropy energy of the structures reveals that Cr@DV-Gr and Fe@DV-Gr have quite small magnetic anisotropy energy.

Further calculations show that the external electric field can tune the magnetic anisotropy energy and switch the easy axes. Finally, this property comes from the d_{z^2} and d_{yz} orbitals of trapped atoms, whose electric properties were affected by the external electric field-induced electron density reconstruction. Moreover, the magnetic property makes Cr@DV-Gr and Fe@DV-Gr promising materials for electric-assisted magnetic recording. The second system is the oxidized forms of two type dumbbell silicene. The two ODB structures are proven stable from both the energetic aspect and the dynamics aspect. The electronic band structures are calculated, showing that both ODB-h and ODB-z are semimetals with high Fermi velocities. Moreover, the Dirac points are reproduced by simple TB models using only p_x, p_y orbitals of oxygen atoms. The functionalization introduced new properties that make the two materials promising for high-density magnetic recording and quantum computing.

In the fourth chapter, three works have been introduced. We predicted three types of 2D materials with different chemical composites and novel properties based on the evolutionary structure search in the three works. The first discussed work is about a new allotrope of graphene, PAI-graphene. It is energetically close to graphene and favored than most other 2D carbon allotropes, including many synthesized structures. PAI-graphene is a semimetal with highly distorted Dirac cones. With tensile strain, the Dirac cone can move in different Direction lines. Furthermore, with proper strain, the Dirac cone can vanish.

The second work is about the 2D forms of A_2B (A=Cu, Ag, Au; B=S, Se). The energetically favored structures are square-A_2B structure and its distorted form. The ground state structures are all direct-gap semiconductors with superior carrier conductivity and low lattice thermal conductivity. Moreover, it is found that most of these materials have unusual negative Poisson's ratios. The third work is about the two-dimensional forms of Au_2Te. We discussed the low energy structures of Au_2Te, i.e., s(I) and s(II), and investigated the structural phase transfer mechanism. Since s(I)-Au_2Te are a direct-gap semiconductor, and s(II)-Au_2Te is a topological insulator, the structural phase transition is accompanied by an apparent electronic property change.

The fifth chapter is about an experimental work, in which we studied the structural, electronic, and magnetic properties of 1T-TaS_2 on the alloy of Ni and Fe. Due to the interface effect, a significant distortion of 1T-TaS_2 is observed, which is quite similar to the 1T′ phase of MoS_2. Furthermore, detailed electronic properties are also discussed. A strong hybridization between the

d_{z^2} atomic orbitals of Ta and Ni atoms has been found, which may enhance the SOC effect in Py and induce the large damping-like spin-orbit torque.

Though many 2D ferromagnetic materials have been synthesized or predicted, the Curie temperatures are often quite low. For example, the most studied 2D ferromagnetic material with the out-of-plane magnetic axis, monolayer CrI_3 shows ferromagnetic properties under 45 K [200]. The low Curie temperature has dramatically hindered the application of 2D materials in low-dimensional spintronic devices.

Renewable energy materials, including solar cells, catalysts, batteries, and thermoelectric materials, are required when the global warming is becoming a severe threat. 2D materials, due to the large specific surface area and many other novel properties, may have promising applications in these fields.

In the future, I would like to continue the research in 2D materials, possibly do some studies in 2D magnetic materials and renewable energy materials.

7. Svensk sammanfatting

I denna avhandling genomförs en teoretisk studie som använder DFT-ramverket på tvådimensionella material med avseende på deras elektroniska, magnetiska, mekaniska och termiska egenskaper. Avhandlingen är huvudsakligen uppbyggd i fem kapitel och ett övergripande diagram presenteras som Figur 7.1.

I det första kapitlet introduceras bakgrunden till 2D-material och betydelsen och motivationen för relaterade studier presenteras. I det andra kapitlet beskrivs först densitetsfunktionsteorin och approximationer, inkluderande Hohenberg-Kohn-teoremet, Kohn-Sham-formalism, den lokala densitetsuppskattningen, den generaliserade gradientuppskattningen och pseudopotential. Sedan introducerade vi mekanismen för evolutionär struktursökning och den detaljerade metoden för att beräkna värmeledningsförmåga, mekaniska egenskaper och mobiliteter av laddningsbärare för 2D-material.
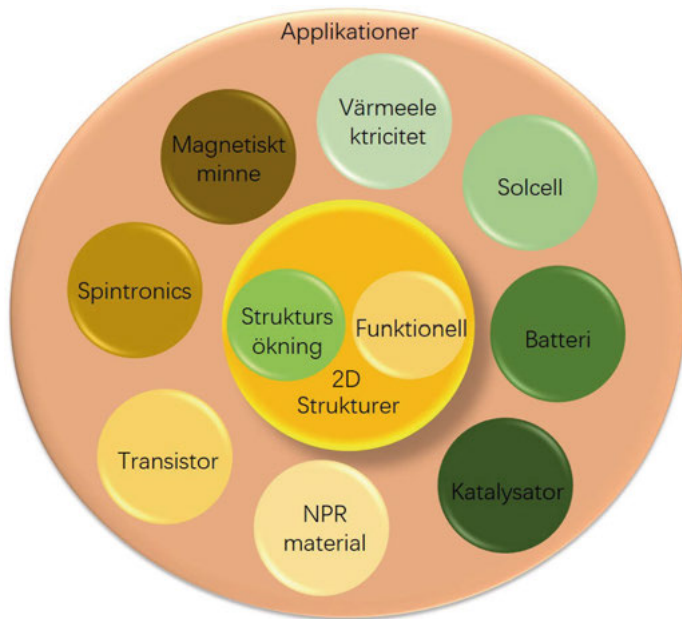

Figure 7.1. Översikt över ämnen och utsikter i denna avhandling.

I det tredje kapitlet diskuterade jag effekten av kemisk adsorption på egenskaperna hos 2D-material, inklusive två system. Det första systemet är övergångsmetallkluster på grafen med defekter. I denna studie simuleras självtillväxtprocesserna för 3d-övergångsmetall (Cr, Mn, Fe) hexamerer. Vid 300 K kan de

isolerade övergångsmetallatomerna eller klusterna röra sig snabbt på pristin grafen och fastna vid defektställen. Med utgångspunkt från optimeringen av BOMD-producerade strukturer studeras grundtillståndet och metastabila strukturer och vi finner att Fe-hexamerer på defektgrafen är ferromagnetiska, medan Cr- och Mn-hexamerer visar ferrimagnetiska strukturer, i god överensstämmelse med experimentet. Strukturernas magnetiska anisotropienergi avslöjar att Cr@DV-Gr och Fe@DV-Gr har ganska liten magnetisk anisotropenergi.

Ytterligare beräkningar visar att ett externt elektriskt fält kan ställa in den magnetiska anisotropienergin och växla de enkla axlarna. Slutligen kommer den här egenskapen från d_{z^2} och d_{yz} orbitaler av infångade atomer, vars elektriska egenskaper påverkades av den externa elektriska fältinducerade elektrontäthetsrekonstruktionen. Dessutom gör den magnetiska egenskapen Cr@DV-Gr och Fe@DV-Gr lovande material för elektrisk assisterad magnetisk inspelning. Det andra systemet är två oxiderade former av hantel silicen (ODB). De två ODB-strukturerna har visat sig vara stabila ur både den energetiska och dynamiska aspekten. De elektroniska bandstrukturerna beräknas, vilket visar att både ODB-h och ODB-z är halvmetaller med höga Fermi-hastigheter. Dessutom reproduceras Dirac-punkterna av enkla TB-modeller som endast använder p_x, p_y orbitaler av syreatomer. Funktionaliseringen introducerade nya egenskaper som gör de två materialen lovande för magnetisk inspelning och kvantdatorer.

I det fjärde kapitlet har tre projekt introducerats. Vi förutspådde tre typer av 2D-material med olika kemiska samansättning och nya egenskaper baserat på den evolutionära struktursökningen i de tre verken. Det första diskuterade projektet handlar om en ny allotrop av grafen, PAI-grafen. Det är energiskt nära grafen och gynnat än de flesta andra 2D-kol-allotroper, inklusive många syntetiserade strukturer. PAI-grafen är en halvmetall med mycket förvrängda Dirac-koner. Med dragspänning kan Dirac-konen röra sig i olika riktningslinjer. Dessutom, med rätt belastning, kan Dirac-konen försvinna.

Det andra projektet handlar om 2D-formerna av A_2B (A = Cu, Ag, Au; B = S, Se). De energiskt gynnade strukturerna är square-A_2B strukturen och dess förvrängda form. Grundtillståndsstrukturerna är alla halvledare med direkta gap med överlägsen strömledningsförmåga och låg värmeledningsförmåga. Dessutom har det visat sig att de flesta av dessa material har ovanliga negativa Poissons förhållanden. Det tredje projektet handlar om tvådimensionella former av Au_2Te. Vi diskuterade strukturerna med låg energi för Au_2Te, dvs s(I) och s(II), och undersökte den strukturella fasöverföringsmekanismen. Eftersom s(I)-Au_2Te är en halvledare med direkt gap, och s(II)-Au_2Te är en topologisk isolator åtföljs strukturfasövergången av en uppenbar elektronisk egenskapsförändring.

Det femte kapitlet handlar om ett experimentellt projekt där vi studerade de strukturella, elektroniska och magnetiska egenskaperna av 1-TaS_2 på legeringen av Ni och Fe. På grund av gränsskiktseffekten observeras en signifikant förvrängning av 1T-TaS_2, vilken är ganska likt 1T′ fasen av MoS_2.

Dessutom diskuteras detaljerade elektroniska egenskaper. En stark hybridisering mellan d_{z^2} atomorbitaler av Ta- och Ni-atomer har hittats, vilken kan öka SOC-effekten i Py och inducera det stora dämpningsliknande spinn-ban rörelsemängdsmomentet. Även om många 2D-ferromagnetiska material har syntetiserats eller förutsagts, är Curie-temperaturerna ofta ganska låga. Till exempel, det mycket studerade 2D ferromagnetiska materialet CrI_3 med en magnetisk axel vinkelrät på planet visar ferromagnetiska egenskaper för temperaturer lägre än 45K [198]. Den låga Curie-temperaturen har dramatiskt hindrat tillämpningen av 2D-material i lågdimensionella spintroniska enheter.

Förnybara energimaterial, inklusive solceller, katalysatorer, batterier och termo-elektriska material, krävs när den globala uppvärmningen blir ett allvarligt hot. 2D-material, på grund av den stora specifika ytan och många andra nya egenskaper, kan ha lovande tillämpningar inom dessa områden.

8. Acknowledgements

References

[1] R. Peierls. Quelques propriétés typiques des corps solides. *Annales de l'institut Henri Poincaré*, 5(3):177–222, 1935.

[2] Lev Davidovich Landau and Evgenii Mikhailovich Lifshitz. *Statistical physics (in Russian)*. Nauka, 1964.

[3] Lev Davidovich Landau. On the theory of phase changes ii. *phys. Z. Soviet Union*, 11(545):26–35, 1937.

[4] N David Mermin. Crystalline order in two dimensions. *Physical Review*, 176(1):250, 1968.

[5] JA Venables, GDT Spiller, and M Hanbucken. Rep prog phys. *Rep. Prog. Phys.*, 47:399–459, 1984.

[6] K. S. Novoselov, A. K. Geim, S. V. Morozov, D. Jiang, Y. Zhang, S. V. Dubonos, I. V. Grigorieva, and A. A. Firsov. Electric field in atomically thin carbon films. *Science*, 306(5696):666–669, 2004.

[7] K. S. Novoselov, A. K. Geim, S. V. Morozov, D. Jiang, M. I. Katsnelson, I. V. Grigorieva, S. V. Dubonos, and A. A. Firsov. Two-dimensional gas of massless Dirac fermions in graphene. *Nature*, 438(7065):197–200, 11 2005.

[8] Yuanbo Zhang, Yan-Wen Tan, Horst L. Stormer, and Philip Kim. Experimental observation of the quantum Hall effect and Berry's phase in graphene. *Nature*, 438(7065):201–204, 11 2005.

[9] Baojie Feng, Zijing Ding, Sheng Meng, Yugui Yao, Xiaoyue He, Peng Cheng, Lan Chen, and Kehui Wu. Evidence of silicene in honeycomb structures of silicon on Ag(111). *Nano Lett.*, 12(7):3507–3511, 7 2012.

[10] Patrick Vogt, Paola De Padova, Claudio Quaresima, Jose Avila, Emmanouil Frantzeskakis, Maria Carmen Asensio, Andrea Resta, Bénédicte Ealet, and Guy Le Lay. Silicene: Compelling experimental evidence for graphenelike two-dimensional silicon. *Physical Review Letters*, 108(15), 2012.

[11] Mickael Derivaz, Didier Dentel, Régis Stephan, Marie Christine Hanf, Ahmed Mehdaoui, Philippe Sonnet, and Carmelo Pirri. Continuous Germanene Layer on Al(111). *Nano Lett.*, 15(4):2510–2516, 2015.

[12] Young-Woo Son, Marvin L Cohen, and Steven G Louie. Energy Gaps in Graphene Nanoribbons. *Physical Review Letters*, 97(21):216803, 11 2006.

[13] Xiaoyang Zhao, Linyang Li, and Mingwen Zhao. Lattice match and lattice mismatch models of graphene on hexagonal boron nitride from first principles. *Journal of Physics: Condensed Matter*, 26(9):095002, 3 2014.

[14] Harman Johll, Hway Chuan Kang, and Eng Soon Tok. Density functional theory study of Fe, Co, and Ni adatoms and dimers adsorbed on graphene. *Physical Review B*, 79(24):245416, 6 2009.

[15] Jia-An Yan, Lede Xian, and M Y Chou. Structural and Electronic Properties of Oxidized Graphene. *Physical Review Letters*, 103(8):086802, 8 2009.

[16] S. H.M. Jafri, K Carva, E Widenkvist, T Blom, B Sanyal, J Fransson, O Eriksson, U Jansson, H Grennberg, O Karis, R A Quinlan, B C Holloway, and K Leifer. Conductivity engineering of graphene by defect formation. *Journal of Physics D: Applied Physics*, 43(4):045404, 2 2010.

[17] Alex W. Robertson, Barbara Montanari, Kuang He, Christopher S. Allen, Yimin A. Wu, Nicholas M. Harrison, Angus I. Kirkland, and Jamie H. Warner. Structural reconstruction of the graphene monovacancy. *ACS Nano*, 7(5):4495–4502, 2013.

[18] M E Dávila, L Xian, S Cahangirov, A Rubio, and G Le Lay. Germanene: a novel two-dimensional germanium allotrope akin to graphene and silicene. *New Journal of Physics*, 16(9):095002, sep 2014.

[19] Feng-feng Zhu, Wei-jiong Chen, Yong Xu, Chun-lei Gao, Dan-dan Guan, Can-hua Liu, Dong Qian, Shou-Cheng Zhang, and Jin-feng Jia. Epitaxial growth of two-dimensional stanene. *Nat. Mater*, 14:1020, Aug 2015. Article.

[20] Junji Yuhara, Bangjie He, Noriaki Matsunami, Masashi Nakatake, and Guy Le Lay. Graphene's latest cousin: Plumbene epitaxial growth on a "nano watercube". *Advanced Materials*, 31(27):1901017, 2019.

[21] Gian G Guzmán-Verri and L. C. Lew Yan Voon. Electronic structure of silicon-based nanostructures. *Physical Review B - Condensed Matter and Materials Physics*, 76(7), 2007.

[22] S Cahangirov, M Topsakal, E Aktürk, H. Šahin, and S Ciraci. Two- and one-dimensional honeycomb structures of silicon and germanium. *Physical Review Letters*, 102(23), 2009.

[23] Cheng Cheng Liu, Wanxiang Feng, and Yugui Yao. Quantum spin Hall effect in silicene and two-dimensional germanium. *Physical Review Letters*, 107(7), 2011.

[24] Boubekeur Lalmi, Hamid Oughaddou, Hanna Enriquez, Abdelkader Kara, Śbastien Vizzini, Ḃnidicte Ealet, and Bernard Aufray. Epitaxial growth of a silicene sheet. *Applied Physics Letters*, 97(22):223109, 2010.

[25] Abdelkader Kara, Hanna Enriquez, Ari P Seitsonen, L. C. Lew Yan Voon, Sébastien Vizzini, Bernard Aufray, and Hamid Oughaddou. A review on silicene - New candidate for electronics. *Surface Science Reports*, 67(1):1–18, 2012.

[26] Antoine Fleurence, Rainer Friedlein, Taisuke Ozaki, Hiroyuki Kawai, Ying Wang, and Yukiko Yamada-Takamura. Experimental evidence for epitaxial silicene on diboride thin films. *Physical Review Letters*, 108(24), 2012.

[27] Baojie Feng, Zijing Ding, Sheng Meng, Yugui Yao, Xiaoyue He, Peng Cheng, Lan Chen, and Kehui Wu. Evidence of silicene in honeycomb structures of silicon on Ag(111). *Nano Lett.*, 12(7):3507–3511, 2012.

[28] Likai Li, Yijun Yu, Guo Jun Ye, Qingqin Ge, Xuedong Ou, Hua Wu, Donglai Feng, Xian Hui Chen, and Yuanbo Zhang. Black phosphorus field-effect transistors. *Nature Nanotechnology*, 9(5):372–377, may 2014.

[29] Andrea Splendiani, Liang Sun, Yuanbo Zhang, Tianshu Li, Jonghwan Kim, Chi Yung Chim, Giulia Galli, and Feng Wang. Emerging photoluminescence in monolayer MoS2. *Nano Lett.*, 10(4):1271–1275, 2010.

[30] Deepthi Jose and Ayan Datta. Structures and chemical properties of silicene: Unlike graphene. *Accounts of Chemical Research*, 47(2):593–602, 2014.

[31] Mariusz Krawiec. Functionalization of group-14 two-dimensional materials. *Journal of Physics: Condensed Matter*, 30(23):233003, jun 2018.

[32] Alessandro Molle, Carlo Grazianetti, Li Tao, Deepyanti Taneja, Md Hasibul Alam, and Deji Akinwande. Silicene, silicene derivatives, and their device applications. *Chemical Society Reviews*, 47(16):6370–6387, 2018.

[33] Jinglan Qiu, Huixia Fu, Yang Xu, Qing Zhou, Sheng Meng, Hui Li, Lan Chen, and Kehui Wu. From Silicene to Half-Silicane by Hydrogenation. *ACS Nano*, 9(11):11192–11199, 2015.

[34] Wei Wei, Ying Dai, and Baibiao Huang. Hydrogenation of silicene on Ag(111) and formation of half-silicane. *Journal of Materials Chemistry A*, 5(34):18128–18137, 2017.

[35] Manh-Thuong Nguyen, Pham Nam Phong, and Nguyen Duc Tuyen. Hydrogenated Graphene and Hydrogenated Silicene: Computational Insights. *Chem Phys Chem*, 16(8):1733–1738, jun 2015.

[36] Yong Xu, Binghai Yan, Hai-Jun Zhang, Jing Wang, Gang Xu, Peizhe Tang, Wenhui Duan, and Shou-Cheng Zhang. Large-Gap Quantum Spin Hall Insulators in Tin Films. *Physical Review Letters*, 111(13):136804, sep 2013.

[37] Xianqing Lin and Jun Ni. Much stronger binding of metal adatoms to silicene than to graphene: A first-principles study. *Physical Review B*, 86:75440, 2012.

[38] Paola De Padova, Claudio Quaresima, Bruno Olivieri, Paolo Perfetti, and Guy Le Lay. Strong resistance of silicene nanoribbons towards oxidation. *Journal of Physics D: Applied Physics*, 44(31):312001, 2011.

[39] Alessandro Molle, Carlo Grazianetti, Daniele Chiappe, Eugenio Cinquanta, Elena Cianci, Grazia Tallarida, and Marco Fanciulli. Hindering the oxidation of silicene with non-reactive encapsulation. *Advanced Functional Materials*, 23(35):4340–4344, sep 2013.

[40] Esmaeil Zaminpayma and Payman Nayebi. Band gap engineering in silicene: A theoretical study of density functional tight-binding theory. *Physica E: Low-Dimensional Systems and Nanostructures*, 84:555–563, 2016.

[41] V. Ongun Özçelik and S Ciraci. Local Reconstructions of Silicene Induced by Adatoms. *The Journal of Physical Chemistry C*, 117(49):26305–26315, dec 2013.

[42] Seymur Cahangirov, Veli Ongun Özçelik, Lede Xian, Jose Avila, Suyeon Cho, María C Asensio, Salim Ciraci, and Angel Rubio. Atomic structure of the 3 × 3 phase of silicene on Ag(111). *Physical Review B - Condensed Matter and Materials Physics*, 90(3):35448, 2014.

[43] H. W. Kroto, J. R. Heath, S. C. O'Brien, R. F. Curl, and R. E. Smalley. C60: Buckminsterfullerene. *Nature*, 318:162–163, 1985.

[44] Katharina Kaiser, Lorel M. Scriven, Fabian Schulz, Przemyslaw Gawel, Leo Gross, and Harry L. Anderson. An sp-hybridized molecular carbon allotrope, cyclo[18]carbon. *Science*, eaay1914:1, 2019.

[45] Sumio Iijima. Helical microtubules of graphitic carbon. *Nature*, 354:56–58, 1991.

[46] K. S. Novoselov, A. K. Geim, S. V. Morozov, D. Jiang, Y. Zhang, S. V. Dubonos, and et al. Electric field effect in atomically thin carbon films. *Science*, 306:666–669, 2004.

[47] Guoxing Li, Yuliang Li, Huibiao Liu, Yanbing Guo, Yongjun Li, and Daoben

Zhu. Architecture of graphdiyne nanoscale films. *ChemComm*, 46:3256–3258, 2010.

[48] Ryota Matsuoka, Ryota Sakamoto, Ken Hoshiko, Sono Sasaki, Hiroyasu Masunaga, Kosuke Nagashio, and et al. Crystalline graphdiyne nanosheets produced at a gas/liquid or liquid/liquid interface. *J. Am. Chem. Soc.*, 139:3145–3152, 2017.

[49] Yu Liu, Gang Wang, Qingsong Huang, Liwei Guo, and Xiaolong Chen. Structural and electronic properties of t graphene: A two-dimensional carbon allotrope with tetrarings. *Phys. Rev. Lett.*, 108:225505, 2012.

[50] Shunhong Zhang, Jian Zhou, Qian Wang, Xiaoshuang Chen, Yoshiyuki Kawazoe, and Puru Jena. Penta-graphene: A new carbon allotrope. *Proc. Natl. Acad. Sci. U.S.A*, 112:2372–2377, 2015.

[51] Vincent H. Crespi, Lorin X. Benedict, Marvin L. Cohen, and Steven G. Louie. Prediction of a pure-carbon planar covalent metal. *Phys. Rev. B*, 53:R13303–R13305, 1996.

[52] M. Deza, P. W. Fowler, M. Shtogrin, and K. Vietze. Pentaheptite modifications of the graphite sheet. *J. Chem. Inf. Model.*, 40:1325–1332, 2000.

[53] Zhenhai Wang, Xiang-Feng Zhou, Xiaoming Zhang, Qiang Zhu, Huafeng Dong, Mingwen Zhao, and et al. Phagraphene: A low-energy graphene allotrope composed of 5–6–7 carbon rings with distorted dirac cones. *Nano Lett.*, 15:6182–6186, 2015.

[54] Xiaoyin Li, Qian Wang, and Puru Jena. ψ-graphene: A new metallic allotrope of planar carbon with potential applications as anode materials for lithium-ion batteries. *J. Phys. Chem. Lett.*, 8:3234–3241, 2017.

[55] HengChuang Yin, Xizhi Shi, Chaoyu He, Miguel Martinez-Canales, Jin Li, Chris J. Pickard, and et al. Stone-wales graphene: A two-dimensional carbon semimetal with magic stability. *Phys. Rev. B*, 99:041405, 2019.

[56] Andrey N. Enyashin and Alexander L. Ivanovskii. Graphene allotropes. *Phys. Status Solidi B*, 248:1879–1883, 2011.

[57] Nobuo Narita, Sumiaki Nagai, Shugo Suzuki, and Kenji Nakao. Optimized geometries and electronic structures of graphyne and its family. *Phys. Rev. B*, 58:11009–11014, 1998.

[58] Daniel Malko, Christian Neiss, Francesc Viñes, and Andreas Görling. Competition for graphene: Graphynes with direction-dependent dirac cones. *Phys. Rev. Lett.*, 108:086804, 2012.

[59] Linyang Li, Xiangru Kong, and François M. Peeters. New nanoporous graphyne monolayer as nodal line semimetal: Double dirac points with an ultrahigh fermi velocity. *Carbon*, 141:712 – 718, 2019.

[60] Tommaso Morresi, Andrea Pedrielli, Silvio a Beccara, Ruggero Gabbrielli, Nicola M. Pugno, and Simone Taioli. Structural, electronic and mechanical properties of all-sp2 carbon allotropes with density lower than graphene. *Carbon*, 159:512 – 526, 2020.

[61] Han Liu, Adam T. Neal, Zhen Zhu, Zhe Luo, Xianfan Xu, David Tománek, and Peide D. Ye. Phosphorene: An unexplored 2d semiconductor with a high hole mobility. *ACS Nano*, 8(4):4033–4041, 2014.

[62] C. Kamal and Motohiko Ezawa. Arsenene: Two-dimensional buckled and puckered honeycomb arsenic systems. *Phys. Rev. B*, 91:085423, Feb 2015.

[63] Shengli Zhang, Zhong Yan, Yafei Li, Zhongfang Chen, and Haibo Zeng. Atomically thin arsenene and antimonene: Semimetal–semiconductor and indirect–direct band-gap transitions. *Angew. Chem*, 54(10):3112–3115, 2015.

[64] Lei Liu, Y. P. Feng, and Z. X. Shen. Structural and electronic properties of h-bn. *Phys. Rev. B*, 68:104102, Sep 2003.

[65] Houlong L. Zhuang, Arunima K. Singh, and Richard G. Hennig. Computational discovery of single-layer iii-v materials. *Phys. Rev. B*, 87:165415, Apr 2013.

[66] Mingwen Zhao, Xin Chen, Linyang Li, and Xiaoming Zhang. Driving a GaAs film to a large-gap topological insulator by tensile strain. *Sci. Rep.*, 5:8441, 2015.

[67] Per Joensen, R.F. Frindt, and S.Roy Morrison. Single-layer mos2. *MRS Bull.*, 21(4):457 − 461, 1986.

[68] Andrea Splendiani, Liang Sun, Yuanbo Zhang, Tianshu Li, Jonghwan Kim, Chi-Yung Chim, Giulia Galli, and Feng Wang. Emerging photoluminescence in monolayer mos2. *Nano Lett.*, 10(4):1271–1275, 2010.

[69] Yanguang Li, Hailiang Wang, Liming Xie, Yongye Liang, Guosong Hong, and Hongjie Dai. Mos2 nanoparticles grown on graphene: An advanced catalyst for the hydrogen evolution reaction. *J. Am. Chem. Soc.*, 133(19):7296–7299, 2011.

[70] Soumyajyoti Haldar, Hakkim Vovusha, Manoj Kumar Yadav, Olle Eriksson, and Biplab Sanyal. Systematic study of structural, electronic, and optical properties of atomic-scale defects in the two-dimensional transition metal dichalcogenides mX_2 ($m =$ Mo, w; $x =$ S, se, te). *Phys. Rev. B*, 92:235408, Dec 2015.

[71] Bevin Huang, Genevieve Clark, Dahlia R. Klein, David MacNeill, Efrén Navarro-Moratalla, Kyle L. Seyler, Nathan Wilson, Michael A. McGuire, David H. Cobden, Di Xiao, Wang Yao, Pablo Jarillo-Herrero, and Xiaodong Xu. Electrical control of 2d magnetism in bilayer cri3. *Nat. Nanotechnol.*, 13(7):544–548, 2018.

[72] Michael A. McGuire, Hemant Dixit, Valentino R. Cooper, and Brian C. Sales. Coupling of crystal structure and magnetism in the layered, ferromagnetic insulator cri3. *Chem. Mater.*, 27(2):612–620, 2015.

[73] J L Lado and J Fernández-Rossier. On the origin of magnetic anisotropy in two dimensional CrI3. *2D Mater.*, 4(3):035002, jun 2017.

[74] Hai Xu, Dong Han, Yang Bao, Fang Cheng, Zijing Ding, Sherman J. R. Tan, and Kian Ping Loh. Observation of gap opening in 1t′ phase mos2 nanocrystals. *Nano Letters*, 18(8):5085–5090, 2018.

[75] Jannik C. Meyer, C. Kisielowski, R. Erni, Marta D. Rossell, M. F. Crommie, and A. Zettl. Direct imaging of lattice atoms and topological defects in graphene membranes. *Nano Letters*, 8(11):3582–3586, 2008.

[76] M. M. Ugeda, I. Brihuega, F. Guinea, and J. M. Gómez-Rodríguez. Missing atom as a source of carbon magnetism. *Phys. Rev. Lett.*, 104:096804, Mar 2010.

[77] J. Pannetier, J. Bassas-Alsina, J. Rodriguez-Carvajal, and V. Caignaert. Prediction of crystal structures from crystal chemistry rules by simulated annealing. *Nature*, 346(6282):343–345, Jul 1990.

[78] J. Christian Schon and Martin Jansen. First step towards planning of syntheses in solid-state chemistry: Determination of promising structure candidates by global optimization. *Angewandte Chemie International Edition in English*, 35(12):1286–1304, 1996.

[79] R. Martoňák, A. Laio, and M. Parrinello. Predicting crystal structures: The parrinello-rahman method revisited. *Phys. Rev. Lett.*, 90:075503, Feb 2003.

[80] Qiang Zhu, Artem R. Oganov, and Andriy O. Lyakhov. Evolutionary metadynamics: a novel method to predict crystal structures. *CrystEngComm*, 14:3596–3601, 2012.

[81] Scott M. Woodley, Peter D. Battle, Julian D. Gale, and C Richard A. Catlow. The prediction of inorganic crystal structures using a genetic algorithm and energy minimisation. *Phys. Chem. Chem. Phys.*, 1:2535–2542, 1999.

[82] Artem R. Oganov and Colin W. Glass. Crystal structure prediction using ab initio evolutionary techniques: Principles and applications. *J. Chem. Phys.*, 124:244704, 2006.

[83] C. M. Freeman, J. M. Newsam, S. M. Levine, and C. R. A. Catlow. Inorganic crystal structure prediction using simplified potentials and experimental unit cells: application to the polymorphs of titanium dioxide. *J. Mater. Chem.*, 3:531–535, 1993.

[84] Dmitrii V. Semenok, Alexander G. Kvashnin, Ivan A. Kruglov, and Artem R. Oganov. Actinium hydrides ach10, ach12, and ach16 as high-temperature conventional superconductors. *J. Phys. Chem. Lett.*, 9(8):1920–1926, 2018.

[85] David J. Wales and Jonathan P. K. Doye. Global optimization by basin-hopping and the lowest energy structures of lennard-jones clusters containing up to 110 atoms. *J. Phys. Chem. A*, 101(28):5111–5116, 1997.

[86] Stefano Curtarolo, Dane Morgan, Kristin Persson, John Rodgers, and Gerbrand Ceder. Predicting crystal structures with data mining of quantum calculations. *Phys. Rev. Lett.*, 91:135503, Sep 2003.

[87] Weiwei Zhang, Artem R. Oganov, Alexander F. Goncharov, Qiang Zhu, Salah Eddine Boulfelfel, Andriy O. Lyakhov, Elissaios Stavrou, Maddury Somayazulu, Vitali B. Prakapenka, and Zuzana Konôpková. Unexpected stable stoichiometries of sodium chlorides. *Science*, 342(6165):1502–1505, 2013.

[88] Artem R. Oganov, Chris J. Pickard, Qiang Zhu, and Richard J. Needs. Structure prediction drives materials discovery. *Nat. Rev. Mater.*, 4(5):331–348, May 2019.

[89] Xiang-Feng Zhou, Xiao Dong, Artem R. Oganov, Qiang Zhu, Yongjun Tian, and Hui-Tian Wang. Semimetallic two-dimensional boron allotrope with massless dirac fermions. *Phys. Rev. Lett.*, 112:085502, 2014.

[90] Qiang Zhu, Li Li, Artem R. Oganov, and Philip B. Allen. Evolutionary method for predicting surface reconstructions with variable stoichiometry. *Phys. Rev. B*, 87:195317, 2013.

[91] Baojuan Dong, Zhenhai Wang, Nguyen T. Hung, Artem R. Oganov, Teng Yang, Riichiro Saito, and Zhidong Zhang. New two-dimensional phase of tin chalcogenides: Candidates for high-performance thermoelectric materials. *Phys. Rev. Materials*, 3:013405, Jan 2019.

[92] Quan Li, Dan Zhou, Weitao Zheng, Yanming Ma, and Changfeng Chen. Global structural optimization of tungsten borides. *Phys. Rev. Lett.*,

110:136403, Mar 2013.

[93] Lijun Zhang, Yanchao Wang, Jian Lv, and Yanming Ma. Materials discovery at high pressures. *Nat. Rev. Mater.*, 2(4):17005, Feb 2017.

[94] Xiao-Liang Qi and Shou-Cheng Zhang. Topological insulators and superconductors. *Rev. Mod. Phys.*, 83:1057–1110, Oct 2011.

[95] B. Andrei Bernevig and Shou-Cheng Zhang. Quantum spin hall effect. *Phys. Rev. Lett.*, 96:106802, Mar 2006.

[96] C. L. Kane and E. J. Mele. Quantum spin hall effect in graphene. *Phys. Rev. Lett.*, 95:226801, Nov 2005.

[97] M. Z. Hasan and C. L. Kane. Colloquium: Topological insulators. *Rev. Mod. Phys.*, 82:3045–3067, Nov 2010.

[98] Markus König, Steffen Wiedmann, Christoph Brüne, Andreas Roth, Hartmut Buhmann, Laurens W. Molenkamp, Xiao-Liang Qi, and Shou-Cheng Zhang. Quantum spin hall insulator state in hgte quantum wells. *Science*, 318(5851):766–770, 2007.

[99] Ivan Knez, Rui-Rui Du, and Gerard Sullivan. Evidence for helical edge modes in inverted InAs/GaSb quantum wells. *Phys. Rev. Lett.*, 107:136603, Sep 2011.

[100] Zaiyao Fei, Tauno Palomaki, Sanfeng Wu, Wenjin Zhao, Xinghan Cai, Bosong Sun, Paul Nguyen, Joseph Finney, Xiaodong Xu, and David H. Cobden. Edge conduction in monolayer wte2. *Nature Physics*, 13(7):677–682, Jul 2017.

[101] Chenxi Zhang, Santosh KC, Yifan Nie, Chaoping Liang, William G. Vandenberghe, Roberto C. Longo, Yongping Zheng, Fantai Kong, Suklyun Hong, Robert M. Wallace, and Kyeongjae Cho. Charge mediated reversible metal–insulator transition in monolayer mote2 and wxmo1–xte2 alloy. *ACS Nano*, 10(8):7370–7375, 2016.

[102] Xiaofeng Qian, Junwei Liu, Liang Fu, and Ju Li. Quantum spin hall effect in two-dimensional transition metal dichalcogenides. *Science*, 346(6215):1344–1347, 2014.

[103] Ya-ping Wang, Wei-Xiao Ji, Chang-Wen Zhang, Ping Li, Feng Li, Pei-Ji Wang, Sheng-shi Li, and Shi-shen Yan. Large-gap quantum spin Hall state in functionalized dumbbell stanene. *Applied Physics Letters*, 108(7):073104, feb 2016.

[104] Matthias Wuttig and Noboru Yamada. Phase-change materials for rewriteable data storage. *Nature Materials*, 6(11):824–832, Nov 2007.

[105] Ying Wang, Jun Xiao, Hanyu Zhu, Yao Li, Yousif Alsaid, King Yan Fong, Yao Zhou, Siqi Wang, Wu Shi, Yuan Wang, Alex Zettl, Evan J. Reed, and Xiang Zhang. Structural phase transition in monolayer mote2 driven by electrostatic doping. *Nature*, 550(7677):487–491, Oct 2017.

[106] Nikhil Shukla, Arun V. Thathachary, Ashish Agrawal, Hanjong Paik, Ahmedullah Aziz, Darrell G. Schlom, Sumeet Kumar Gupta, Roman Engel-Herbert, and Suman Datta. A steep-slope transistor based on abrupt electronic phase transition. *Nat. Commun.*, 6(1):7812, Aug 2015.

[107] Matthew J. Hollander, Yu Liu, Wen-Jian Lu, Li-Jun Li, Yu-Ping Sun, Joshua A. Robinson, and Suman Datta. Electrically driven reversible insulator–metal phase transition in 1t-tas2. *Nano Lett.*, 15(3):1861–1866, 2015.

[108] Jian Zhou, Shunhong Zhang, and Ju Li. Normal-to-topological insulator martensitic phase transition in group-iv monochalcogenides driven by light.

NPG Asia Mater., 12(1):2, Jan 2020.

[109] Dong Hoon Keum, Suyeon Cho, Jung Ho Kim, Duk-Hyun Choe, Ha-Jun Sung, Min Kan, Haeyong Kang, Jae-Yeol Hwang, Sung Wng Kim, Heejun Yang, K. J. Chang, and Young Hee Lee. Bandgap opening in few-layered monoclinic mote2. *Nature Physics*, 11(6):482–486, Jun 2015.

[110] M.B. Vellinga, R. de Jonge, and C. Haas. Semiconductor to metal transition in mote2. *Journal of Solid State Chemistry*, 2(2):299 – 302, 1970.

[111] Yao Li, Karel-Alexander N. Duerloo, Kerry Wauson, and Evan J. Reed. Structural semiconductor-to-semimetal phase transition in two-dimensional materials induced by electrostatic gating. *Nature Communications*, 7(1):10671, Feb 2016.

[112] Changsik Kim, Sudarat Issarapanacheewin, Inyong Moon, Kwang Young Lee, Changho Ra, Sungwon Lee, Zheng Yang, and Won Jong Yoo. High-electric-field-induced phase transition and electrical breakdown of mote2. *Advanced Electronic Materials*, 6(3):1900964, 2020.

[113] Hajime Kimizuka, Hideo Kaburaki, and Yoshiaki Kogure. Mechanism for negative poisson ratios over the α- β transition of cristobalite, sio_2: A molecular-dynamics study. *Phys. Rev. Lett.*, 84:5548–5551, Jun 2000.

[114] Yeong Jun Park and Jeong Koo Kim. The Effect of Negative Poisson's Ratio Polyurethane Scaffolds for Articular Cartilage Tissue Engineering Applications. *Adv. Mater. Sci. Eng.*, 2013:5, 2013.

[115] K. E. Evans and A. Alderson. Auxetic materials: Functional materials and structures from lateral thinking! *Adv. Mater.*, 12(9):617–628, 2000.

[116] Chunmei Zhang, Tianwei He, Sri Kasi Matta, Ting Liao, Liangzhi Kou, Zhongfang Chen, and Aijun Du. Predicting novel 2d mb2 (m = ti, hf, v, nb, ta) monolayers with ultrafast dirac transport channel and electron-orbital controlled negative poisson's ratio. *J. Phys. Chem. Lett.*, 10(10):2567–2573, 2019.

[117] Rui Peng, Yandong Ma, Zhonglin He, Baibiao Huang, Liangzhi Kou, and Ying Dai. Single-layer ag2s: A two-dimensional bidirectional auxetic semiconductor. *Nano Lett.*, 19(2):1227–1233, 2019.

[118] Liangzhi Kou, Yandong Ma, Chun Tang, Ziqi Sun, Aijun Du, and Changfeng Chen. Auxetic and ferroelastic borophane: A novel 2d material with negative possion's ratio and switchable dirac transport channels. *Nano Lett.*, 16(12):7910–7914, 2016.

[119] Zhibin Gao, Xiao Dong, Nianbei Li, and Jie Ren. Novel two-dimensional silicon dioxide with in-plane negative poisson's ratio. *Nano Lett.*, 17(2):772–777, 2017.

[120] M. Born and R. Oppenheimer. Zur quantentheorie der molekeln. *Annalen der Physik*, 389(20):457–484, 1927.

[121] L. H. Thomas. The calculation of atomic fields. *Mathematical Proceedings of the Cambridge Philosophical Society*, 23(5):542–548, 1927.

[122] Enrico Fermi. Un Metodo Statistice per la Determinazionedi Alcune Proprieta dell Atomo. *Rend. Accad. Naz. Lincei*, 6(December):602–607, 1927.

[123] P. Hohenberg and W. Kohn. Inhomogeneous electron gas. *Phys. Rev.*, 136:B864–B871, Nov 1964.

[124] W. Kohn and L. J. Sham. Self-consistent equations including exchange and

correlation effects. *Phys. Rev.*, 140:A1133–A1138, Nov 1965.

[125] John P. Perdew, J. A. Chevary, S. H. Vosko, Koblar A. Jackson, Mark R. Pederson, D. J. Singh, and Carlos Fiolhais. Atoms, molecules, solids, and surfaces: Applications of the generalized gradient approximation for exchange and correlation. *Phys. Rev. B*, 46:6671–6687, Sep 1992.

[126] John P. Perdew, Kieron Burke, and Matthias Ernzerhof. Generalized gradient approximation made simple. *Physical Review Letters*, 77(18):3865–3868, 1996.

[127] John P. Perdew, Kieron Burke, and Matthias Ernzerhof. Generalized gradient approximation made simple [phys. rev. lett. 77, 3865 (1996)]. *Phys. Rev. Lett.*, 78:1396–1396, Feb 1997.

[128] Axel D. Becke. A new mixing of hartree–fock and local density□functional theories. *The Journal of Chemical Physics*, 98(2):1372–1377, 1993.

[129] K. Kim and K. D. Jordan. Comparison of density functional and mp2 calculations on the water monomer and dimer. *The Journal of Physical Chemistry*, 98(40):10089–10094, 1994.

[130] John P. Perdew, Matthias Ernzerhof, and Kieron Burke. Rationale for mixing exact exchange with density functional approximations. *The Journal of Chemical Physics*, 105(22):9982–9985, 1996.

[131] Jochen Heyd, Gustavo E. Scuseria, and Matthias Ernzerhof. Hybrid functionals based on a screened coulomb potential. *The Journal of Chemical Physics*, 118(18):8207–8215, 2003.

[132] G Kresse and D Joubert. From ultrasoft pseudopotentials to the projector augmented-wave method. *Phys. Rev. B*, 59:1758–1775, 1999.

[133] P. E. Blöchl. Projector augmented-wave method. *Phys. Rev. B*, 50:17953–17979, 1994.

[134] G. Kresse. Ab initio molecular dynamics for liquid metals. *J. Non-Cryst. Solids*, 192-193:222 – 229, 1995.

[135] G. Kresse and J. Furthmüller. Efficient iterative schemes for ab initio total-energy calculations using a plane-wave basis set. *Phys. Rev. B*, 54:11169–11186, 1996.

[136] C. Guillot, Y. Ballu, J. Paigné, J. Lecante, K. P. Jain, P. Thiry, R. Pinchaux, Y. Pétroff, and L. M. Falicov. Resonant photoemission in nickel metal. *Phys. Rev. Lett.*, 39:1632–1635, Dec 1977.

[137] Colin W. Glass, Artem R. Oganov, and Nikolaus Hansen. Uspex—evolutionary crystal structure prediction. *Comput. Phys. Commun.*, 175:713 – 720, 2006.

[138] Hannes Jónsson, Greg Mills, and Karsten W Jacobsen. *Nudged elastic band method for finding minimum energy paths of transitions*. Citeseer, 1998.

[139] Graeme Henkelman, Blas P. Uberuaga, and Hannes Jónsson. A climbing image nudged elastic band method for finding saddle points and minimum energy paths. *The Journal of Chemical Physics*, 113(22):9901–9904, 2000.

[140] John M Ziman. *Electrons and phonons: the theory of transport phenomena in solids*. Oxford university press, 2001.

[141] Wu Li, Jesús Carrete, Nebil A. Katcho, and Natalio Mingo. ShengBTE: a solver of the Boltzmann transport equation for phonons. *Comp. Phys. Commun.*, 185:1747, 2014.

[142] Wu Li, Natalio Mingo, Lucas Lindsay, David A. Broido, Derek A. Stewart, and Nebil A. Katcho. Thermal conductivity of diamond nanowires from first principles. *Phys. Rev. B*, 85:195436, 2012.

[143] R. C. Andrew, R. E. Mapasha, A. M. Ukpong, and N. Chetty. Mechanical properties of graphene and boronitrene. *Phys. Rev. B*, 85:125428, 2012.

[144] Shunhong Zhang, Jian Zhou, Qian Wang, Xiaoshuang Chen, Yoshiyuki Kawazoe, and Puru Jena. Penta-graphene: A new carbon allotrope. *Proc. Natl. Acad. Sci. U.S.A.*, 2015.

[145] Emiliano Cadelano and Luciano Colombo. Effect of hydrogen coverage on the young's modulus of graphene. *Phys. Rev. B*, 85:245434, Jun 2012.

[146] Emiliano Cadelano, Pier Luca Palla, Stefano Giordano, and Luciano Colombo. Elastic properties of hydrogenated graphene. *Phys. Rev. B*, 82:235414, Dec 2010.

[147] J. Bardeen and W. Shockley. Deformation potentials and mobilities in non-polar crystals. *Phys. Rev.*, 80:72–80, Oct 1950.

[148] H. Sevinçli, M. Topsakal, E. Durgun, and S. Ciraci. Electronic and magnetic properties of $3d$ transition-metal atom adsorbed graphene and graphene nanoribbons. *Phys. Rev. B*, 77:195434, May 2008.

[149] Kevin T. Chan, J. B. Neaton, and Marvin L. Cohen. First-principles study of metal adatom adsorption on graphene. *Phys. Rev. B*, 77:235430, Jun 2008.

[150] P. O. Lehtinen, A. S. Foster, A. Ayuela, A. Krasheninnikov, K. Nordlund, and R. M. Nieminen. Magnetic properties and diffusion of adatoms on a graphene sheet. *Phys. Rev. Lett.*, 91:017202, Jun 2003.

[151] A. V. Krasheninnikov, P. O. Lehtinen, A. S. Foster, P. Pyykkö, and R. M. Nieminen. Embedding transition-metal atoms in graphene: Structure, bonding, and magnetism. *Phys. Rev. Lett.*, 102:126807, Mar 2009.

[152] Yanjie Gan, Litao Sun, and Florian Banhart. One- and two-dimensional diffusion of metal atoms in graphene. *Small*, 4(5):587–591, 2008.

[153] Kevin A. Kreisel, Glenn P. A. Yap, Olga Dmitrenko, Clark R. Landis, and Klaus H. Theopold. The Shortest Metal−Metal Bond Yet: Molecular and Electronic Structure of a Dinuclear Chromium Diazadiene Complex. *Journal of the American Chemical Society*, 129(46):14162–14163, 11 2007.

[154] Steven Horvath, Serge I. Gorelsky, Sandro Gambarotta, and Ilia Korobkov. Breaking the 1.80 Å barrier of the Cr-Cr multiple bond between CrII atoms. *Angewandte Chemie - International Edition*, 47(51):9937–9940, 12 2008.

[155] Giovanni La Macchia, Francesco Aquilante, Valera Veryazov, Björn O. Roos, and Laura Gagliardi. Bond Length and Bond Order in One of the Shortest Cr−Cr Bonds. *Inorganic Chemistry*, 47(24):11455–11457, 12 2008.

[156] Hansong Cheng and Lai-Sheng Wang. Dimer Growth, Structural Transition, and Antiferromagnetic Ordering of Small Chromium Clusters. *Physical Review Letters*, 77(1):51–54, 7 1996.

[157] Marcin Brynda, Laura Gagliardi, Per-Olof Widmark, Philip P. Power, and Björn O. Roos. A Quantum Chemical Study of the Quintuple Bond between Two Chromium Centers in [PhCrCrPh]:trans-Bent versus Linear Geometry. *Angewandte Chemie International Edition*, 45(23):3804–3807, 6 2006.

[158] Soumyajyoti Haldar, Bhalchandra S. Pujari, Sumanta Bhandary, Fabrizio Cossu, Olle Eriksson, Dilip G. Kanhere, and Biplab Sanyal. Fe_n (n=1-6)

clusters chemisorbed on vacancy defects in graphene: Stability, spin-dipole moment, and magnetic anisotropy. *Physical Review B*, 89(20):205411, 5 2014.

[159] Jindong Ren, Haiming Guo, Jinbo Pan, Yan-Fang Zhang, Yifeng Yang, Xu Wu, Shixuan Du, Min Ouyang, and Hong-Jun Gao. Interatomic spin coupling in manganese clusters registered on graphene. *Phys. Rev. Lett.*, 119:176806, Oct 2017.

[160] Ding Sheng Wang, Ruqian Wu, and A. J. Freeman. First-principles theory of surface magnetocrystalline anisotropy and the diatomic-pair model. *Physical Review B*, 47(22):14932–14947, 1993.

[161] Pedro Borlido, Claudia Rödl, Miguel A.L. Marques, and Silvana Botti. The ground state of two-dimensional silicon. *2D Materials*, 5(3):035010, apr 2018.

[162] Tian Zhang, Zhao Yi Zeng, Yan Cheng, Xiang Rong Chen, and Ling Cang Cai. Dumbbell silicene: A strain-induced room temperature quantum spin Hall insulator. *New Journal of Physics*, 18(4), 2016.

[163] H Kageshima and K Shiraishi. Microscopic mechanism for SiO2/Si interface passivation: Si=O double bond formation. *Surface Science*, 380(1):61–65, 1997.

[164] Mingwen Zhao, Xiaoming Zhang, and Linyang Li. Strain-driven band inversion and topological aspects in Antimonene. *Scientific Reports*, 5(1):16108, dec 2015.

[165] Mingwen Zhao, Xiaoming Zhang, and Linyang Li. Strain-driven band inversion and topological aspects in Antimonene. *Scientific Reports*, 5(1):16108, dec 2015.

[166] H. Terrones, M. Terrones, E. Hernández, N. Grobert, J-C. Charlier, and P. M. Ajayan. New metallic allotropes of planar and tubular carbon. *Phys. Rev. Lett.*, 84:1716–1719, 2000.

[167] X. Rocquefelte, G.-M. Rignanese, V. Meunier, H. Terrones, M. Terrones, and J.-C. Charlier. How to identify haeckelite structures: A theoretical study of their electronic and vibrational properties. *Nano Lett.*, 4(5):805–810, 2004.

[168] Shuaiwei Wang, Yubing Si, Baocheng Yang, Eli Ruckenstein, and Houyang Chen. Two-dimensional carbon-based auxetic materials for broad-spectrum metal-ion battery anodes. *J. Phys. Chem. Lett.*, 10(12):3269–3275, 2019.

[169] Ferdaous Ben Romdhane, Ovidiu Cretu, Lamjed Debbichi, Olle Eriksson, Sébastien Lebègue, and Florian Banhart. Quasi-2d cu2s crystals on graphene: In-situ growth and ab-initio calculations. *Small*, 11(11):1253–1257, 2015.

[170] Bo Li, Le Huang, Guangyao Zhao, Zhongming Wei, Huanli Dong, Wenping Hu, Lin-Wang Wang, and Jingbo Li. Large-size 2d β-cu2s nanosheets with giant phase transition temperature lowering (120 k) synthesized by a novel method of super-cooling chemical-vapor-deposition. *Adv. Mater.*, 28(37):8271–8276, 2016.

[171] Yu Guo, Qisheng Wu, Yunhai Li, Ning Lu, Keke Mao, Yizhen Bai, Jijun Zhao, Jinlan Wang, and Xiao Cheng Zeng. Copper(i) sulfide: a two-dimensional semiconductor with superior oxidation resistance and high carrier mobility. *Nanoscale Horiz.*, 4:223–230, 2019.

[172] Jiangjiang Feng, Xiaohui Li, Zhaojiang Shi, Chuang Zheng, Xuwei Li, Deying Leng, Yamin Wang, Jie Liu, and Lujun Zhu. 2d ductile transition metal chalcogenides (tmcs): Novel high-performance ag2s nanosheets for ultrafast

photonics. *Adv. Opt. Mater.*, page 1901762, 2019.

[173] Yue Zhu, Lele Peng, Weinan Zhu, Deji Akinwande, and Guihua Yu. Layer-by-layer assembly of two-dimensional colloidal cu2se nanoplates and their layer-dependent conductivity. *Chem. Mater.*, 28(12):4307–4314, 2016.

[174] Graeme Henkelman, Andri Arnaldsson, and Hannes Jónsson. A fast and robust algorithm for bader decomposition of charge density. *Comput. Mater. Sci.*, 36(3):354 – 360, 2006.

[175] Qisheng Wu, Wen Wu Xu, Dongdong Lin, Jinlan Wang, and Xiao Cheng Zeng. Two-dimensional gold sulfide monolayers with direct band gap and ultrahigh electron mobility. *J. Phys. Chem. Lett.*, 10(13):3773–3778, 2019.

[176] Xingli Wang, Yongji Gong, Gang Shi, Wai Leong Chow, Kunttal Keyshar, Gonglan Ye, Robert Vajtai, Jun Lou, Zheng Liu, Emilie Ringe, Beng Kang Tay, and Pulickel M. Ajayan. Chemical vapor deposition growth of crystalline monolayer mose2. *ACS Nano*, 8(5):5125–5131, 2014.

[177] Tetsuya Tohei, Akihide Kuwabara, Fumiyasu Oba, and Isao Tanaka. Debye temperature and stiffness of carbon and boron nitride polymorphs from first principles calculations. *Phys. Rev. B*, 73:064304, Feb 2006.

[178] Siqi Lin, Wen Li, Shasha Li, Xinyue Zhang, Zhiwei Chen, Yidong Xu, and et al. High thermoelectric performance of ag9gase6 enabled by low cutoff frequency of acoustic phonons. *Joule*, 1(4):816 – 830, 2017.

[179] Zhibin Gao, Fang Tao, and Jie Ren. Unusually low thermal conductivity of atomically thin 2d tellurium. *Nanoscale*, 10:12997–13003, 2018.

[180] A. Bondi. van der waals volumes and radii. *J. Phys. Chem.*, 68(3):441–451, 1964.

[181] Shouyuan Huang, Mauricio Segovia, Xiaolong Yang, Yee Rui Koh, Yixiu Wang, Peide D Ye, Wenzhuo Wu, Ali Shakouri, Xiulin Ruan, and Xianfan Xu. Anisotropic thermal conductivity in 2d tellurium. *2D Mater.*, 7(1):015008, nov 2019.

[182] G.A. Slack. Nonmetallic crystals with high thermal conductivity. *J. Phys. Chem. Solids*, 34(2):321 – 335, 1973.

[183] L. Lindsay, D. A. Broido, and T. L. Reinecke. First-principles determination of ultrahigh thermal conductivity of boron arsenide: A competitor for diamond? *Phys. Rev. Lett.*, 111:025901, Jul 2013.

[184] Samantha Bruzzone and Gianluca Fiori. Ab-initio simulations of deformation potentials and electron mobility in chemically modified graphene and two-dimensional hexagonal boron-nitride. *Appl. Phys. Lett.*, 99(22):222108, 2011.

[185] Jingsi Qiao, Xianghua Kong, Zhi-Xin Hu, Feng Yang, and Wei Ji. High-mobility transport anisotropy and linear dichroism in few-layer black phosphorus. *Nature Communications*, 5(1):4475, 2014.

[186] Changgu Lee, Xiaoding Wei, Jeffrey W. Kysar, and James Hone. Measurement of the elastic properties and intrinsic strength of monolayer graphene. *Science*, 321(5887):385–388, 2008.

[187] Manish Chhowalla, Hyeon Suk Shin, Goki Eda, Lain-Jong Li, Kian Ping Loh, and Hua Zhang. The chemistry of two-dimensional layered transition metal dichalcogenide nanosheets. *Nature Chemistry*, 5(4):263–275, Apr 2013.

[188] Bo Peng, Hao Zhang, Weiwen Chen, Bowen Hou, Zhi-Jun Qiu, Hezhu Shao,

Heyuan Zhu, Bartomeu Monserrat, Desheng Fu, Hongming Weng, and Costas M. Soukoulis. Sub-picosecond photo-induced displacive phase transition in two-dimensional mote2. *npj 2D Materials and Applications*, 4(1):14, Jun 2020.

[189] Qian Wang, Edward T. F. Rogers, Behrad Gholipour, Chih-Ming Wang, Guanghui Yuan, Jinghua Teng, and Nikolay I. Zheludev. Optically reconfigurable metasurfaces and photonic devices based on phase change materials. *Nature Photonics*, 10(1):60–65, Jan 2016.

[190] Li-Ming Yang, Vladimir Bačić, Ivan A. Popov, Alexander I. Boldyrev, Thomas Heine, Thomas Frauenheim, and Eric Ganz. Two-dimensional cu2si monolayer with planar hexacoordinate copper and silicon bonding. *J. Am. Chem. Soc.*, 137(7):2757–2762, 2015.

[191] Guang-Rui Qian, Xiao Dong, Xiang-Feng Zhou, Yongjun Tian, Artem R. Oganov, and Hui-Tian Wang. Variable cell nudged elastic band method for studying solid–solid structural phase transitions. *Comput. Phys. Commun.*, 184(9):2111 – 2118, 2013.

[192] R. Fivaz and E. Mooser. Mobility of charge carriers in semiconducting layer structures. *Phys. Rev.*, 163:743–755, Nov 1967.

[193] B. Radisavljevic, A. Radenovic, J. Brivio, V. Giacometti, and A. Kis. Single-layer mos2 transistors. *Nature Nanotechnology*, 6(3):147–150, Mar 2011.

[194] Satoru Emori, Uwe Bauer, Sung-Min Ahn, Eduardo Martinez, and Geoffrey S. D. Beach. Current-driven dynamics of chiral ferromagnetic domain walls. *Nature Materials*, 12(7):611–616, Jul 2013.

[195] C. K. Safeer, Emilie Jué, Alexandre Lopez, Liliana Buda-Prejbeanu, Stéphane Auffret, Stefania Pizzini, Olivier Boulle, Ioan Mihai Miron, and Gilles Gaudin. Spin–orbit torque magnetization switching controlled by geometry. *Nature Nanotechnology*, 11(2):143–146, Feb 2016.

[196] Kevin Garello, Ioan Mihai Miron, Can Onur Avci, Frank Freimuth, Yuriy Mokrousov, Stefan Blügel, Stéphane Auffret, Olivier Boulle, Gilles Gaudin, and Pietro Gambardella. Symmetry and magnitude of spin–orbit torques in ferromagnetic heterostructures. *Nature Nanotechnology*, 8(8):587–593, Aug 2013.

[197] Yuan Ping Feng, Lei Shen, Ming Yang, Aizhu Wang, Minggang Zeng, Qingyun Wu, Sandhya Chintalapati, and Ching-Ray Chang. Prospects of spintronics based on 2d materials. *WIREs Computational Molecular Science*, 7(5):e1313, 2017.

[198] Sajid Husain, Xin Chen, Rahul Gupta, Nilamani Behera, Prabhat Kumar, Tomas Edvinsson, F. García-Sánchez, Rimantas Brucas, Sujeet Chaudhary, Biplab Sanyal, Peter Svedlindh, and Ankit Kumar. Large damping-like spin–orbit torque in a 2d conductive 1t-tas2 monolayer. *Nano Letters*, 20(9):6372–6380, 2020.

[199] Sajid Husain, Xin Chen, Rahul Gupta, Nilamani Behera, Prabhat Kumar, Tomas Edvinsson, Felipe Garcia-Sanchez, Rimantas Brucas, Sujeet Chaudhary, Biplab Sanyal, et al. Large damping-like spin–orbit torque in a 2d conductive 1t-tas2 monolayer. *Nano letters*, 20(9):6372–6380, 2020.

[200] Bevin Huang, Genevieve Clark, Efrén Navarro-Moratalla, Dahlia R Klein, Ran

Cheng, Kyle L Seyler, Ding Zhong, Emma Schmidgall, Michael A McGuire, David H Cobden, et al. Layer-dependent ferromagnetism in a van der waals crystal down to the monolayer limit. *Nature*, 546(7657):270–273, 2017.

Acta Universitatis Upsaliensis

Digital Comprehensive Summaries of Uppsala Dissertations
from the Faculty of Science and Technology 1975

Editor: The Dean of the Faculty of Science and Technology

A doctoral dissertation from the Faculty of Science and Technology, Uppsala University, is usually a summary of a number of papers. A few copies of the complete dissertation are kept at major Swedish research libraries, while the summary alone is distributed internationally through the series Digital Comprehensive Summaries of Uppsala Dissertations from the Faculty of Science and Technology. (Prior to January, 2005, the series was published under the title "Comprehensive Summaries of Uppsala Dissertations from the Faculty of Science and Technology".)

ACTA
UNIVERSITATIS
UPSALIENSIS
UPPSALA
2020